

Institut für Kern und Teilchenphysik  
Fakultät Mathematik und Naturwissenschaften  
Technische Universität Dresden

---

# Photodisintegration studies of astrophysically relevant p-nuclei

---

Dissertation  
zur Erlangung des  
Doktorgrades der Naturwissenschaften  
(Doctor rerum naturalium)

vorgelegt von  
**Chithra Kumaran Nair**  
geboren am 7. April 1981 in Thrissur, Kerala, Indien

1. Gutachter: Prof. Dr. E. Grosse, TU Dresden  
2. Gutachter: Prof. Dr. A. G. Zilges, Universität zu Köln  
Eingereicht am 3. Juni 2009  
Verteidigt am 30. September 2009



# Abstract

The majority of the light elements up to iron (Fe) are formed by successive rounds of thermonuclear fusion burning in the stellar interiors. The nuclei heavier than iron ( $Z > 26$ ) are being synthesized mainly by neutron-capture reactions - the astrophysical r- and s-processes. There are 35 neutron deficient stable isotopes between Se and Hg which are shielded from the rapid neutron capture by stable isobars. These so-called p-nuclei are produced in explosive stellar environments via photodisintegration reactions like  $(\gamma, n)$ ,  $(\gamma, p)$  and  $(\gamma, \alpha)$  on r- or s-seed nuclei. The reaction rates of the p-nuclei are mostly based on theoretical parameterizations using statistical model calculations. At the bremsstrahlung facility of the superconducting electron accelerator ELBE, photon-induced reactions of the p-nuclei are being studied.

In the scope of this thesis work, photodisintegration measurements of the p-nuclei  $^{92}\text{Mo}$  and  $^{144}\text{Sm}$  have been performed via the photoactivation technique. The residual nuclei resulting from photoactivation were studied via  $\gamma$ -ray spectroscopy. For the decay measurements of short-lived nuclei, a pneumatic delivery system has been used. In the case of  $^{144}\text{Sm}(\gamma, p)$  and  $^{144}\text{Sm}(\gamma, \alpha)$  reactions, the activated samarium samples with very low counting statistics were measured at the underground laboratory "Felsenkeller" in Dresden. The experimental activation yields for the  $^{144}\text{Sm}(\gamma, n)$ ,  $(\gamma, p)$  and  $(\gamma, \alpha)$  and the  $^{92}\text{Mo}(\gamma, \alpha)$  reactions were determined. It is to be emphasized that the  $(\gamma, p)$  and  $(\gamma, \alpha)$  reactions were measured for the first time in a laboratory at astrophysically relevant energies.

In all the mentioned experiments, special care was taken to determine the endpoint energy of the bremsstrahlung spectra by using the photodisintegration of deuteron. The  $^{197}\text{Au}(\gamma, n)^{196}\text{Au}$  reaction has been established as an activation standard. The photoactivation yields for the  $^{197}\text{Au}(\gamma, n)$  and  $^{144}\text{Sm}(\gamma, n)$  reactions have been compared to the yield calculated using cross sections from previous photoneutron experiments. A comparison of the two data sets leads to a conclusion on the inaccuracies in previous data. The statistical uncertainties involved in the activation experiments are very small except for the case of decay spectra with weak counting statistics. The systematic uncertainties are mostly from the experimental determination of photon flux. A detailed discussion of the overall uncertainty is provided.

Hauser-Feshbach statistical model calculations using TALYS and NON-SMOKER codes have been performed for all the concerned reactions. The experimental activation yields, in general, agree within a factor of 2 to the simulated yields using statistical model predictions. The sensitivity of the model codes to the nuclear physics inputs like optical-model potentials, nuclear level densities and  $\gamma$ -ray strength functions has been tested.



# Contents

<b>1</b>	<b>Introduction</b>	<b>1</b>
<b>2</b>	<b>Physics Background</b>	<b>3</b>
2.1	Stellar nucleosynthesis . . . . .	3
2.2	Nucleosynthesis beyond iron . . . . .	4
2.2.1	The s-process . . . . .	5
2.2.2	The r-process . . . . .	6
2.2.3	The p-process . . . . .	7
2.3	The p-nuclides in detail . . . . .	7
2.3.1	Production of p-nuclides . . . . .	8
2.3.2	Experimental situation . . . . .	9
2.4	The p-nuclei $^{92}\text{Mo}$ and $^{144}\text{Sm}$ . . . . .	10
<b>3</b>	<b>Photodisintegration via real photons at ELBE</b>	<b>13</b>
3.1	The ELBE accelerator . . . . .	13
3.2	Photoactivation method . . . . .	14
3.3	Photoactivation facility at the ELBE accelerator . . . . .	16
3.3.1	Electron beam dump - The photoactivation site . . . . .	16
3.3.2	The photon scattering site . . . . .	17
3.4	Determination of photon flux . . . . .	18
3.4.1	Spectral shape of bremsstrahlung . . . . .	18
3.4.2	Photon scattering from $^{11}\text{B}$ . . . . .	19
3.4.3	Thick target Bremsstrahlung at the photoactivation site . . . . .	23
3.5	Determination of the electron-beam energy . . . . .	24
3.5.1	The NMR method . . . . .	24
3.5.2	Photodisintegration of the deuteron . . . . .	25
3.5.3	Monitoring of the electron beam stability . . . . .	27
<b>4</b>	<b>Decay studies of the activated targets</b>	<b>29</b>
4.1	Determination of peak intensity . . . . .	29
4.1.1	Peakfit functions for $\gamma$ -ray spectra . . . . .	29
4.1.2	The dead time and pile-up correction factors . . . . .	31
4.2	Counting facilities . . . . .	32
4.2.1	The low-level counting setup . . . . .	32
4.2.2	Efficiency variations with source-detector geometry . . . . .	35
4.2.3	Decay studies at the underground laboratory 'Felsenkeller' . . . . .	36
4.3	The rabbit system . . . . .	39
4.4	Corrections for self-absorption and target dimensions . . . . .	41

<b>5</b>	<b>Experimental results</b>	<b>45</b>
5.1	The statistical model . . . . .	45
5.1.1	The model codes TALYS and NON-SMOKER . . . . .	46
5.2	Activation yield for the $^{197}\text{Au}(\gamma, n)$ reaction . . . . .	47
5.2.1	Comparison with previous experiments . . . . .	48
5.2.2	Comparison with model calculations . . . . .	51
5.2.3	Phenomenological parameterization of the photon strength function . . . . .	51
5.3	Photodisintegration of $^{144}\text{Sm}$ . . . . .	53
5.4	Activation yield for the $^{144}\text{Sm}(\gamma, n)$ reaction . . . . .	54
5.4.1	Comparison with previous experiments . . . . .	56
5.4.2	Comparison with model calculations . . . . .	58
5.5	Activation yield for the $^{144}\text{Sm}(\gamma, p)$ and $^{144}\text{Sm}(\gamma, \alpha)$ reactions . . . . .	59
5.6	Activation yield for the $^{92}\text{Mo}(\gamma, \alpha)$ reaction . . . . .	61
5.7	Statistical and systematic uncertainties . . . . .	63
<b>6</b>	<b>Discussion</b>	<b>67</b>
6.1	Sensitivity of the statistical model calculations to nuclear physics input . . . . .	67
6.1.1	The $\gamma$ -ray strength functions . . . . .	67
6.1.2	Optical model potentials . . . . .	70
6.1.3	Nuclear level densities . . . . .	72
<b>7</b>	<b>Summary and Outlook</b>	<b>75</b>
	<b>Appendices</b>	<b>77</b>
<b>A</b>	<b>Detector dimensions</b>	<b>77</b>
A.1	HPGe detectors at photon scattering site . . . . .	77
A.2	HPGe detectors at the counting facilities . . . . .	77
A.3	Silicon detectors for endpoint energy determination . . . . .	78
<b>B</b>	<b>Photopeak efficiency determination</b>	<b>79</b>
B.1	Calibration standards . . . . .	79
B.2	Coincidence summing corrections . . . . .	80
<b>C</b>	<b>Photon scattering from <math>^{11}\text{B}</math></b>	<b>83</b>
<b>D</b>	<b>Decay properties of the photodisintegration targets</b>	<b>87</b>
	<b>Bibliography</b>	<b>89</b>
	<b>Acknowledgement</b>	<b>99</b>
	<b>Erklärung</b>	<b>101</b>

# List of Figures

2.1	Evolution of the internal structure of a spherically-symmetric massive star . . .	4
2.2	Solar abundances of trans-iron elements splitted into different components . . .	5
2.3	The possible routes for the formation of p-nuclides from r- or s-seeds . . . . .	7
2.4	Averaged normalized overproduction factor for the neutron-deficient p-nuclei . .	10
3.1	Schematic layout of the ELBE accelerator and associated experimental facilities	14
3.2	Photoactivation setup at ELBE accelerator . . . . .	16
3.3	Electron beam dump (photoactivation site) at ELBE accelerator . . . . .	17
3.4	Comparison of theoretical bremsstrahlung cross sections for a thin radiator . . .	19
3.5	Efficiency curve of a 100% HPGe detector used at the photon scattering site . .	20
3.6	GEANT3 simulations for the full-energy peak efficiency of a 100% HPGe detector	20
3.7	Decay scheme of $^{11}\text{B}$ . . . . .	21
3.8	Spectrum of $^{11}\text{B}$ taken with a 100% HPGe detector. . . . .	22
3.9	Absolute photon fluence measured from the scattered photons in $^{11}\text{B}$ . . . . .	22
3.10	Thick target bremsstrahlung spectrum at the photoactivation site behind the graphite beam dump . . . . .	23
3.11	User interface to the NMR teslameter . . . . .	24
3.12	Spectrum of a mixed $^{239}\text{Pu}/^{241}\text{Am}/^{244}\text{Cm}$ alpha source . . . . .	26
3.13	Proton spectrum from the photodisintegration of deuterons . . . . .	26
3.14	The operation of the beam energy control loop in the nuclear physics beam line	27
3.15	The beam current recorded during an experimental run at ELBE . . . . .	28
4.1	Peak fit for one of the strongest decay transitions of $^{133}\text{Ba}$ . . . . .	30
4.2	Peak area calculations for $\gamma$ -peaks with very low counting statistics . . . . .	30
4.3	The dead time and pile-up correction using pulser method . . . . .	31
4.4	The low-level counting setup . . . . .	33
4.5	Natural background measured with the 90% HPGe detector in the low-level counting setup . . . . .	33
4.6	Spectrum of $^{133}\text{Ba}$ with and without cadmium absorber . . . . .	34
4.7	Efficiency curves for HPGe detectors with 90% and 60% relative efficiency . . .	35
4.8	Variation of point source efficiency with source-detector distance . . . . .	36
4.9	The point source efficiency ratio for 661 keV for different distances on the sym- metry and off-axis distances . . . . .	36
4.10	Comparison of background spectra from underground laboratories at different depths . . . . .	37
4.11	Photopeak efficiency curve for the 30% detector at Felsenkeller . . . . .	38
4.12	Comparison of the decay measurement at ELBE and Felsenkeller for the decay originating from $^{144}\text{Sm}(\gamma, \alpha)^{140}\text{Nd}$ reaction . . . . .	38

4.13	Schematic sketch of the pneumatic delivery system . . . . .	39
4.14	Sample spectrum for short-lived activities measured with rabbit system . . . . .	40
4.15	Half-life determination of $^{197m}\text{Au}$ . . . . .	40
4.16	Measuring geometry for experiments using the rabbit system . . . . .	42
4.17	Photograph of the cassettes used for measurements with rabbit system . . . . .	42
4.18	Absolute photopeak efficiencies for volume targets . . . . .	43
5.1	Decay scheme for the $^{197}\text{Au}(\gamma, n)$ reaction-1 . . . . .	47
5.2	Decay scheme for the $^{197}\text{Au}(\gamma, n)$ reaction-2 . . . . .	47
5.3	Spectrum of an irradiated $^{197}\text{Au}$ target . . . . .	48
5.4	Photoneutron cross sections for $^{197}\text{Au}(\gamma, n)$ from previous experiments . . . . .	49
5.5	$^{197}\text{Au}(\gamma, n)$ activation yield compared to the yield calculated using cross sections measured in previous experiments . . . . .	50
5.6	$^{197}\text{Au}(\gamma, n)$ activation yield compared to the yield calculated using cross sections from model calculations . . . . .	52
5.7	The photon strength function of $^{197}\text{Au}$ derived on the assumption of oblate deformation . . . . .	54
5.8	The photodisintegration reactions $(\gamma, n)$ , $(\gamma, p)$ and $(\gamma, \alpha)$ on $^{144}\text{Sm}$ . . . . .	55
5.9	Decay scheme for the $^{144}\text{Sm}(\gamma, p/n)$ reaction . . . . .	55
5.10	Decay spectra following the photodisintegration reaction $^{144}\text{Sm}(\gamma, n)$ . . . . .	56
5.11	Photoneutron cross sections for $^{144}\text{Sm}$ from model calculations and previous experiments . . . . .	57
5.12	$^{144}\text{Sm}(\gamma, n)^{143m, g}\text{Sm}$ activation yield compared to the yield calculated using cross sections measured in previous experiments . . . . .	57
5.13	$^{144}\text{Sm}(\gamma, n)^{143}\text{Sm}$ activation yield compared to the yield calculated using cross sections from model calculations . . . . .	58
5.14	$^{144}\text{Sm}(\gamma, p)$ and $^{144}\text{Sm}(\gamma, \alpha)$ cross sections from model calculations . . . . .	59
5.15	Spectrum of an irradiated $^{144}\text{Sm}$ target . . . . .	60
5.16	Activation yield for the photodisintegration reactions $^{144}\text{Sm}(\gamma, p)$ and $^{144}\text{Sm}(\gamma, \alpha)$ compared to model calculations . . . . .	60
5.17	Spectrum of an irradiated $^{92}\text{Mo}$ target . . . . .	61
5.18	Half-life measurements for the $^{92}\text{Mo}(\gamma, \alpha)$ photodisintegration . . . . .	61
5.19	Activation yield for $^{92}\text{Mo}(\gamma, \alpha)$ reaction compared to model calculations . . . . .	62
5.20	$^{197}\text{Au}(\gamma, n)$ activation yield close to threshold . . . . .	64
6.1	Sensitivity of the model calculations to $^{144}\text{Sm}(\gamma, n)$ activation yield with different inputs for photon strength functions . . . . .	69
6.2	Sensitivity of the model calculations to $^{144}\text{Sm}(\gamma, \alpha) / ^{144}\text{Sm}(\gamma, p)$ activation yield with different inputs for the photon strength functions . . . . .	69
6.3	Sensitivity of the model calculations to $^{144}\text{Sm}(\gamma, n)$ activation yield with different inputs for the optical model potentials . . . . .	71
6.4	Sensitivity of the model calculations to $^{144}\text{Sm}(\gamma, \alpha) / ^{144}\text{Sm}(\gamma, p)$ activation yield with different inputs for the optical model potentials . . . . .	71
6.5	Sensitivity of the model calculations to $^{144}\text{Sm}(\gamma, n)$ activation yield with different inputs for the nuclear level densities . . . . .	72
6.6	Sensitivity of the model calculations to $^{144}\text{Sm}(\gamma, \alpha) / ^{144}\text{Sm}(\gamma, p)$ activation yield with different inputs for the nuclear level densities . . . . .	73



---

B.1	Decay scheme of $^{133}\text{Ba}$ - energies displayed in keV. The scheme is not drawn to scale. . . . .	80
-----	--	----



# List of Tables

3.1	Beam parameters used for photoactivation experiments . . . . .	14
4.1	Dimensions of the targets used for decay studies with rabbit system . . . . .	42
5.1	The statistical and systematic uncertainties in the activation experiments . . . . .	63
6.1	The different nuclear physics inputs to TALYS model code . . . . .	68
A.1	Specifications of the n-type HPGe detectors at the photon scattering site . . . . .	77
A.2	Specifications of the 90% and 60% detectors at the low-level counting setup and the 30% detector at Felsenkeller . . . . .	77
A.3	Specifications of the Si-detectors used for recording the proton spectra . . . . .	78
B.1	Spectrometric properties of the calibration standards . . . . .	79
C.1	Properties of the levels in $^{11}\text{B}$ used for photon scattering experiments. . . . .	83
D.1	Decay properties of the photodisintegration targets . . . . .	87



# Chapter 1

## Introduction

It is always a fascinating world: the night sky with its twinkle tiny objects. We often wonder - how the stars are born, galaxies are formed, what is beyond our earth? Many of these were answered by astronomy and astrophysics. These two research areas are dealing with the physics of the universe on a cosmic scale and serve as the key to explore many features of it.

Citing Carl Sagan's famous quote "...we are made of star stuff", an accepted fact could be emphasized - the building elements of human bodies are the debris from stars. Most of the elements heavier than hydrogen and helium were created and processed in the interior of stars and similar systems like supernovae before they were ejected into space. The elements in our body: iron, calcium, carbon, nitrogen, all were formed in the interior of the stars at extreme temperature and pressure conditions.

The link between the two - connecting the cosmic scale astrophysics to the micro scale nucleus opened up the way to the exciting new field of Nuclear Astrophysics. With a history extending back to not more than fifty years, it is now the most powerful tool to study the key processes governing the element formation in the universe. The foundation stone was laid by the benchmark paper in 1957 from E. M. Burbidge, G. R. Burbidge, W. Fowler and F. Hoyle (B<sup>2</sup>FH, [Burb57]) which provided a wonderful explanation of the nucleosynthesis processes in the stellar evolution stages.

Now the interdisciplinary research in Nuclear Astrophysics is one of the most attractive fields of science. Forty years after the publication of B<sup>2</sup>FH, in 1997, Wallerstein et al. [Wall97] summarized the new discoveries and developments in nucleosynthesis and stellar evolution. One of the open questions which calls for special attention was pointed out to be heavy element synthesis beyond iron. The motivation behind this dissertation falls into this category, especially to the studies of the heavy element species categorized as p-nuclei.

In this thesis, photodisintegration measurements of the p-nuclei <sup>92</sup>Mo and <sup>144</sup>Sm have been performed via the photoactivation technique. The Mo isotopes are underproduced significantly in the p-nucleosynthesis network calculations and experimental information about the photodisintegration of Mo is of high demand in the nuclear astrophysics community. In this work, the first experimental results from the <sup>92</sup>Mo( $\gamma, \alpha$ ) reaction are provided. The nuclides <sup>144</sup>Sm and <sup>146</sup>Sm have been identified as a pure p-process chronometer pair and there were many efforts to determine the <sup>146</sup>Sm/<sup>144</sup>Sm production ratio experimentally. In general, it is highly necessary to provide experimental information to test the nuclear-physics-related uncertainties in the p-process model predictions. Systematic investigation of the ( $\gamma, \alpha$ ) reactions in the mass region  $A \geq 140$  is considered to be very important. The experimental activation yields for the <sup>144</sup>Sm ( $\gamma, n$ ), ( $\gamma, p$ ) and ( $\gamma, \alpha$ ) reactions are determined in this work.

The second chapter starts with an overview of the stellar nucleosynthesis processes. In partic-

ular, the heavy element synthesis is discussed with special emphasis on the p-nuclei formation mechanisms. In the second part of Chapter 2, the experimental studies so far on these so-called *nuclear astrophysics p-nuts* are outlined briefly. The nuclei under discussion in the context of this thesis - Mo and Sm, are introduced in the last part of Chapter 2.

In Chapter 3, a description of the photoactivation facility at the superconducting electron accelerator ELBE is given. There are two irradiation sites: the photoactivation site with a high photon flux and the photon scattering site equipped with detectors to measure the scattered  $\gamma$ -rays online. In this chapter, the techniques used for the determination of photon flux and the bremsstrahlung endpoint energy are presented.

For the reaction yield determination, the activated targets are studied by  $\gamma$ -ray spectroscopy. The  $\gamma$ -counting facilities are described in Chapter 4. The pneumatic delivery system for the decay studies of short-lived nuclei and the measurements at the underground  $\gamma$ -counting laboratory "Felsenkeller" are discussed in detail.

In Chapter 5, experimental results from the photodisintegration studies of  $^{144}\text{Sm}$  and  $^{92}\text{Mo}$  will be presented and compared to the theoretical predictions using Hauser-Feshbach models. The model codes TALYS and NON-SMOKER were used for simulating the activation yield. The  $^{197}\text{Au}(\gamma, n)^{196}\text{Au}$  reaction has been established as an activation standard. The photoactivation yields have been compared to the yield calculated using cross sections from previous experiments. The statistical and systematic uncertainties involved in the photoactivation experiments are discussed in detail in the last section of Chapter 5. The sensitivity of the statistical model calculations to their nuclear physics inputs are tested in Chapter 6. A brief summary and an outlook on the future perspectives are given in the concluding chapter.

# Chapter 2

## Physics Background

In this chapter, the nucleosynthesis processes in stars are briefly introduced with particular emphasis on the trans-iron element formation processes. The p-nuclei formation via photodisintegration reactions are discussed in detail. The current experimental status regarding the p-nuclei studies is described along with the motivation for focusing our studies on the p-nuclei  $^{144}\text{Sm}$  and  $^{92}\text{Mo}$ .

### 2.1 Stellar nucleosynthesis

The solar abundance distribution compiled by Anders and Grevesse [Ande89] summarized the observational data from the chemical analysis of meteoroids as well as solar/stellar spectral analysis. It was clear that the observed abundance pattern cannot be described by a single nucleosynthesis model. The different nucleosynthesis processes were already proposed by B2FH [Burb57] following the atomic abundance curve from Suess and Urey [Sues56]. The classification was based on the mass of the element, stellar conditions and observational evidences. Nucleosynthesis is the process by which new atomic nuclei are formed from preexisting protons and neutrons, the nucleons. The primordial nuclei like H, D, He and Li originated in the big bang. All of the heavier nuclides with  $A \geq 12$  were produced later in the stellar interiors.

The first stage in the nucleosynthesis is the fusion process which effectively converts hydrogen to helium. The helium nuclei are produced mainly either by the proton-proton chain reaction [Beth38] or the CNO cycle [Beth39] in which four protons fuse using carbon, nitrogen and oxygen isotopes as a catalyst to produce one  $^4\text{He}$  nucleus, two positrons and two electron neutrinos. For stars with the size of sun or smaller, the proton-proton chain reaction dominates whereas for the stars heavier than about 1.5 times the mass of the sun, the CNO cycle is more important.

The  $^4\text{He}$  ashes of hydrogen burning then become the fuel for helium burning, where helium nuclei combine to form  $^{12}\text{C}$  and  $^{16}\text{O}$ . For a star with a mass similar to the sun this is the last burning stage. After throwing off much of its envelope as a planetary nebula, such a star will ultimately become a white dwarf, supported against gravitational collapse by the outward pressure of its degenerate electrons and slowly starts to cool. For more massive stars, subsequent stages of stellar evolution produce successively heavier nuclei from  $^{12}\text{C}$  and  $^{16}\text{O}$  by carbon, neon, oxygen and silicon burning. These processes are responsible for the synthesis of most of the nuclei from neon to somewhat beyond iron.

A simple schematic representation of the evolution of a massive star ( $M \approx 25M_{\odot}$ ,  $M_{\odot}$  - mass of the sun) is given in Fig. 2.1. As illustrated, the evolution of the central regions of a massive star is made of successive thermonuclear burning stages and phases of gravitational contraction

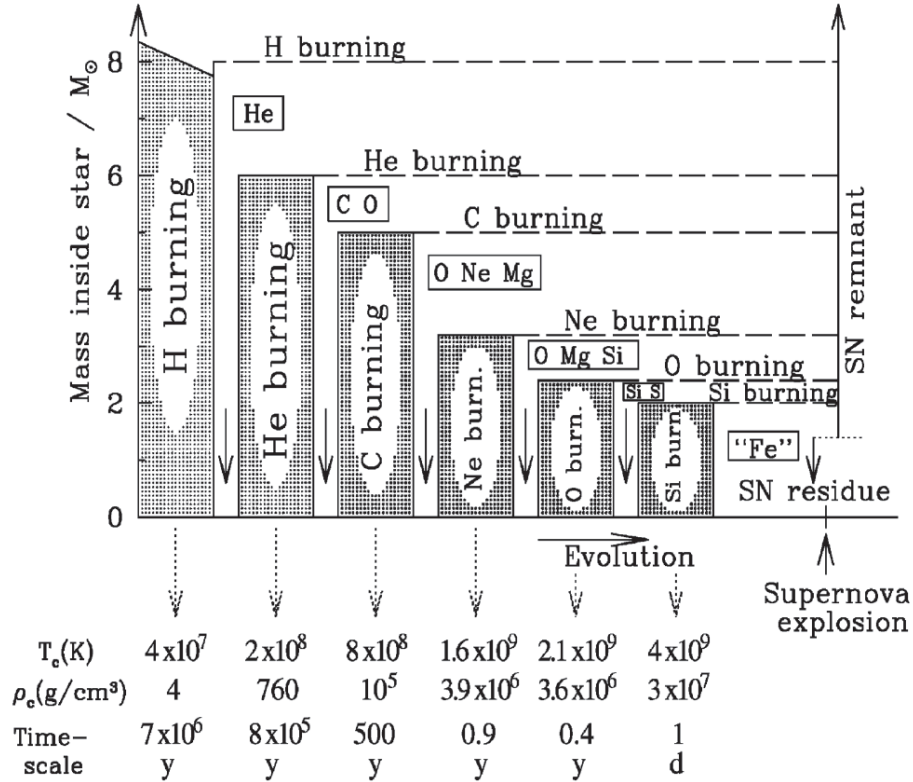


Figure 2.1: Schematic representation of the evolution of the internal structure of a spherically-symmetric massive ( $M \approx 25M_\odot$ ) star (from [Arno03]). The nuclear burning stages are given by shaded zones. A given burning phase starts in the central regions and then migrates into thin peripheral burning shells. The central temperatures  $T_c$ , central densities  $\rho_c$  and time scales of the core burning phases are also indicated. The downward arrows denote episodes of gravitational contraction.

and heating. The star, in general, is a bound object which self-confined by its own gravity according to the virial theorem. As per the theorem, the total kinetic energy for a star in hydrostatic equilibrium is equal to one half the total potential energy by magnitude. Using the virial theorem, for a given radius of collapse, one could make a prediction of the temperature of the hydrogen gas in terms of the kinetic energy and could make a prediction about when it would reach the ignition temperature for hydrogen fusion.

The first burning stages produce energy through charged-particle induced reactions. In the latter phases, the temperature increases from several tens of  $10^6$  K to about  $4 \times 10^9$  K. The iron-peak nuclei with  $50 \leq A \leq 60$  are shown with the chemical symbol 'Fe'. Finally, the iron core explodes in a catastrophic explosion referred to as a core collapse supernova (CCSN) event. In a CCSN event, the most central parts generally leave a residue (neutron star or black hole) whereas the rest of the stellar material is ejected into the interstellar space.

## 2.2 Nucleosynthesis beyond iron

Elements up to iron are formed in the stellar interiors by the charged-particle-induced reactions starting with hydrogen and helium burning. The element abundances show an exponential decrease with the exception of a sharp peak at iron ( $A=56$ ). Beyond iron, the heavy elements



are formed by successive neutron captures using prevailing neutron fluxes in the stellar interiors. Depending on the time scale, temperature and neutron densities, these are quantified as s- and r- processes. The p-process is responsible for the formation of the neutron deficient nuclei which are shielded from the neutron capture processes.

The heavy nuclide abundance distribution splitted into three separate curves for s-, r- and p-nuclides is given in Fig. 2.2. From the figure, one could infer that about half of the heavy nuclei in the solar material comes from the s-process, and the other half from the r-process. The abundances of the p-nuclei are in the order of (0.0-1%), a factor of  $\approx 100$  smaller than the adjacent r- or s- species. The three different processes are described in detail in the following sections.

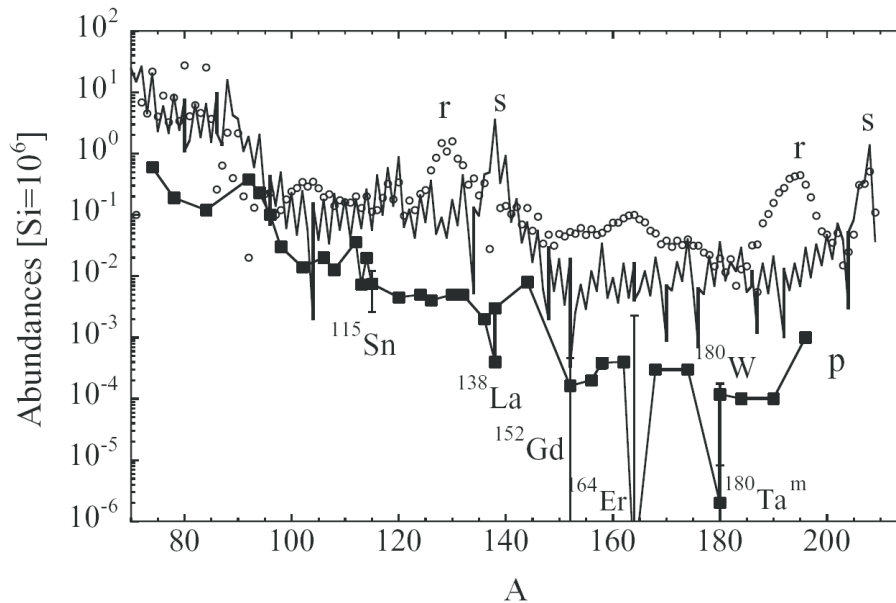


Figure 2.2: Solar abundances of trans-iron elements splitted into different components. The different contributions are from s-process (solid line), r-process (open circles) and p-process (squares). Vertical bars represent the uncertainties on the abundances of some nuclides due to a possible s-process contamination (from [Arno03]).

### 2.2.1 The s-process

The s-process is the slow neutron capture process which occurs on a time scale ranging from  $\sim 100$  years to  $\sim 10^5$  years. In this process, the time between successive neutron captures is much larger than the lifetimes of intervening beta-decays. The s-process peaks in the solar abundance distribution are at  $A = 90, 138$  and  $208$ . For a detailed review of the s-process nucleosynthesis, see [Kaep99].

The resulting isotopic abundances from the s-process chains are inversely proportional to the neutron capture reaction rates. For the closed neutron shell isotopes, the neutron capture rates are small and hence they peak up in the solar-system abundance distribution.

There are two components which explain the observed s-process abundance distribution -the main and the weak. The main component is responsible for the production of elements between Zr and Bi. The production site of the main component is the low mass asymptotic giant branch (AGB) stars. For a star in the AGB stage ( $M_{\odot} \leq M \leq 8M_{\odot}$ ), the core of extremely

dense carbon and oxygen is surrounded by a helium-burning shell which periodically ignites in a violent helium-flash [Boot06]. The neutron sources producing neutrons for main s-processing are  $^{13}\text{C}(\alpha, n)^{16}\text{O}$  and  $^{22}\text{Ne}(\alpha, n)^{25}\text{Mg}$ . Isotope production is directly proportional to the rates of these reactions. The synthesized elements are dredged to the star's surface where they can be observed and are ejected into the interstellar medium by stellar wind. The weak s-process component synthesizes s-process isotopes of elements from the iron group up to Sr and Y and takes place at the end of helium and carbon-burning in massive stars. These massive stars will become supernovae at their final stages and eject the s-nuclei into interstellar space.

Experimentally, there have been extensive efforts to study the s-process nuclei and neutron-capture cross sections are now available for a wide range of isotopes [Bao00, Dill06]. Due to the long half-life of the branching-point nuclei along the s-process path, it is hard to study the direct capture reaction on these isotopes. Alternatively, the neutron-capture cross sections of the s-process nuclei are derived by studying the inverse reaction ( $\gamma, n$ ) of the stable neighboring nucleus. In this regard, exciting results have been published from the experiments at the S-DALINAC accelerator facility in Darmstadt [Sonn03, Muel06].

### 2.2.2 The r-process

The r-process, as the name indicates, is the rapid neutron capture in which the interval between captures is much shorter than the lifetime for beta decay. The rapid capture takes place under the environment of high temperature ( $\sim 10^9$  K), high neutron density ( $> 10^{20} \text{cm}^{-3}$ ) and short time scales (0.01-10 s).

The r-process peaks at mass numbers  $A=130$  and  $195$ , about 10 units away from the s-abundance peaks at  $A=138$  and  $208$ . These are caused by the neutron magic numbers  $N=50, 82$  and  $126$ . The neutron magic nuclides accumulate far away from the valley of stability whereas the s-process nuclei were located close to the valley of stability. Later on, after termination of the neutron flux in the r-process, the extremely neutron-rich isotopes decay back to the valley of stability. The abundance maxima for r-process are located in mass regions below the corresponding s-process abundance peaks.

In the r-process, the abundance maximum in each isotopic chain is identified with nuclides of even neutron number. In a particular isotopic chain where the rate of capture is balanced by the rate of photodisintegration (waiting point approximation), the even- $N$  isotopes show the significant abundances and represent the waiting points. The isotopic equilibrium abundance of each element is determined by the corresponding neutron capture  $Q$ -values. The further transfer of matter to the adjacent isotopic chains proceeds through  $\beta^-$  decays. Then again another equilibrium within the corresponding chain is formed and the repetitive sequence gives rise to the r-process path. One thing to be noted is that the relative amount of r-process nuclide abundance is not correlated with its neutron capture cross section; instead to the total  $\beta^-$  decay probabilities of the isotopic chains.

The above referred conditions hold together for the classical r-process model which describes the behavior of the r-abundance distribution in the solar system. The astrophysical sites are mostly massive stars which provide high neutron densities and sufficiently high temperatures over short time scales. The possible sites for r-nuclei production include merging neutron stars, magnetized jets from asymmetric massive star explosions and neutrino-powered wind from type II supernovae. However, at present the astrophysical site of the r-process is under debate. An overview of the studies on r-process nuclei are given in [Cowa91].

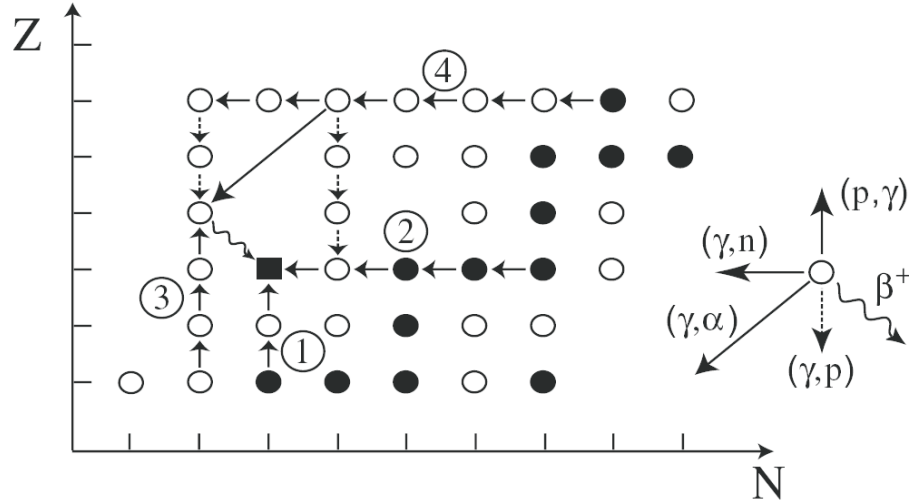


Figure 2.3: The possible routes for the formation of p-nuclides (black square) from r- or s-seeds (black dots). Unstable nuclei are represented by open dots. For details, see text.

### 2.2.3 The p-process

From the previous sections, we have seen that about 50% of the observed abundances could be reproduced well in the network calculations by the s- or r-processes. However, the group of 35 neutron-deficient nuclei between  $^{74}\text{Se}$  and  $^{196}\text{Hg}$  are shielded from the r- or s-process by stable isobars. These are classically referred to as the p-nuclei. A detailed description of the p-process nucleosynthesis is given in Refs. [Lamb92, Arno03].

The abundance distribution peaks at  $^{92}\text{Mo}$ ,  $^{112}\text{Sn}$  and  $^{144}\text{Sm}$  (see Fig. 2.2). The astrophysical production sites as well as the experimental needs for the *nuclear astrophysics p-nuts* ([Arno03]) will be discussed in the following sections.

## 2.3 The p-nuts in detail

From Fig. 2.2, it is evident that p-elements do not exist while some elements have their abundances dominated by a r- or s-nuclide. The solar system abundances of the p-nuclides are given in Table 1 of Ref. [Arno03]. It has been a great challenge to categorize the astrophysical scenarios contributing to the p-nuclei synthesis. There are three different processes by which the p-nuclei are produced - the  $\gamma$ -process (photodisintegration), the rp-process and the neutrino process.

For the p-process modeling, precise knowledge of the astrophysical reaction rate is necessary. The present astrophysical reaction rates exist only from statistical model calculations. The astrophysical reaction rates for p-nuclei were investigated by [Rapp06] using a full nuclear reaction network for a Type II supernova explosion. The impact of nuclear reaction rates on the predicted p-process abundances were tested by using simulations for different sets of collectively and individually modified neutron-, proton-, and  $\alpha$ -capture and photodisintegration rates. The results of the simulations reveal the extreme importance of experimental studies on p-nuclei to test the input parameters of model calculations. In the following subsections, the different modes of p-nuclei production and experimental attempts to investigate the p-nuclei will be described.

### 2.3.1 Production of p-nuclides

The observed abundances of the p-nuclei are mainly from the analysis of the class of meteorites called *carbonaceous chondrites*. The elemental and isotopic abundances were tabulated by Anders and Grevesse [Ande89].

As already mentioned, one of the modes for p-nuclei formation is the photodisintegration of previously existing r- or s- seed nuclei. For initiating the  $\gamma$ -process, a hot photon environment ( $\sim 2\text{-}3$  GK) is necessary. In such a hot *photon bath*, the high energetic photons in the tail of the Planck spectrum can induce photodisintegration reactions like  $(\gamma, n)$ ,  $(\gamma, p)$  and  $(\gamma, \alpha)$  on seed nuclei. A very schematic way of four different possible routes through which seed s- or r-nuclides can be transformed into p-nuclides is given in Fig 2.3 (taken from [Arno03]). The succession of  $(p, \gamma)$  or  $(\gamma, n)$  reactions leading to the formation of p-nuclides are indicated by routes (1) and (2). The p-nuclide formation via slightly complicated routes are -  $(p, \gamma)$  reactions followed by  $\beta$ -decays (3) and combination of  $(\gamma, n)$  and  $(\gamma, p)$  or  $(\gamma, \alpha)$  and  $\beta$ -decays (4).

The temperature and timescale should be ideal for photon induced reactions, but should not sustain for a long time which would result in all seeds decaying back to the iron peak nuclei. An ideal site for p-process is thus a *core collapse supernova event*, the final stage of stellar burning in a spherically-symmetric massive star (see Fig. 2.1). Examples are types Ib, Ic, and type II supernovae which result from the collapse of the iron core of a massive star at the end of its life. The photodisintegration along a particular isotopic chain depends on the decay constants for the ejection of neutrons, protons or alpha particles. In the isotopic chain, while moving to the neutron-deficient nuclei, the  $(\gamma, n)$  threshold increases. The energy required to remove a proton or alpha particle is smaller and hence  $(\gamma, p)$  and  $(\gamma, \alpha)$  will dominate over the  $(\gamma, n)$  reactions. Such a situation is marked as the *branching point*. Generally, the even-N nuclei in an isotopic chain tend to be the branching points where the material accumulates and it turns into a p-nucleus except for a few cases. The  $\beta$ -decays are much slower and are negligible. The  $(p, \gamma)$  or  $(\alpha, \gamma)$  reactions don't play a role in the  $\gamma$ -process.

The most favored scenario for the p-nuclei production are O-Ne-rich layers of a massive star and the p-process flow occurs when the shock wave passes through the layer resulting in different temperatures for different zones. It has been shown that the p-nuclei with masses  $92 \leq A \leq 144$  are mainly produced in the stellar zones with temperature range 2.5-3.0 GK. Except for a few discrepancies, the solar system abundances of the p-nuclei have been reproduced within a factor of 3 [Haya04].

The synthesis of some of the lighter p-process nuclides such as isotopes of Mo and Ru was not reproduced in the  $\gamma$ -process models. The two other possible mechanisms suggested were rp-process and neutrino-induced nucleosynthesis. The rapid proton capture process (rp-process) consists of consecutive proton captures onto the seed nuclei to produce heavier elements and it occurs on the proton-rich side of the valley of stability [Wall81].

The main production sites of rp-process are associated with the thermonuclear explosions in accreting binary star systems - novae, X-ray bursts and Type Ia supernovae. In a binary system of a high and low mass star, the higher mass star will evolve faster and will eventually become a compact object - either a white dwarf star, a neutron star, or a black hole. Later on, the lower mass star evolves into an expansion phase and when it is so close to the compact star its outer atmosphere actually falls onto the compact star. This creates an accretion disk which is rich in hydrogen and helium and temperatures are typically around  $10^8\text{K}$ . Gas in this accretion disk heats up, and eventually falls onto the compact star. The runaway thermonuclear explosion leads to the rp-process which is generally observed in neutron star binaries as an X-ray burst. The third mechanism of p-nuclei production, the neutrino-process occurs in the high neutrino

flux produced by the protoneutron star in a core-collapse supernovae [Woos90]. In the  $\nu$ -process certain nuclides can be made by neutrino-induced spallation of nuclei in the outer shells of a massive star during a supernova explosion. This can affect the abundances of r-process nuclei, especially those on the lower-mass side of the r-process peaks, and produce a significant abundance of rare isotopes like  ${}^7\text{Li}$ ,  ${}^{11}\text{B}$ ,  ${}^{19}\text{F}$ ,  ${}^{138}\text{La}$ , and  ${}^{180}\text{Ta}$ . It may also produce light p-nuclei such as  ${}^{92}\text{Mo}$ . The cross sections for the relevant neutrino-induced reactions can be deduced from inelastic hadron scattering and charge exchange studies at fragmentation facilities.

In order to explain the existence of Sr and other elements beyond Fe in the very early stage of galactic evolution, a new light element primary process (LEPP) named  $\nu p$  process has been proposed by [Froe06]. It could contribute to the nucleosynthesis of the light p-nuclei as well. The relevant astrophysical sites for the  $\nu p$  process are the inner ejecta of core collapse supernovae or winds from the accretion disk in the collapsar model of gamma-ray bursts. The neutrino-induced nucleosynthesis of the nuclei with  $A > 64$  has been discussed in detail by Froehlich et al. [Froe06].

### 2.3.2 Experimental situation

As already mentioned, the information on experimental reaction rates involved in the p-process nuclear flows are very scarce. The experimental information available so far is either from reactions that involve neutrons or charged particles.

The p-nuclei studies by photon-induced reactions have the limitation that they concern stable targets only. In order to calculate the stellar rates, one needs to take into account that the nuclei can be in excited states in the stellar environment. However, the ground state reaction rates themselves are extremely important since they are used to validate the nuclear physics inputs to theoretical model calculations. The  $(\gamma, n)$  cross sections have been directly measured at energies around the giant dipole resonance (GDR) [Diet88]. These are not of direct astrophysical relevance. The experimental data of importance to the p-nuclei lie close around the photodisintegration threshold and this energy region have been investigated using bremsstrahlung photons at the S-DALINAC facility in Darmstadt [Mohr00, Sonn04]. The technique used at Darmstadt is based on the principle that the superposition of bremsstrahlung spectra with different end-point energies yields a  $\gamma$ -ray distribution that can approximate a black-body Planck spectrum at a given temperature. For example, this method has been used to measure the cross section of  ${}^{198}\text{Pt}(\gamma, n){}^{197}\text{Pt}$  reaction at energies of astrophysical interest [Vogt01]. Recently, there has been interesting experimental results from the S-DALINAC experiment regarding the photodisintegration reactions of the isotopes in the rare-earth region [Hasp08a, Hasp08b]. The photoneutron cross sections of  ${}^{148,150}\text{Nd}$ ,  ${}^{154}\text{Sm}$ ,  ${}^{154,160}\text{Gd}$  close to the neutron emission threshold has been determined and compared to the statistical model calculations.

Another method to probe the photon-induced reactions is by using the Laser Inverse Compton scattering (LIC) technique which can produce quasi-monochromatic  $\gamma$ -rays. The major advantage of this method is the availability of high intense  $\gamma$ -rays in the energy window of astrophysical interest, i.e., close to the neutron threshold. The method has been used to measure the rates of some astrophysically relevant  $(\gamma, n)$  reactions [Utsu03, Utsu06]. In particular, the  ${}^{181}\text{Ta}(\gamma, n){}^{180}\text{Ta}$  cross section has been measured which is of special importance for the p-process modeling [Utsu03].

The experimental data on charged-particle induced reactions like  $(p, \gamma)$  and  $(\alpha, \gamma)$  are scarcer than the reactions involving neutrons due to the extremely low cross sections at the sub-Coulomb energies of astrophysical interest. The  $(p, \gamma)$  cross sections of interest to the p-process

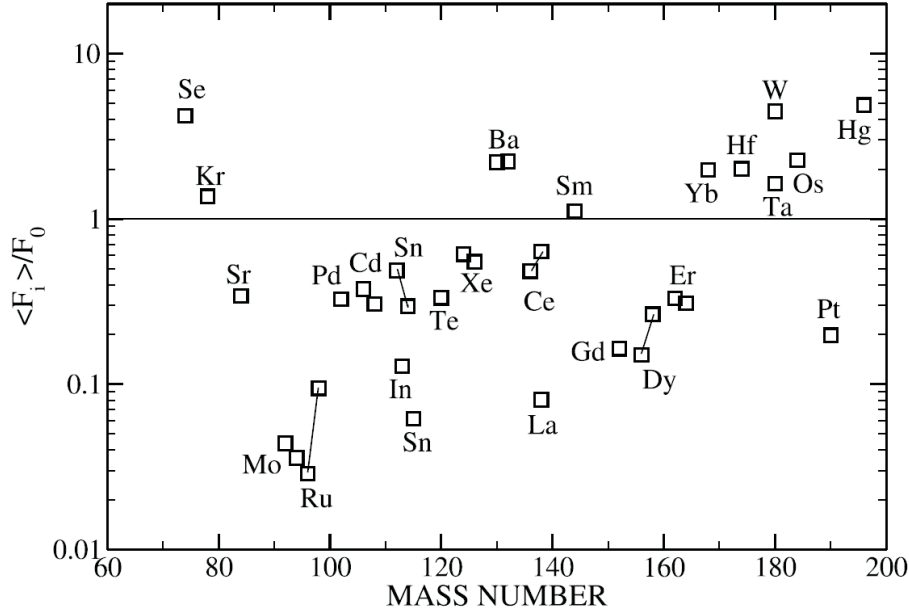


Figure 2.4: Averaged normalized overproduction factor for the neutron-deficient p-nuclei from network calculation with standard reaction rates (from [Rapp06]). The factor is defined to be equal to unity when the simulated abundances match with the observed solar values.

have been measured using the activation method or in-beam measurements [Gyur01, Gyur03, Gala03, Chlo99, Haris01, Saut97]. Experimental data are available only for stable targets up to about Sn and an extension towards  $Z > 50$  targets is on high demand since it will provide the stellar  $(\gamma, p)$  reaction rates through the reciprocity theorem. The experimental data on  $(\alpha, \gamma)$  reactions are even fewer- the only reactions that have been studied at sub-Coulomb energies are the  $(\alpha, \gamma)$  reactions on  $^{70}\text{Ge}$  [Fulo96],  $^{96}\text{Ru}$  [Rapp01],  $^{112}\text{Sn}$  [Ozka02] and  $^{144}\text{Sm}$  [Somo98]. The  $^{144}\text{Sm}(\alpha, \gamma)^{148}\text{Gd}$  reaction has been measured using an activation method based on the off-line  $\gamma$ -activity measurement of the  $^{148}\text{Gd}$  residual nucleus and is of special astrophysical interest. The cross sections and astrophysical S-factors have been measured at low energies which are important in the modeling of the  $\alpha$ -nucleus optical potentials (see [Somo98]). A summary of the experimental approaches and associated problems involved in p-nuclei studies are given in [Arno03, Mohr07].

## 2.4 The p-nuclei $^{92}\text{Mo}$ and $^{144}\text{Sm}$

As already discussed in Sect.2.3.1, the present models for the p-nuclei production call for its development in the O/Ne rich layers of Type II supernovae. The average normalized overproduction factor  $\langle F_i \rangle / F_0$  for the p-nuclei from recent calculations by [Rapp06] performed with a multilayered model adopting the seed of a pre-explosion evolution of a  $25M_{\odot}$  star is given in Fig. 2.4. The overproduction factor  $\langle F_i \rangle$  gives the efficiency of a particular nucleosynthesis process in contributing to the observed solar abundance distribution.  $F_0$  ( $\sum \frac{\langle F_i \rangle}{35}$ ) is the averaged overproduction factor for the 35 p-only nuclides. Even though this model successfully reproduces the solar system abundances, the light Mo ( $^{92}\text{Mo}$ ,  $^{94}\text{Mo}$ ) and Ru ( $^{96}\text{Ru}$ ,  $^{98}\text{Ru}$ ) isotopes are still underproduced.

Despite the considerations for the contributions from other nucleosynthesis processes (rp-

process,  $\nu p$  process), the underproduction phenomena is still the main enigma in p-process simulations. There has been an interesting proposal from Costa et al. [Cost00] that this underproduction could be related to the uncertainties left in the rate of the neutron producing reaction  $^{22}\text{Ne}(\alpha, n)^{25}\text{Mg}$ . This reaction is the key neutron producer and has a direct impact on the predicted abundances of the s-seeds for the p-process. It has been suggested that the problem of underproduction could be cured if the  $^{22}\text{Ne}(\alpha, n)^{25}\text{Mg}$  rate is increased by factors of about 5-10 with respect to the proposed rates in NACRE compilation [Angu99]. However, the experiment from Jaeger et al. [Jaeg01] provided a  $^{22}\text{Ne}(\alpha, n)^{25}\text{Mg}$  rate which is roughly equal to the NACRE rate for  $2\text{-}3 \times 10^8$  K. This leads to the conclusion that the underproduction of Mo and Ru isotopes is not related with the  $^{22}\text{Ne}(\alpha, n)^{25}\text{Mg}$  rate and leaves it as an open problem. The other possible contributions which could account for the measured  $^{92,94}\text{Mo}$  and  $^{96,98}\text{Ru}$  abundances are currently under investigation. It is thus highly favorable to have experimental information regarding these nuclei.

The nuclide  $^{144}\text{Sm}$  has been in the frame of the p-process chronometer  $^{146}\text{Sm}$  [Audo72]. The nuclides  $^{144}\text{Sm}$  and  $^{146}\text{Sm}$  were identified as a pure p-process chronometer pair. The p-process chronology, in general, would provide information about when the process occurred which in turn will shed light on the astrophysical sites of p-nuclei formation. There were several efforts to determine the  $^{146}\text{Sm}/^{144}\text{Sm}$  production ratio experimentally which varies due to uncertainties in different inputs entering the calculation, see [Somo98]. One of the important nuclear physics input is the proper optical potential at energies of astrophysical relevance which has been derived from  $^{144}\text{Sm}(\alpha, \alpha)^{144}\text{Sm}$  elastic scattering [Mohr97].

The nuclear-physics-related uncertainties in the p-process model predictions were investigated recently by Rapp et al [Rapp06]. A list of the most critical p-process reaction rates (with their respective inverse reactions) which will influence the final p-abundances is given (see Table 2 and Table 3, [Rapp06]). The  $^{92}\text{Mo}(\gamma, p)^{91}\text{Nb}$  and  $^{156}\text{Er}(3\gamma, 3\alpha)^{144}\text{Sm}$  reactions were among the list of the reaction chains which strongly influence the p-process flow. In general, systematic investigation of the  $(\gamma, \alpha)$  reactions in the mass region  $A \geq 140$  is found to be very important. Experimental information on these rates is necessary for reducing the inherent nuclear model uncertainties.

In the scope of this thesis work, the  $(\gamma, n)$ ,  $(\gamma, p)$  and  $(\gamma, \alpha)$  reactions on  $^{144}\text{Sm}$  have been investigated via photoactivation method for the first time at energies of astrophysical interest. The  $(\gamma, p)$  and  $(\gamma, n)$  reactions on  $^{92}\text{Mo}$  are discussed in detail in the thesis work of [Erha09]. The  $^{92}\text{Mo}(\gamma, \alpha)$  experiments will be discussed in the following chapters.





# Chapter 3

## Photodisintegration via real photons at ELBE

The photodisintegration experiments were performed at the photoactivation facility of the ELBE accelerator of the Forschungszentrum Dresden-Rossendorf, Dresden. ELBE serves as an outstanding bremsstrahlung facility with intense photon beams of endpoint energies between 6 and 18 MeV. These beam parameters provide a unique environment to probe photon-induced reactions.

The p-nuclei  $^{92}\text{Mo}$  and  $^{144}\text{Sm}$  were studied using the photoactivation technique. In this chapter, the photoactivation facility will be presented in detail. The second part of this chapter is dedicated to the description of the photon flux and bremsstrahlung endpoint energy determination procedures adopted for this work.

### 3.1 The ELBE accelerator

The radiation source ELBE (Electron Linac of high Brilliance and low Emittance) delivers multiple secondary beams, both electromagnetic radiation and particles. ELBE is in operation since 2003 and delivers continuous wave electron beams with a maximum energy of 40 MeV at a maximum average current of 1 mA [Gabr00]. Electrons are pre-accelerated in a 250 keV-thermionic DC electron-gun and pre-bunched in two Radio-Frequency (RF) buncher sections. Main acceleration is accomplished in two 20 MeV-superconducting linear accelerator modules operated at 1.3 GHz. Each accelerator module uses standing wave RF cavities designed for the TESLA test facility at DESY<sup>1</sup>. Two 9-cell superconducting niobium cavities are operated in a cryo-module with superfluid liquid helium at a temperature of 1.8 K. Each cavity is driven by a 10 kW klystron amplifier. The maximum accelerating gradient is 15 MV/m. There is an electromagnetic chicane between the two modules which optimizes the micropulse duration and energy spread of the beam.

A schematic layout of the ELBE facility is given in Fig. 3.1. The different experimental facilities associated with the ELBE accelerator are also shown. The bremsstrahlung facility is located before the second linac module (the nuclear physics cave, see Fig. 3.1). The electron beam is deflected from the main path and hits the radiator producing bremsstrahlung. The beam parameters used for bremsstrahlung experiments are given in Table. 3.1.

---

<sup>1</sup>Deutsches Elektronen-Synchrotron, Hamburg, Germany.

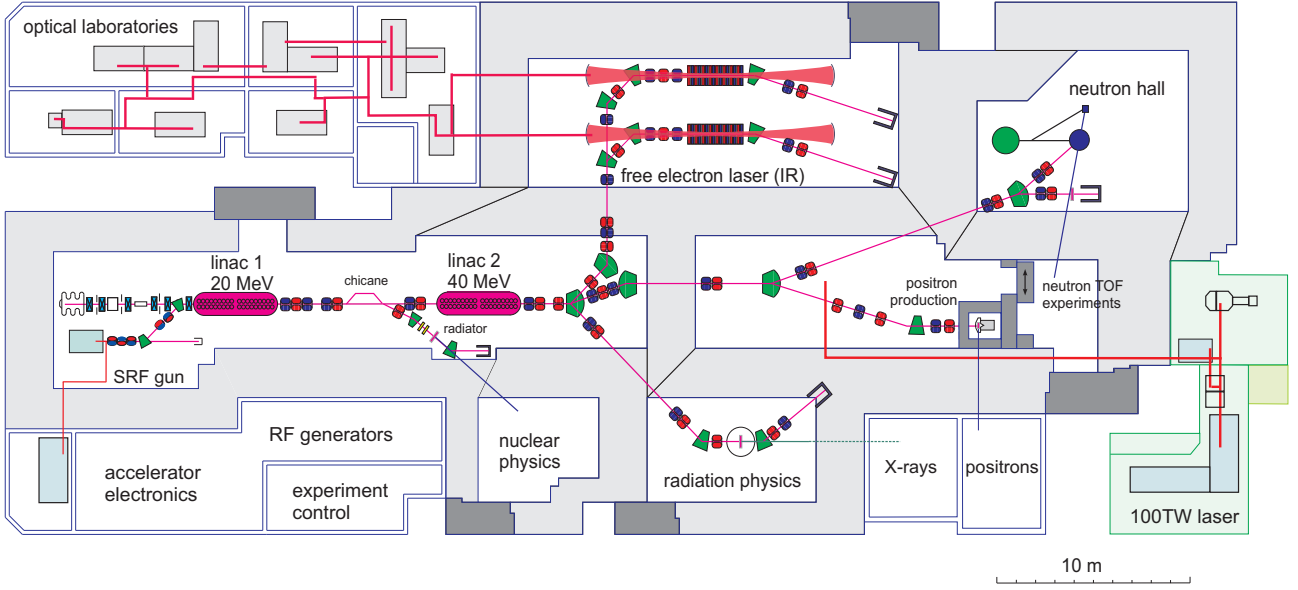


Figure 3.1: A schematic layout of the ELBE accelerator and associated facilities. Before linac 2, the electron beam is deflected out of the main beam line to the Nuclear Physics cave for production of bremsstrahlung. The dipole magnets are marked in green, vertically focussing quadrupoles in red and horizontally focussing quadrupoles in blue.

Electron beam energy	6 – 18 MeV
Max. bunch charge	58 pC
Max. average beam current	750 $\mu$ A
Micropulse duration	5 ps
Micropulse repetition rate	13 MHz

Table 3.1: Beam parameters used for bremsstrahlung experiments at the ELBE accelerator.

## 3.2 Photoactivation method

The photoactivation method essentially consists of two steps

1. irradiation of the target nuclei (e.g.  $^{92}\text{Mo}$ ,  $^{144}\text{Sm}$ ) of interest,
2. decay measurement of the daughter nuclei resulting from photoactivation.

The irradiation is performed in a highly intense photon beam. The number of radioactive nuclei  $N_{\text{act}}(E_0)$  produced is proportional to the integral of the absolute photon fluence (time integrated photon flux)  $\Phi_\gamma(E, E_0)$  times the photodisintegration cross section  $\sigma_{\gamma,x}(E)$ . The integral runs from the reaction threshold energy  $E_{\text{thr}}$  up to the endpoint energy  $E_0$  of the bremsstrahlung spectrum. The symbol  $x = n, p, \alpha$  denotes the emitted particle.

$$N_{\text{act}}(E_0) = N_{\text{tar}} \cdot \int_{E_{\text{thr}}}^{E_0} \sigma_{\gamma,x}(E) \cdot \Phi_\gamma(E, E_0) dE \quad (3.1)$$

After irradiation, the  $\gamma$ -rays following the  $\beta$ -decays of the radioactive sample are measured using High Purity Germanium (HPGe) detectors. The number of radioactive nuclei  $N_{\text{act}}(E_0)$

is determined using the formula:

$$N_{\text{act}}(E_0) = \frac{N_{\gamma}^{\text{corr}}(E_{\gamma}, E_0) \cdot \kappa_{\text{corr}}}{\varepsilon(E_{\gamma}) \cdot p(E_{\gamma})} \quad (3.2)$$

$N_{\gamma}^{\text{corr}}(E_{\gamma}, E_0)$ ,  $\varepsilon(E_{\gamma})$  and  $p(E_{\gamma})$  denote the dead-time and pile-up corrected full-energy peak counts of the observed transition, the absolute photopeak efficiency of the detector at the energy  $E_{\gamma}$  and the emission probability of the photon with energy  $E_{\gamma}$  respectively.

The factor  $\kappa_{\text{corr}}$  in Eq. (3.2) is given by

$$\kappa_{\text{corr}} = \frac{\exp\left(\frac{t_{\text{loss}}}{\tau}\right)}{1 - \exp\left(\frac{-t_{\text{meas}}}{\tau}\right)} \cdot \frac{\frac{t_{\text{irr}}}{\tau}}{1 - \exp\left(\frac{-t_{\text{irr}}}{\tau}\right)} \quad (3.3)$$

This expression determines the number of radioactive nuclei from their decays measured during the time  $t_{\text{meas}}$ . It also takes into account decay losses during irradiation ( $t_{\text{irr}}$ ) and in between end of irradiation and beginning of measurement ( $t_{\text{loss}}$ ).  $\tau$  denotes the mean life time of the radioactive nucleus produced during the photoactivation.

For the  $(\gamma, x)$  reaction ( $x=n, p$  or  $\alpha$ ), the activation yield is denoted by  $Y_{\text{act}}$  and is expressed as the ratio of the number of activated nuclei to the number of target atoms in the sample. For example, for the  $^{144}\text{Sm}(\gamma, n)$  reaction,

$$Y_{\text{act}}(\text{Sm}) = \frac{N_{\text{act}}(^{143}\text{Sm})}{N_{\text{tar}}(^{144}\text{Sm})} \quad (3.4)$$

Using Eq. (3.1), the activation yield can be calculated from  $\sigma_{\gamma, n}(E)$  data with the known bremsstrahlung spectrum. In this way measured activation yields can be compared with the experimental or theoretical cross section data.

To compare the activation yield measured at different endpoint energies with the calculated yield using cross sections from theory/previous experiments, the experimental data need to be normalized to the photon fluence at the irradiation site. The irradiation site is the *photoactivation site* shown in Fig. 3.2 where the available photon fluence is very high and technically challenging to measure with in-beam detectors. The photon fluence is determined from the activation yield of a Au target that is irradiated simultaneously with the Mo/Sm targets. The photon fluence at a fixed energy  $E_{\gamma}$  is given by the ratio of the measured  $^{197}\text{Au}(\gamma, n)$  activation yield and the calculated activation yield using the known  $\sigma_{\gamma, n}$  from  $^{197}\text{Au}$  and a simulated thick target bremsstrahlung spectrum using the code MCNP (see Sect. 3.4.3), which is based on the bremsstrahlung cross sections by Seltzer and Berger. At the *photon scattering site* (see Fig. 3.2), the activation yield of  $^{197}\text{Au}(\gamma, n)$  was determined to verify the  $\sigma_{\gamma, n}$  cross section to be used for the photon fluence determination. There the photon flux is determined online via photon scattering from  $^{11}\text{B}$ . The photon flux determination procedure from  $^{11}\text{B}$  scattering will be discussed in detail in Sect. 3.4.

Rewriting Eq. (3.1), the activation yield for Sm is,

$$Y_{\text{act}}(\text{Sm}) = \Phi_{\gamma}(E_{\gamma}^{\text{X}}, E_0) \cdot \int_{E_{\text{thr}}}^{E_0} \sigma_{\gamma, x}^{\text{sim}}(E) \cdot \frac{\Phi_{\gamma}^{\text{sim}}(E_{\gamma}, E_0)}{\Phi_{\gamma}^{\text{sim}}(E_{\gamma}^{\text{X}}, E_0)} dE \quad (3.5)$$

where  $E_{\gamma}^{\text{X}}$  stands for any arbitrarily chosen energy. For the experiments discussed in this thesis, the normalization has been done to the fluence at  $E_{\gamma}^{\text{X}} = 7.288$  MeV which is below the bremsstrahlung endpoint energies for the photodisintegration experiments under discussion. The activation yield of the  $^{92,100}\text{Mo}(\gamma, n)$  reaction has been measured both at the photoactivation site and photon scattering site at ELBE [Erha09]. The two target sites (photoactivation site and photon scattering site) will be explained in detail in the following sections.

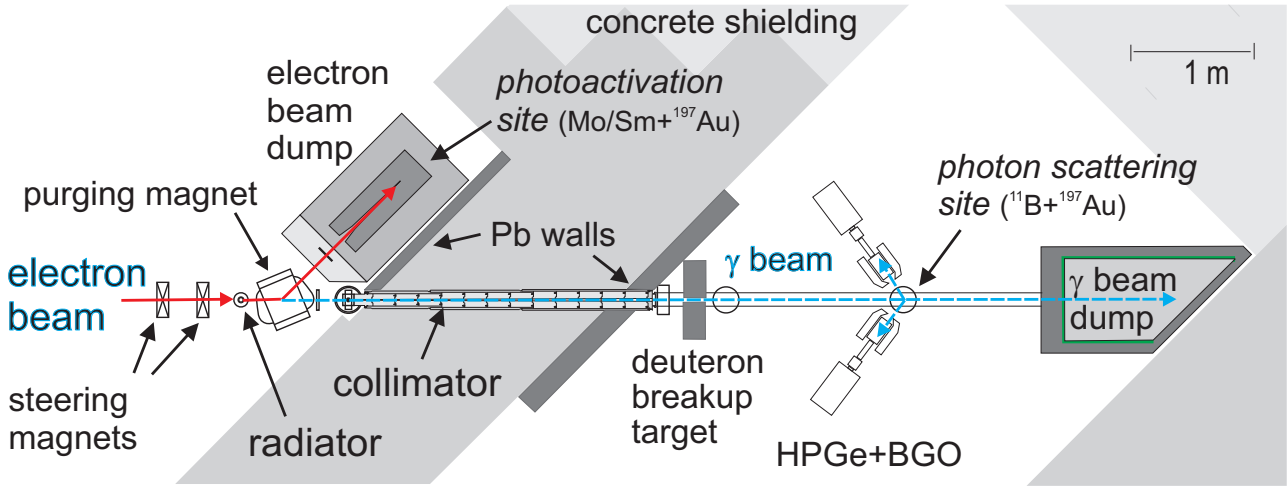


Figure 3.2: Photoactivation setup at the ELBE accelerator. The electron beam is deflected from the main beam line and creates bremsstrahlung in the radiator. There are two target sites: at the photoactivation site, the Mo and/or Sm targets are irradiated together with  $^{197}\text{Au}$  as a reference. At the photon scattering site, the scattered photons from  $^{11}\text{B}$  are observed for the experimental determination of the flux. Another  $^{197}\text{Au}$  target is sandwiched with  $^{11}\text{B}$  for flux normalization purposes. The experimental setup has been described in detail in [Schw05, Wagn05].

### 3.3 Photoactivation facility at the ELBE accelerator

A sketch of the photoactivation facility is given in Fig. 3.2. The primary electron beam is deflected from the main line by a non-dispersive system of two dipole magnets with a quadrupole magnet in between. There is another subsequent quadrupole doublet which focusses the beam on to the radiator producing bremsstrahlung via deceleration of electrons [Schi03a]. The radiator converts the kinetic energy of only a small fraction of the electrons to bremsstrahlung while the main fraction of the electrons passes the radiator and is separated from the photon beam by a deflecting dipole magnet (purging magnet, see figure). After deflection, the electron beam is led through a thin vacuum separation window made from beryllium and dumped into the electron beam dump (photoactivation site). The p-nuclei under investigation (Mo/Sm) are irradiated here together with the activation standard target  $^{197}\text{Au}$ . The bremsstrahlung beam goes straight ahead through the collimator to the photon scattering site.

At the photon scattering site, photons scattered from  $^{11}\text{B}$  are observed by means of High Purity Germanium detectors for the experimental determination of photon flux. The endpoint energy of the bremsstrahlung distribution is determined by measuring the proton energy spectrum from the photodisintegration of the deuteron (see Fig. 3.2, deuteron breakup target) with silicon detectors. The two target sites and the different components shown in Fig. 3.2 are described in detail in the following sections.

#### 3.3.1 Electron beam dump - The photoactivation site

After passing the niobium radiator, the electron beam is deflected by a dipole magnet and led through a vacuum separation window made from beryllium (thickness = 1 mm, diameter = 90 mm) into the electron beam dump, where the beam is stopped (See Fig. 3.3). The beam

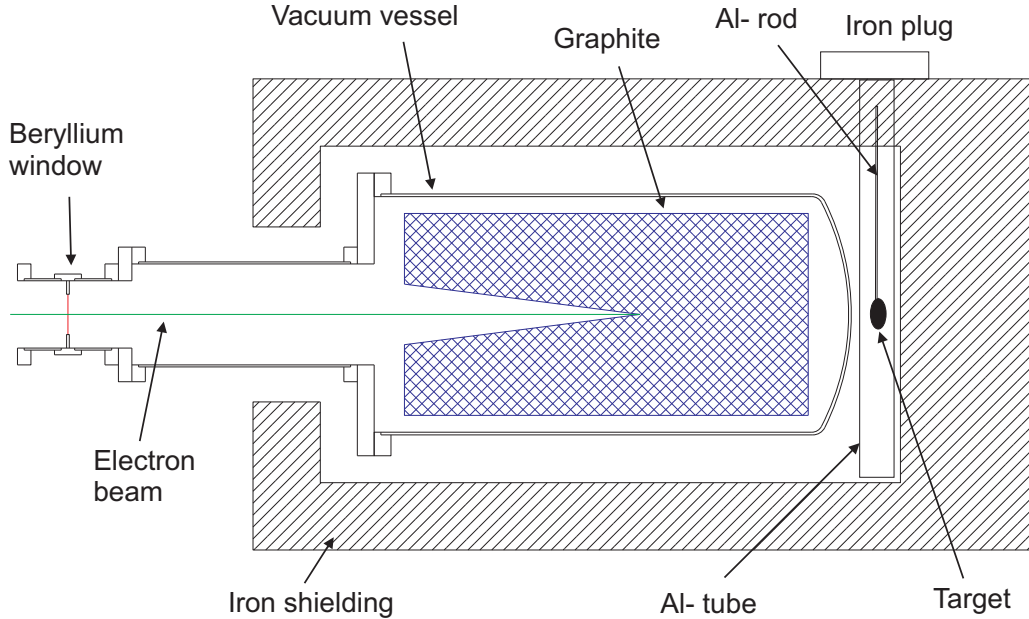


Figure 3.3: Photoactivation site at ELBE accelerator. The electron beam hits the carbon radiator and creates *thick* target bremsstrahlung. Molybdenum and/or Samarium targets are irradiated together with Au behind the beam dump.

separation magnet is a dipole magnet with a 117 mm gap [Schi03c]. The electron beam dump is made of a graphite cylinder of 600 mm length and 200 mm diameter which is mounted on insulating ceramic rods inside a double-walled water-cooled steel housing surrounded by a 10 cm thick radiation shield made of iron. The electron-beam dump is designed to have a maximum cooling power of 50 kW.

The activation targets (Mo/Sm +  $^{197}\text{Au}$ ) are placed behind the vacuum steel vessel as shown in Fig. 3.3. The target holder is made of an Al rod with a clamping bolt which is mounted in a cylindrical Al tube and inserted behind the vacuum vessel. To differentiate from the niobium radiator bremsstrahlung, we refer to the flux in the electron beam dump as *thick* target bremsstrahlung. It is not possible to measure the photon flux at this target position directly. The flux determination procedure is discussed in detail in Sect. 3.4.

### 3.3.2 The photon scattering site

At the photon scattering site, a  $^{11}\text{B}$  sample is irradiated together with the activation standard target  $^{197}\text{Au}$  in the bremsstrahlung beam. As already stated, the radiator for bremsstrahlung production is made of thin foils of niobium. In addition to being an appropriate Z material, it also has a high melting point ( $2468^\circ$ ) to withstand the absorbed beam power. The thickness of the foil is chosen according to the radiation lengths ranging from  $2 \times 10^{-4}$  to  $10^{-3}$  which keeps the small angle scattering low. Six radiator foils of varying thicknesses are mounted on a water-cooled copper holder [Schi03a]. The radiator holder can be moved by a DC motor drive which enables the selection of an appropriate radiator without breaking the vacuum. The electron-beam spot on the radiator is monitored by a video camera.

To extract a well-defined beam from the bremsstrahlung produced by the radiator, the beam is passed through a collimator (see Fig. 3.2). The collimator is made of high-purity aluminium (99.5 %) which has a high neutron separation energy of 13.1 MeV keeping the production

of background by neutrons small. Aluminium has a photon attenuation effect similar to the surrounding concrete walls. The collimator is 2600 mm in length and has an opening angle of 5 mrad [Schi02a]. It is fixed within the 1.6 m thick wall of heavy concrete between the accelerator hall and the experimental cave (see Fig. 3.2).

As a part of the radiation protection system, a beam shutter and hardener is positioned directly in front of the entrance aperture of the bremsstrahlung collimator. The beam shutter is used to shut the collimator entrance port against the background radiation from the accelerator hall and thus to shield the nuclear physics cave when the accelerator is in operation for other experimental caves. The beam hardener is used to suppress the low-energy photons in the bremsstrahlung spectral distribution. The bremsstrahlung spectrum for a particular incident electron energy is continuous with end-point energy equal to the kinetic energy of the incident electrons. The intensity is higher at low energies and it leads to a huge background in the measured spectra which in turn limits the counting rates of the HPGe detectors. The hardener improves the shape of the bremsstrahlung spectrum by absorbing the low energy photons. At ELBE, there is a vacuum chamber in front of the entrance of the collimator which contains a feed through with three cylinders of 10 cm diameter and 10 cm length made of TRIAMET<sup>2</sup>, of aluminium and of an aluminium cylinder of 9 mm diameter surrounded by TRIAMET, respectively. These cylinders are motor-driven and can be placed separately in the beam [Schi02b]. The TRIAMET cylinder is used to close the beam line (shutter), the aluminium cylinder is used as the hardener and the aluminium surrounded by TRIAMET works in a similar way with the tungsten acting as an additional collimator.

After passing through the scattering target, the bremsstrahlung beam is dumped into the photon beam dump in order to minimize the background from scattered photons. The photon-beam dump [Wagn01] is made of polyethylene (PE) and shielded with a 2 mm thick cadmium foil and 10 cm thick lead walls. The front lead wall has a thickness of 20 cm. The beam dump has an entrance hole of 11 cm in diameter. Because of the Compton scattering and the rather big entrance hole, the beam dump does not fully absorb the photon beam. For reducing the back-scattered radiation, a cylindrical void has been made in the PE block so that the scattering process starts deep inside the beam dump.

## 3.4 Determination of photon flux

As mentioned earlier, it is necessary to know the absolute photon flux at the photoactivation site for the activation yield normalization. It is not possible to measure the photon flux directly at this site using photon detectors placed in-beam. The flux determination procedure is explained in the following subsections in detail.

### 3.4.1 Spectral shape of bremsstrahlung

At the photon scattering site, the bremsstrahlung spectrum is well approximated with a theoretical bremsstrahlung distribution for a thin niobium target. A comparison of different theoretical approaches for an incident bremsstrahlung endpoint energy of 11.5 MeV is given in Fig. 3.4. The Schiff curve is created from the analytical expression given in [Schi51]. The bremsstrahlung spectrum using the approach by Seltzer and Berger [Selt86] which includes screening and Coulomb effects at higher energies is shown. The recent quantum mechani-

---

<sup>2</sup>TRIAMET- a composite material consisting of 95 % W, 5 % Ni and Cu; from Bayerische Metallwerke GmbH, Leitenweg 5, 85221 Dachau, Germany

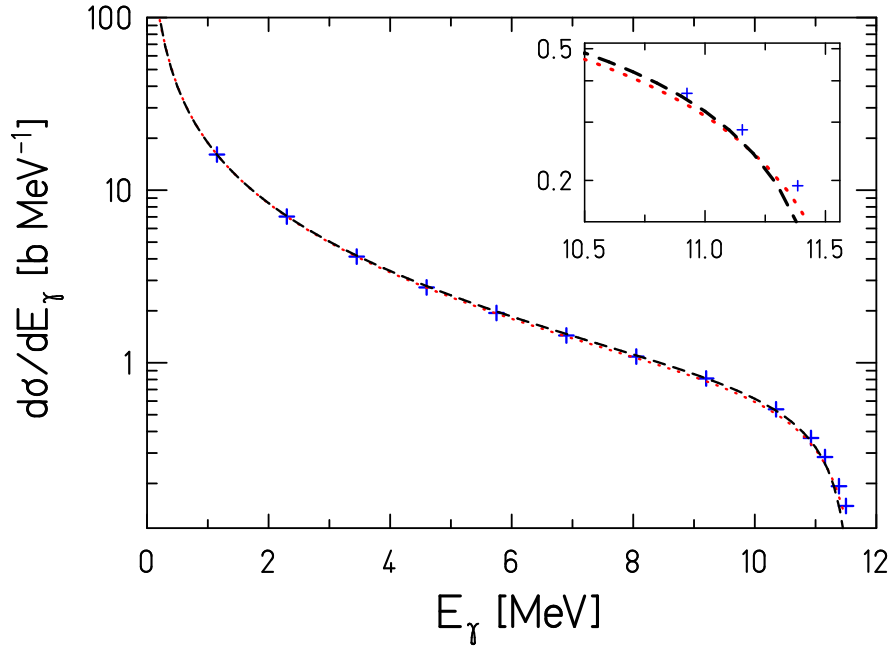


Figure 3.4: Comparison of theoretical bremsstrahlung cross sections for the Nb radiator for an incident electron endpoint energy of 11.5 MeV. Black dashed and red dotted lines correspond to the bremsstrahlung distributions by Schiff [Schi51] and Haug [Haug08] whereas values taken from the Seltzer and Berger [Selt86] tables are shown as blue symbols (+).

cal calculations by Haug [Haug08, Roch72] which uses the atomic shielding effects given in Ref. [Salv87] is also shown.

As seen in the figure, the different approaches are in agreement with each other. At the low-energy part of the spectrum they are not distinguishable from each other and agree within 1 percent. Close to the endpoint, the different models differ by about 20% (see inset, Fig. 3.4).

### 3.4.2 Photon scattering from $^{11}\text{B}$

In order to determine the photon flux experimentally, a  $^{11}\text{B}$  sample is sandwiched with the activation standard target ( $^{197}\text{Au}$ ) at the photon scattering site. The absolute photon fluence is determined by studying the  $^{11}\text{B}(\gamma, \gamma')$  reaction.

To detect scattered photons from  $^{11}\text{B}$ , four HPGe-detectors with 100% efficiency relative to a 3"×3" NaI detector are used [Schw03]. Two of them are placed vertically above and below the target respectively, while the other two are placed horizontally at 127 ° relative to the photon-beam direction. All HPGe detectors are surrounded by escape-suppression shields consisting of bismuth-germanate (BGO) scintillation detectors of 3 cm thickness (type Crismatec Scintiflex<sup>3</sup>). The detector specifications are given in Table. A.1 of Appendix A.

By measuring the scattered photons from the  $^{11}\text{B}$  sample, the  $\gamma$ -fluence at the photon scattering site is determined experimentally with the formula:

$$\Phi_{\gamma}(E_{\gamma}) = \frac{N_{\gamma}^{\text{corr}}(E_{\gamma})}{\varepsilon(E_{\gamma}, \theta) \cdot N_{\text{tar}} \cdot I_s \cdot W(\theta)} \quad (3.6)$$

<sup>3</sup><http://www.detectors.saint-gobain.com>

$N_{\gamma}^{\text{corr}}(E_{\gamma})$ ,  $\varepsilon(E_{\gamma})$  and  $N_{\text{tar}}$  represent the dead-time and pile-up corrected full-energy peak counts of the resonant transition, the absolute efficiency of the detector at the energy  $E_{\gamma}$ , and the number of target atoms in the  $^{11}\text{B}$  sample.  $W(\theta)$  is the angular correlation between the incoming and scattered photon and  $I_s$  denotes the integrated scattering cross section (see Appendix C).

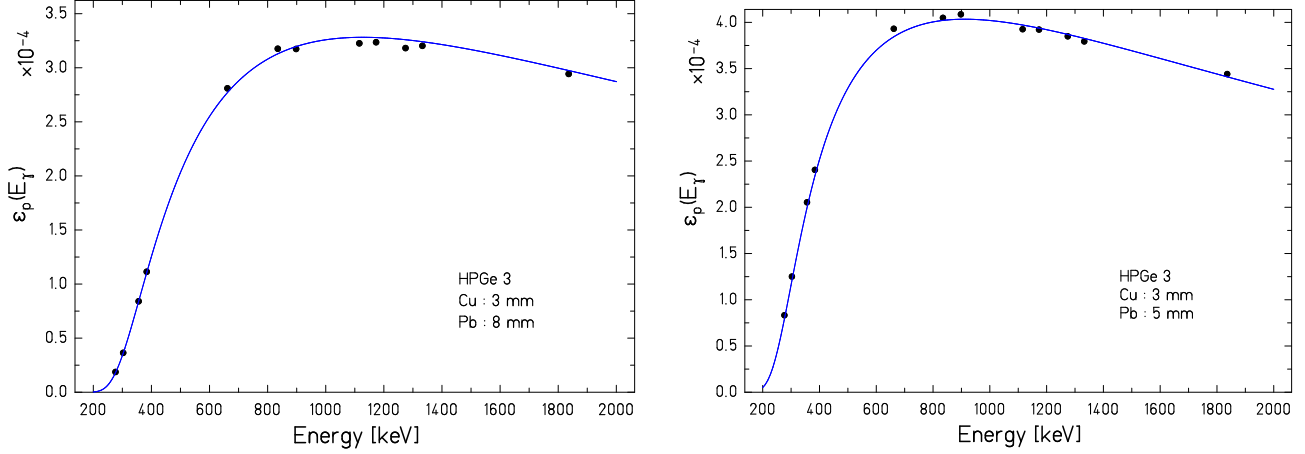


Figure 3.5: Full energy detection efficiency curve of a 100% HPGe detector used at the photon scattering site with the absorber combination Pb - 8 mm, Cu - 3 mm (left) and Pb - 5 mm, Cu - 3 mm (right panel). The curve shows a realistic simulation using GEANT3 which has been normalized to fit the efficiency data (circles) determined using calibration sources. The error bars shown are statistical errors (see text), they are smaller than the symbol size.

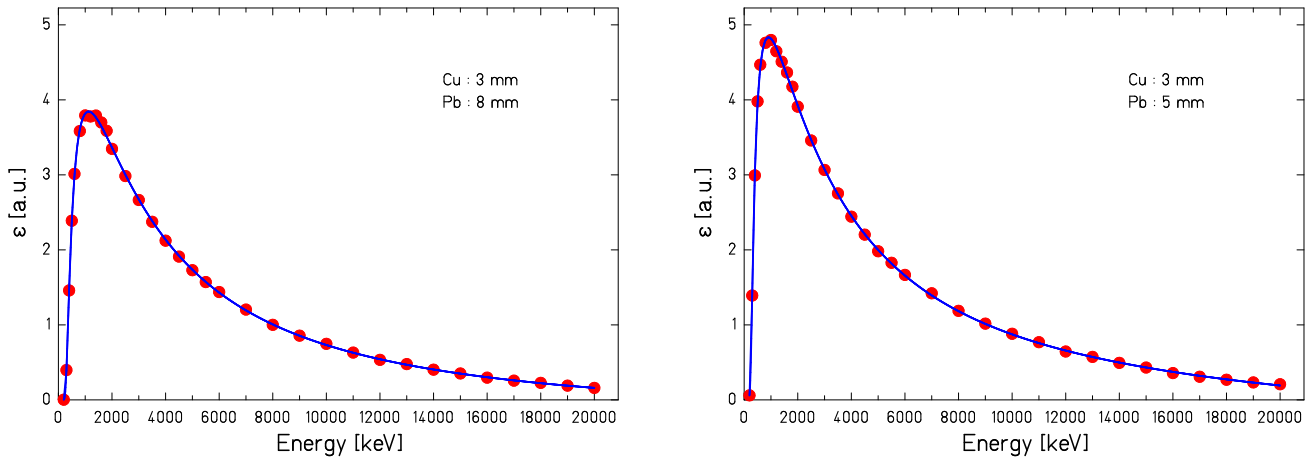


Figure 3.6: GEANT3 simulations for photopeak efficiency of a 100% HPGe detector with a) the absorber combination Pb - 8 mm, Cu - 3 mm and b) Pb - 5 mm, Cu - 3 mm. The fit is a linear combination of several exponential terms, created using the formalism given in [Radf95].

The full-energy peak efficiency of the HPGe detectors has been determined with calibration sources for energies up to 2 MeV. The efficiency determination procedure is given in Table. B.1 of Appendix B along with the properties of the standard sources used for calibration. The



efficiency curve for one of the detectors (at  $127^\circ$ ) is shown in Fig. 3.5 for two different sets of Pb and Cu absorbers. The efficiency curve for the other three detectors look very similar.

For extrapolating the efficiency to higher energies, a GEANT3<sup>4</sup> simulation under realistic geometry was used. The simulations for different absorber combinations are shown in Fig. 3.6. For the interpolation of the simulated efficiency points, a fit is generated using the Radware package [Radf95]. The simulations were normalized to the measured efficiency at energies below 2 MeV (see also: Fig.4, Ref. [Ruse08]).

The decay properties of  $\gamma$ -transitions in  $^{11}\text{B}$  were adopted from the online library of Evaluated Nuclear Structure Data Files (ENSDF) which refers to the revised Ajzenberg-Selove compilation (see Table 11.4, Ref. [Ajze90]). The decay scheme of  $^{11}\text{B}$  is shown in Fig. 3.7. The level energies, level widths, etc., are given in Appendix C.

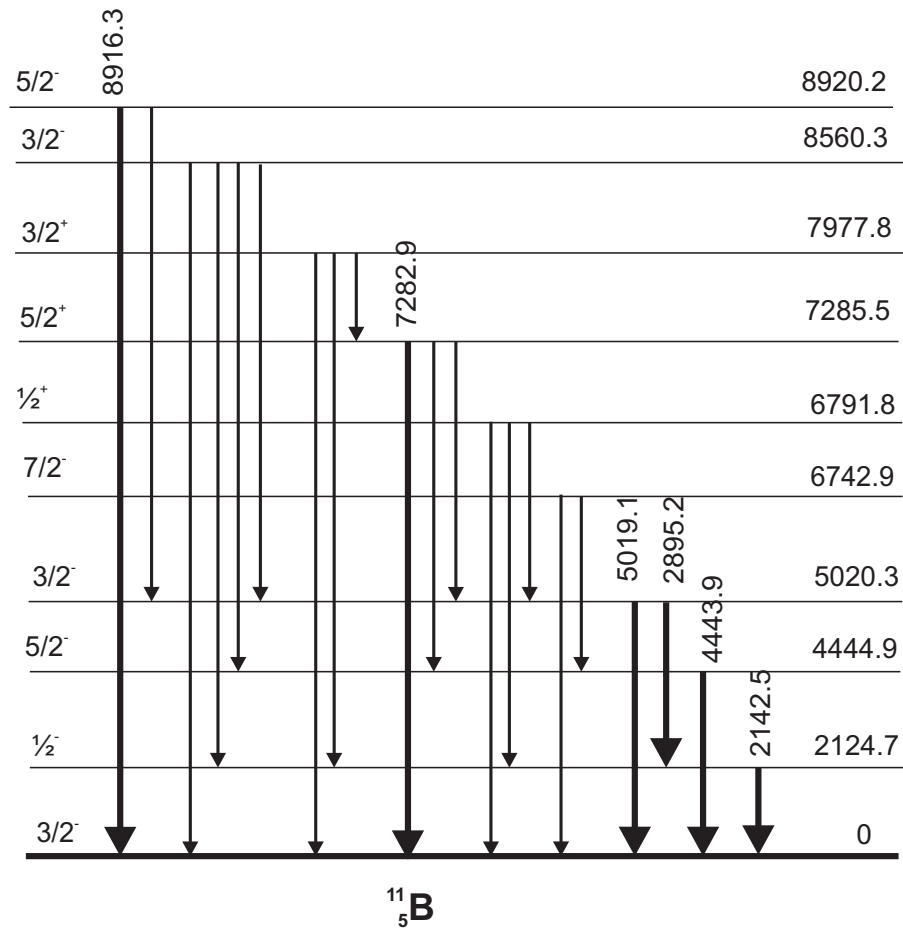


Figure 3.7: The level energies and prominent  $\gamma$ -transitions from  $^{11}\text{B}$ , scheme not to scale. The spin and parity of the states are also shown. The values are adopted from the online library of Evaluated Nuclear Structure Data Files [ENSDF].

The  $^{11}\text{B}$  targets used were of crystalline boron powder with an enrichment of 99.5%, mass areal density of  $1.43 \text{ g cm}^{-2}$  and an effective density of  $1.6 \text{ g cm}^{-3}$ . Energy dependent nuclear self absorption corrections were applied using the formalism given in Ref. [Skor75]. For example, for the level at 7.286 MeV, the nuclear self absorption correction amounts to about 7.5% when using a target with the specifications given above. The correction factor  $C_{nsac}$  for all the

<sup>4</sup>CERN program Library Long Writeup W5013, CERN, Geneva (CH), 1993.

relevant transitions is given in Table C.1 of Appendix C. A sample spectrum originating from the  $^{11}\text{B}(\gamma, \gamma')$  reaction is shown in Fig. 3.8. The prominent  $\gamma$ -transitions from  $^{11}\text{B}$  are marked.

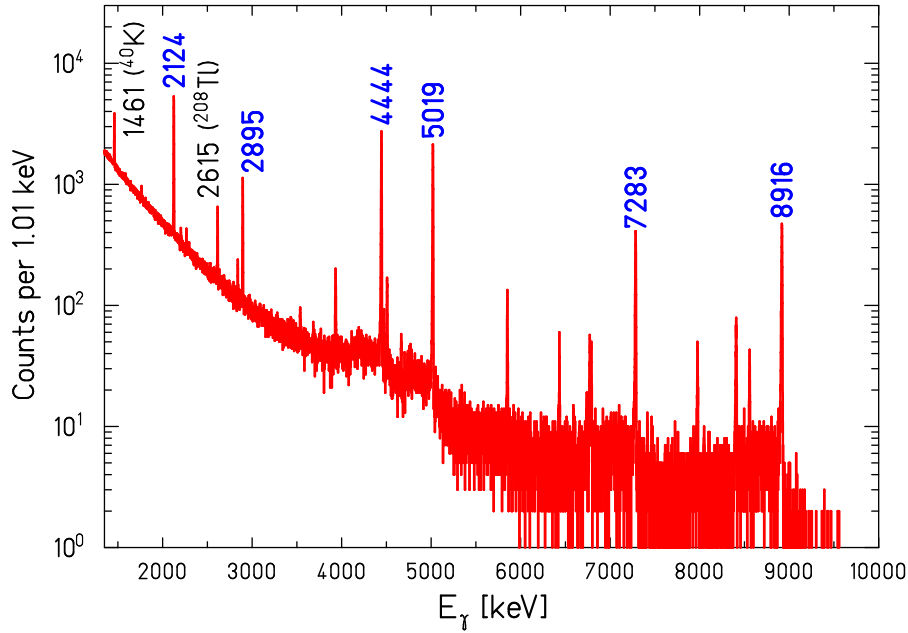


Figure 3.8: Spectrum of  $^{11}\text{B}$  taken with a HPGe detector of 100% relative efficiency. The prominent  $\gamma$ -transitions from  $^{11}\text{B}$  are marked together with the corresponding transition energies. The background peaks stemming from the decay of  $^{40}\text{K}$  and  $^{208}\text{Tl}$  are also shown.

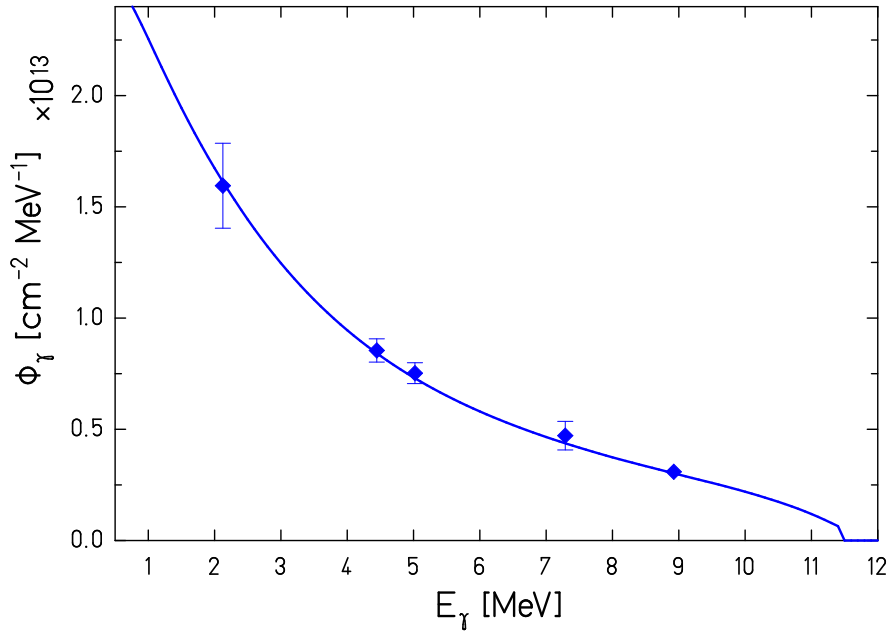


Figure 3.9: Absolute photon fluence measured from the scattered photons in  $^{11}\text{B}$  compared to the Seltzer and Berger bremsstrahlung spectrum with hardener corrections. The fluence measured with different transitions in  $^{11}\text{B}$  agrees to the simulated curve within the error bars.

The experimental photon fluence determined from the  $^{11}\text{B}(\gamma, \gamma')$  reaction is shown in Fig. 3.9. The simulated bremsstrahlung spectrum was created using MCNP<sup>5</sup> which takes into account the effects of the aluminium hardener situated behind the niobium radiator. In MCNP, the bremsstrahlung cross sections from Seltzer and Berger are used. The simulated bremsstrahlung spectrum has been normalized to the measured absolute photon fluence at the transition energies of  $^{11}\text{B}$ . The systematic deviations between the simulated curve and the experimental points are about 6%.

In the fluence determination procedure discussed above, the statistical contribution to the uncertainties from the gamma-counting is quite small and is in the order of 0.5-2%. The systematic uncertainty in the extrapolation of efficiency is estimated to be about 5% in the energy range of the observed transitions in  $^{11}\text{B}$ .

### 3.4.3 Thick target Bremsstrahlung at the photoactivation site

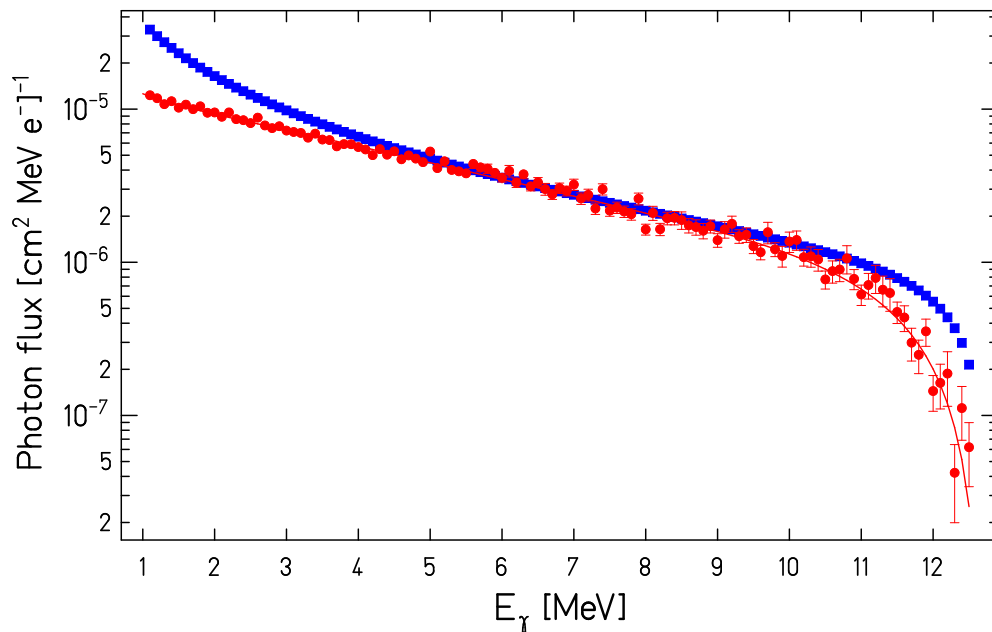


Figure 3.10: *Thick* target bremsstrahlung spectrum at the photoactivation site behind the graphite beam dump as calculated with MCNP4C2 (red circles) for an end-point energy of 12.6 MeV. Theoretical thin-target bremsstrahlung spectrum calculated according to Schiff formula [Schi51] is given for a comparison (blue squares). It is normalized to the MCNP simulation at 6 MeV. The full line is a parametrization of the MCNP simulation.

At the photoactivation site, the bremsstrahlung distribution generated by the graphite is described by MCNP4C2 simulations which are based on the bremsstrahlung cross sections by Seltzer and Berger [Selt86]. The simulated bremsstrahlung distribution for an electron end-point energy of 12.6 MeV is given in Fig. 3.10. The thin target bremsstrahlung distribution for the same endpoint energy using the Schiff formula [Schi51] is given for comparison.

From Fig. 3.10, one can see how the shape of a thick target spectrum is changed due to creation of photon- electron cascades and multiple scattering. The thick target spectral shape

<sup>5</sup>MCNP - Monte Carlo N-Particle Transport Code, <http://mcnp-green.lanl.gov/>

is required to determine the absolute photon flux for the Mo/Sm samples that were irradiated at the photo-activation site with the bremsstrahlung produced in the graphite block.

For the range of bremsstrahlung energies under discussion, the photon flux at the photoactivation site is, on average, about a factor of 100 times higher than the flux at the photon scattering site. For example, for a bremsstrahlung endpoint energy of 15.0 MeV and an irradiation time of about 20 hours, the available photon flux at the photoactivation site at  $E_\gamma^X = 7.288$  MeV amounts to about  $6 \times 10^9 \text{ cm}^{-2} \text{ s}^{-1} \text{ MeV}^{-1}$  whereas the flux at the photon scattering site, measured by  $^{11}\text{B}$  scattering amounts to about  $7 \times 10^7 \text{ cm}^{-2} \text{ s}^{-1} \text{ MeV}^{-1}$ . As discussed in Sect. 3.2, the absolute activation yield  $Y_{\text{act}}$  is normalized to the photon fluence at  $E_\gamma^X = 7.288$  MeV. The experimental results are always plotted as a function of endpoint energy.

### 3.5 Determination of the electron-beam energy

For the photoactivation experiments, it is important to monitor the electron energy, which defines the maximum energy of the bremsstrahlung spectrum. The beam energy is measured using two different methods - one is the conventional method by the use of a Nuclear Magnetic Resonance (NMR) probe to determine the magnetic rigidity of the beam and the other is by studying the photodisintegration of the deuteron.

#### 3.5.1 The NMR method

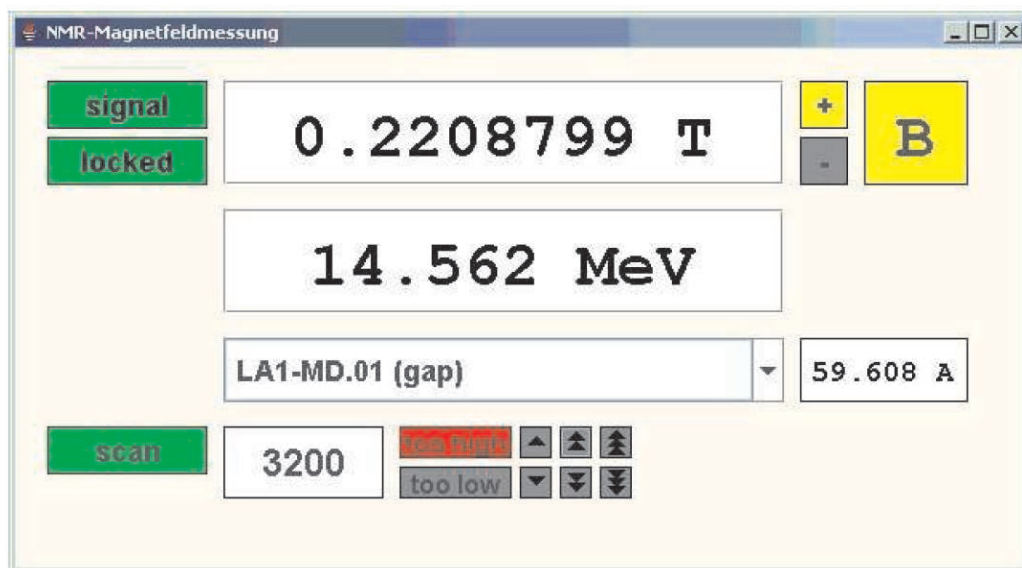


Figure 3.11: User interface to the teslameter used in NMR measurements at ELBE (from [Lehn06]). The instrument status indicates the presence of and the correct lock on to a NMR resonance. The beam energy, value of the magnetic field etc are displayed in separate tabs.

At ELBE, the deflection of the beam in a magnetic field is used for the beam energy determination. This requires a precise knowledge of the magnetic field strength.

To measure the field, we use an NMR (Nuclear Magnetic Resonance) probe [Lehn06]. The probe containing a sample material which has a nuclear angular momentum (spin) is placed inside the magnetic field. The angular momentum in turn rotates about the axis of the field.

The frequency of precession depends on the value of the angular momentum and the field. Around the sample, a modulation coil is wound which is driven by an RF signal. If the sample atoms are influenced by the RF field of frequency close to the precession frequency, the phases will be synchronized. Then a signal is measured in a second pickup coil wound perpendicular to the modulation coil. The accurate determination of the resonance frequency in turn yields an accurate magnetic field measurement.

To generate and measure the required RF frequencies, a commercial teslameter is used. It is remote-controlled in the diagnostic station at the ELBE control room. A snapshot of the user interface of the teslameter is shown in Fig. 3.11. When a valid magnetic field value is received this value is displayed with the computed beam energy in parallel (see Fig. 3.11). However, the insufficient knowledge of the field mapping of the used magnet necessitates a more precise method for the beam energy measurement. A calibrated energy spectrometer will be installed in future in this regard.

### 3.5.2 Photodisintegration of the deuteron

Independent from the NMR measurement, the electron beam energy is monitored at the photon scattering site via the photodisintegration of the deuteron. The endpoint energy of the bremsstrahlung distribution is determined by measuring protons from the photodisintegration of the deuteron (see Fig. 3.2, deuteron breakup target) with silicon detectors. From the maximum energy of the emitted protons, the maximum energy of the incident photons can be deduced.

When a photon with sufficient energy is incident upon a deuteron, the bond between the proton and neutron can be broken, emitting them in opposite directions. Using four-momentum conservation, the energy of the incident photon can be calculated.

Consider the simple example of a photon  $k$  incident upon a stationary deuteron  $d$  which results in the disintegration of the deuteron into a proton and a neutron. The neutron is emitted with a momentum at an angle from the direction of the incident photon. The incident photon energy is related to the proton energy and the angle of emission by the equation

$$E_\gamma = k_0 = \frac{m_n^2 - m_p^2 - m_d^2 + m_d(T_p + m_p)}{2(m_d - m_p - T_p + \sqrt{T_p^2 + 2T_p m_p} \cos \theta_p)}. \quad (3.7)$$

where  $m_p$ ,  $m_n$  and  $m_d$  are the masses of the proton, neutron and deuteron respectively.  $T_p$  is the proton kinetic energy and  $\theta_p$  is the proton angle of emission. The details of the photodisintegration kinematics can be found in Appendix A of [Mori06].

At the photon scattering site, the protons are detected by a set-up of four silicon detectors (Ion-Implanted-Silicon Charged-Particle Detectors, type ORTEC ULTRA<sup>6</sup>) placed at a distance of 6 cm from the beam axis and at azimuthal angles of 0°, 90°, 180° and 270° with respect to the photon beam. The detectors have a thickness of 500  $\mu\text{m}$  and a sensitive area of 600  $\text{mm}^2$ . The detector characteristics are given Table. A.3 of Appendix A.

For the energy calibration of the silicon detectors, a mixed alpha source  $^{239}\text{Pu}/^{241}\text{Am}/^{244}\text{Cm}$  is used. A sample spectrum is shown in Fig. 3.12. The alpha energies used for calibration are marked. In addition, equidistant lines from a pulse generator were used to determine the offset. For measuring the photodisintegration of the deuteron, a 4  $\text{mg}/\text{cm}^2$  thick polyethylene film<sup>7</sup>, in which hydrogen is substituted by deuterium ( $\text{CD}_2$ ) is used as the target. The  $\text{CD}_2$  target is

<sup>6</sup>ORTEC, 801 South Illinois Avenue, Oak Ridge, TN 37830, USA.

<sup>7</sup>Courtesy : D. K. Geiger, SUNY Geneseo, NY 14454, USA.

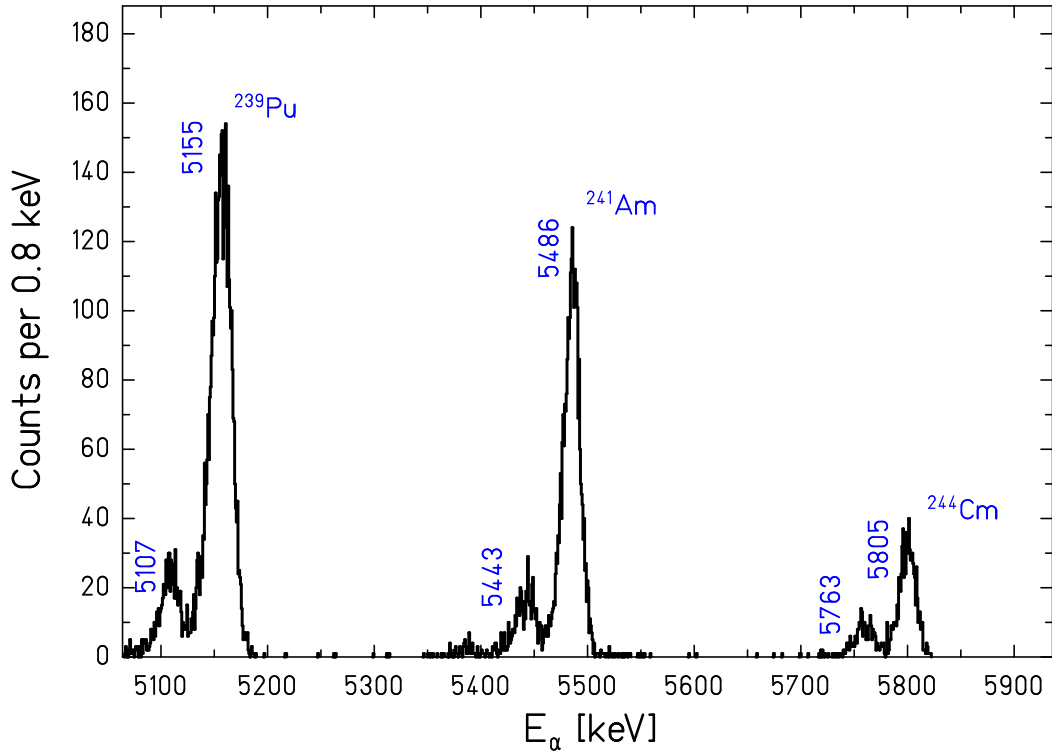


Figure 3.12: Spectrum of a mixed  $^{239}\text{Pu}/^{241}\text{Am}/^{244}\text{Cm}$  alpha source used for calibrating the Si-detectors for endpoint energy determination.

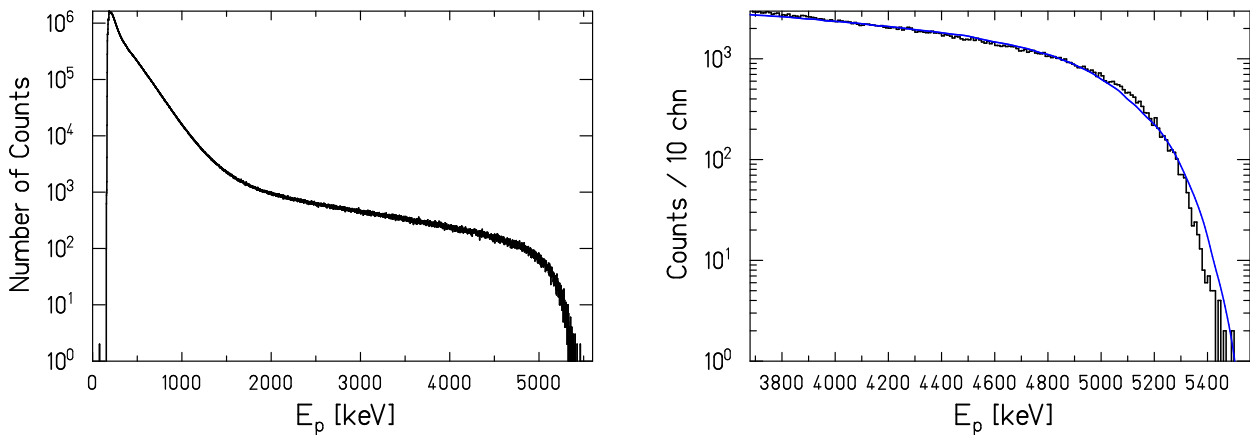


Figure 3.13: On the left panel, proton spectrum from the photodisintegration of deuterons recorded with Si detectors of  $500\ \mu\text{m}$  thickness during an irradiation with incident electron energy  $13.2\ \text{MeV}$  is shown. A fit to the rebinned spectrum shown in the left panel is on right panel. The fit is a simulated spectrum under realistic geometry which also takes into account of the energy loss in the  $\text{CD}_2$  target, see text.

positioned parallel to the incident beam such that its surfaces are observed by all four detectors under  $45^\circ$ . A typical spectrum is shown in Fig. 3.13. The low-energy part of the spectrum below  $2.5\ \text{MeV}$  reveals not useful as it is dominated by beam induced  $\gamma$ -rays and electrons. For a very precise measurement of the proton endpoint energy, it is necessary to correct for the

energy-losses in the  $\text{CD}_2$  target, in the detector dead layers and for the non-electronic losses in the intrinsic area of the detector. The correction procedure for all these effects has been discussed in detail by [Erha09].

In order to determine the endpoint energy, the measured spectra are fitted to a simulated proton spectrum for a realistic geometry. The simulation takes into account the deuteron breakup kinematics, geometry of the detector setup, energy loss of the protons inside the  $\text{CD}_2$  film as well as the energy spread of the electron beam. A fit to the measured spectrum is shown (see Fig. 3.13, right panel).

The statistical error from the fit amounts to 2-8 keV for the range of endpoint energies described here. The systematic deviation of the experimental spectra from the simulated one is 40 keV. This is inherent to all experiments but significant only for endpoint energies close-above the neutron/proton-emission threshold of the photodisintegration reaction under consideration (see Fig. 5.20, Sect. 5.7). This method has been used for electron-beam energy measurements for all the experiments discussed in this thesis. The measurement has been found to be reliable and accurate.

### 3.5.3 Monitoring of the electron beam stability

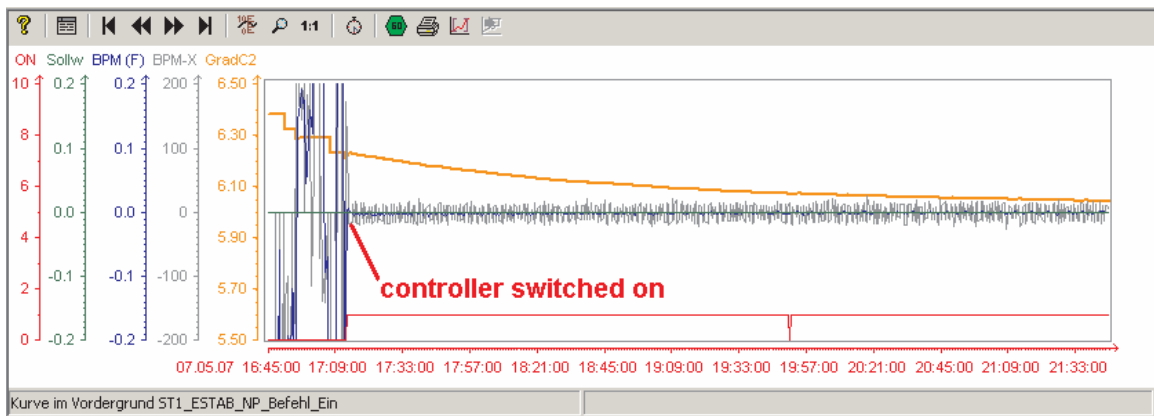


Figure 3.14: The operation of the beam energy control loop in the nuclear physics beam line over a period of 5 hours at the nominal energy 14.5 MeV, gradient  $GC_1 = 10$  MV/m and beam current  $I_{Beam} = 450\mu\text{A}$  in continuous wave mode (adopted from [Just07]). The color codes stand for - ON: controller on state, Sollw: BPM reference value, BPM(F): BPM reading filtered with 30 sec, BPM-X: BPM reading and GRADC2: gradient set value for cavity 2 (controller output).

One of the key requirements of the photoactivation experiments is the stability of the mean electron beam energy and the beam intensity. A slow drift of the effective accelerating field during the first hours after a machine power-up or after switching to different nominal beam energies is practically observed. Since the energy drifts affect parameters of the generated bremsstrahlung spectra, this needs to be corrected. To correct for the energy drift continuously, a non-intrusive Beam Position Monitor (BPM) is placed in a transversely dispersive part of the beam guide. The energy control loop using a BPM acts as a sensor. The description of the beam line setup and the simplified dynamic model of the control loop is given in [Just07].

The operation of the control loop in the nuclear physics beam line over a period of 5 hours is shown in Fig. 3.14. The fluctuations seen in the first 30 minutes of the plot are from the manual setting-up of the machine. From the moment of switching on, the BPM reading stays

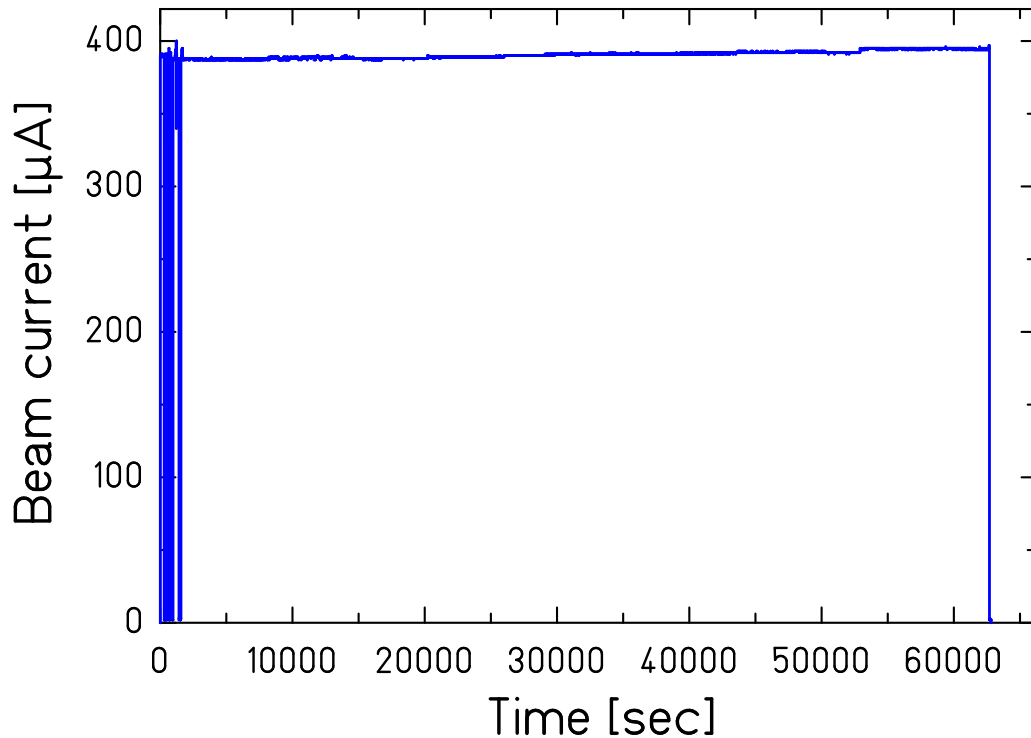


Figure 3.15: The beam current (bpm11i) recorded during an experiment with an electron beam energy of 13.0 MeV. The beam current is found to be stable for the whole irradiation period ( $\approx 18$  hours). The fluctuations in the first few minutes denote the beam tuning period by the accelerator operators.

on a constant base line (see figure, curve BPM-X). This method is working properly for all experiments requiring higher mean energy stability. The controller optimization techniques are given in [Just07]. Even though the performance of the current control loop is fitting our needs, there will be improvements in the future like combining the present loop with a high resolution field measurement for an absolute energy measurement.

As stated earlier, the electron beam for bremsstrahlung experiments is deflected from the main line by a non-dispersive system of two dipole magnets with a quadrupole magnet in between. There is another subsequent quadrupole doublet which focusses the electron beam on to the radiator. There are two beam position monitors placed along the beam line. These are denoted as BPM11 and BPM06. BPM11 is located behind the first dipole and BPM06 is after the second quadrupole doublet (before the radiator). The beam current entering to the beam line for bremsstrahlung experiments as recorded by BPM11 (bpm11i) during an experiment with an electron beam energy of 13.0 MeV is shown in Fig. 3.15. For the whole irradiation period ( $\approx 18$  hours), the beam current was recorded periodically and is found to be practically stable. The fluctuations in the first few minutes denote the beam tuning period by the accelerator operators. The small fluctuations in the beam current generally doesn't affect the experiment, except for activation measurements of the nuclei with short half-lives.



# Chapter 4

## Decay studies of the activated targets

For the reaction-yield determination explained in Eq. 3.2, the activated targets were studied by gamma-ray spectroscopy. The first section of this chapter is dedicated to the  $\gamma$ -counting method used for decay studies at ELBE. The different counting facilities used in the scope of the experiments are discussed in detail. The last section deals with the newly built pneumatic delivery system for studying short-lived nuclides.

### 4.1 Determination of peak intensity

In photoactivation experiments, it is extremely important to determine the correct peak area of the  $\gamma$ -transition under investigation. For the analysis of the experiments discussed in this thesis, we used the SATAN<sup>1</sup> (System for the Analysis of Tremendous Amounts of Nuclear data) data analysis package to evaluate experimental data, to perform model calculations, and to visualize the results. This is a user friendly analysis program written in IBM VisualAge PL/I for workstations. SATAN can read data arrays in different simple ASCII as well as binary list-mode formats. It has powerful fit capabilities with least-squares and Poisson fits and automatic peak finding in one and two dimensions.

For analyzing the  $\gamma$ -spectra, we modified the built-in fit routines of SATAN by including the additional measurement-specific requirements. The peakfit analysis and the determination of dead time and pile-up correction factors are discussed in the following sections.

#### 4.1.1 Peakfit functions for $\gamma$ -ray spectra

While analyzing  $\gamma$ -ray peaks from the spectra, precision is generally limited by the ability to define and compute consistent peak areas [Debe01]. Simple methods with Gaussian functions are adequate for single, well-resolved peaks. But for a complex peak shape with considerable spectral background and low-energy tailing, an adapted fit routine is necessary.

For the experiments discussed in this thesis, the extraction of relevant peak parameters from the measured spectrum is done with a fit routine similar to the one in the Radware package [Radf95]. Each peak is considered to be composed of three components:

1. a Gaussian

$$y_g = \frac{h \cdot R}{100} \exp\left(-\frac{(E - E_0)^2}{2\sigma^2}\right)$$

---

<sup>1</sup><http://www-wnt.gsi.de/CHARMS/SATAN/graf.htm>

2. a skewed Gaussian,

$$y_s = h \cdot \left(1 - \frac{R}{100}\right) \exp\left(\frac{E - E_0}{\beta}\right) \operatorname{erfc}\left(\frac{E - E_0}{\sqrt{2}\sigma} + \frac{\sigma}{\sqrt{2}\beta}\right)$$

3. and a smoothed step function to increase the background on the low-energy side of the peak.

$$y_b = \frac{h \cdot S}{100} \operatorname{erfc}\left(\frac{E - E_0}{\sqrt{2}\sigma}\right) + A + B(E - E_0)$$

Components (2) and/or (3) can easily be set to zero if not required.

The first component is the Gaussian, usually the main component of the peak which arises from complete charge collection of a photoelectric event in the detector.  $E$  is the energy variable,  $E_0$  and  $\sigma$  are the centroid and standard deviation of the Gaussian.  $h$  stands for the height of the total peak,  $S$  for the step height of the background in percent of peak height and  $R$  is the fraction of Gaussian peak in percent, i.e.,  $R=100$  denotes a full Gaussian with no skewed component.

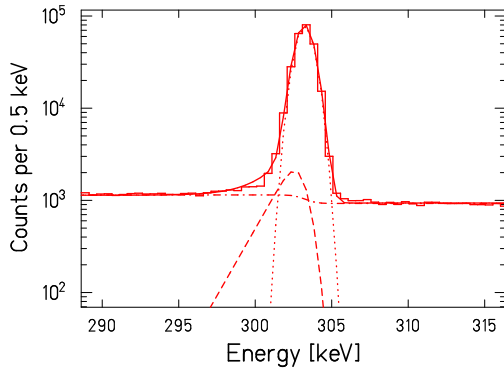


Figure 4.1: Peak fit for one of the strongest decay lines of  $^{133}\text{Ba}$  - Fit parameters chosen for display are  $R = 97.3$ ,  $\beta = 3.8$  keV and step  $S = 0.24$ . The fit components are shown separately and correspond to: dotted line - gaussian, dashed line - skewed gaussian, dash-dotted line - step, and full line represents how all the components go together to make the total peak fit.

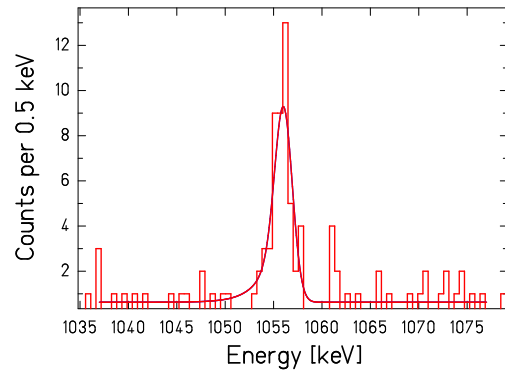


Figure 4.2: Peak fit for the  $\gamma$ -transition from the decay of  $^{143}\text{Sm}$  following the  $^{144}\text{Sm}(\gamma, n)$  reaction. Close to the threshold, the  $\gamma$ -counting statistics is very low. For the peak-fit shown, the parameters are:  $R = 73.8$ ,  $\beta = 4.9$  keV and step  $S = 0$ . The full line represents the peak fit and corresponds to the peak area  $45 \pm 8$  counts, see text for details.

Component (2) is the skewed Gaussian which arises from incomplete charge collection, often due to *trapping* of charge at dislocations in the crystal lattice caused by impurities or neutron damage. If the detector and electronics had perfect resolution, component (1) would be a delta-function and component (2) would yield an exponential tail on the low-energy side. Convolution of this exponential tail with a Gaussian resolution function yields the functional form  $y_s$  with  $\operatorname{erfc}$  as the complement of the error function and  $\beta$  as the decay constant of the exponential.  $\beta$  now corresponds to the *skewedness* of the skewed Gaussian.

The third component arises mainly from the Compton scattering of photons and the escape of photoelectrons from the Ge crystal, which result in a slightly higher background on the low-energy side of the peak. The functional form  $y_b$  is produced by the convolution of a step

function with a Gaussian of width  $\sigma$ . A and B denote the constant and linear background. The different constant background below and above the full efficiency peak stems from multiple interactions (multi-compton scattering, cf.) of one  $\gamma$ -ray inside the crystal where the full energy is not deposited.

Fig. 4.1 illustrates how the components go together to make up the total peak shape. The peak fit is illustrated for an energy calibrated spectrum showing one of the strongest transitions in the decay of  $^{133}\text{Ba}$ . The different components such as gaussian, skewed gaussian, step etc are shown separately.

For  $\gamma$ -peaks with very low counting statistics, the same peak fit routine discussed above was used. In such a case, the width of the peak is taken from a good statistics peak at the same energy. This width is then kept fixed for the low-statistics peak and a poisson-fit including zeroes is performed. For the peak fit shown in Fig. 4.2, the width was kept fixed as 2.3 keV and the different parameters chosen were:  $R = 73.8$ ,  $\beta = 4.9$  keV and step  $S = 0$ . The resulting area was 45 counts with a statistical uncertainty of 17%.

### 4.1.2 The dead time and pile-up correction factors

In all the  $\gamma$ -counting applications discussed in this thesis, it was important to correct for the loss of events due to the dead time of the system. This refers to the minimum separation time between two registered events. The dead time losses are rather severe in high count-rate measurements. In such cases, accurate correction factors must be included for these losses while analyzing the  $\gamma$  spectra. In addition to this, one has to correct also for the so-called pile-up problems which arise due to the interfering of random pulses. This is a pure effect of the electronics associated with the summing of two pulses which come in a short time interval.

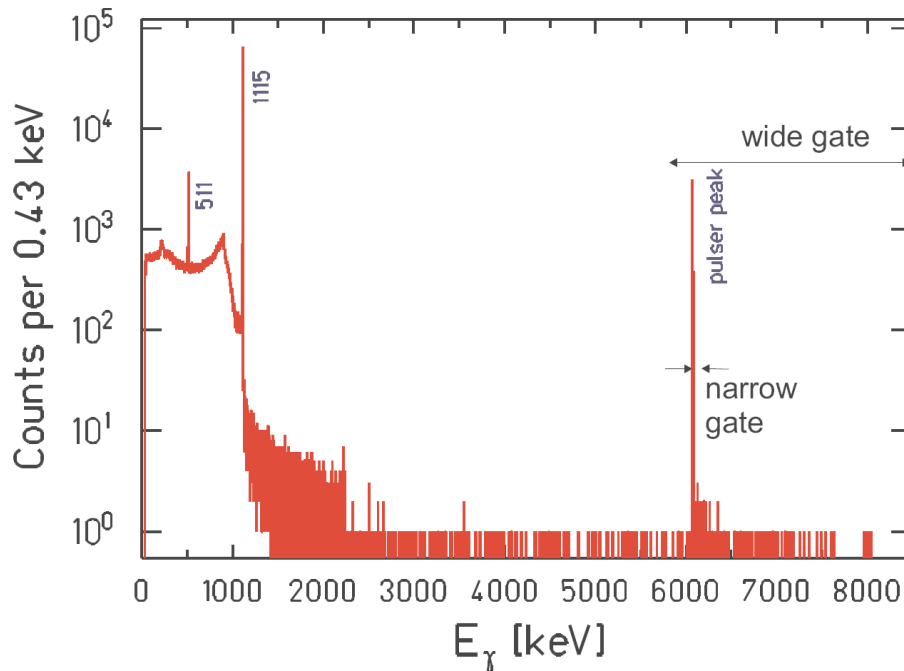


Figure 4.3:  $\gamma$ -ray spectrum of a  $^{65}\text{Zn}$  source with pulser peak. The pulser peak area is determined from the narrow gate and the wide gate includes the part as shown in figure. The prominent  $\gamma$ -transitions from  $^{65}\text{Zn}$  decay are marked with their energies shown in keV.

The dead time and pile-up correction was achieved by the pulser method in which a pulser signal is fed to the “test” input of the detector. The procedure can be explained by considering a sample spectrum of a  $^{65}\text{Zn}$  source with pulser shown in Fig. 4.3. The superposition of the pulser signal and the signal from the detector gives a signal at energy higher than the amplitude of the pulser. The peak area of the pulser is defined by the *narrow gate* and the *wide gate* defines the area including the pulser peak and pile-up of  $\gamma$ -ray signals and pulser signals as shown in Fig. 4.3. The pulser counts are counted in a scaler as well (see Fig. 4.4).

The dead time correction factor is given by

$$C_{dt} = \frac{N_{\text{widegate}}}{N_{\text{scaler}}} \quad (4.1)$$

Where  $N_{\text{scaler}}$  is the number of counts recorded in the scaler and  $N_{\text{widegate}}$  is the area of the defined wide gate.

The pile-up correction factor is

$$C_{pup} = \frac{N_{\text{narrowgate}}}{N_{\text{widegate}}} \quad (4.2)$$

with  $N_{\text{narrowgate}}$  as the area of the pulser peak.

For the example shown in Fig. 4.3,  $C_{dt}$  is 0.994 and  $C_{pup} = 0.979$ . The number of counts in the peak corrected for the dead time and pile-up corrections is given by

$$N_{\gamma}^{\text{corr}} = \frac{N_{\gamma}}{C_{dt} \cdot C_{pup}} \quad (4.3)$$

The corrected peak area is an important input for determining the number of radioactive nuclei using Eq. (3.2). All the experiments included in this thesis were performed with accurate dead time and pile-up corrections using this method.

## 4.2 Counting facilities

### 4.2.1 The low-level counting setup

At ELBE, the decay spectroscopy of activated targets is studied offline by using HPGe in a *low-level counting setup* located outside the nuclear physics cave. The two detectors used are of relative efficiency 90% and 60% relative to a 3”×3” NaI detector. The detectors are placed in so-called *lead castles* which are used to screen the detector from background radiation [Erha04]. A schematic sketch of the counting setup and the lead castle is given in Fig. 4.4. The inner layer (2 cm) of the lead castle is lined with lead of low level radioactivity. The rest is covered with lead which contains traces of the radioactive  $^{210}\text{Pb}$  from the uranium/thorium decay chains. A graded-Z shield is used which helps to reduce the Pb K X-rays at 80 keV. Very pure, electrolytic copper is used for this purpose which emits lower-energy Cu K X-rays at 3 keV. Only for X-ray measurements it is necessary to shield the Cu K X-rays with Plexiglas. A natural background spectrum recorded with the 90% HPGe inside the lead castle is shown in Fig. 4.5.

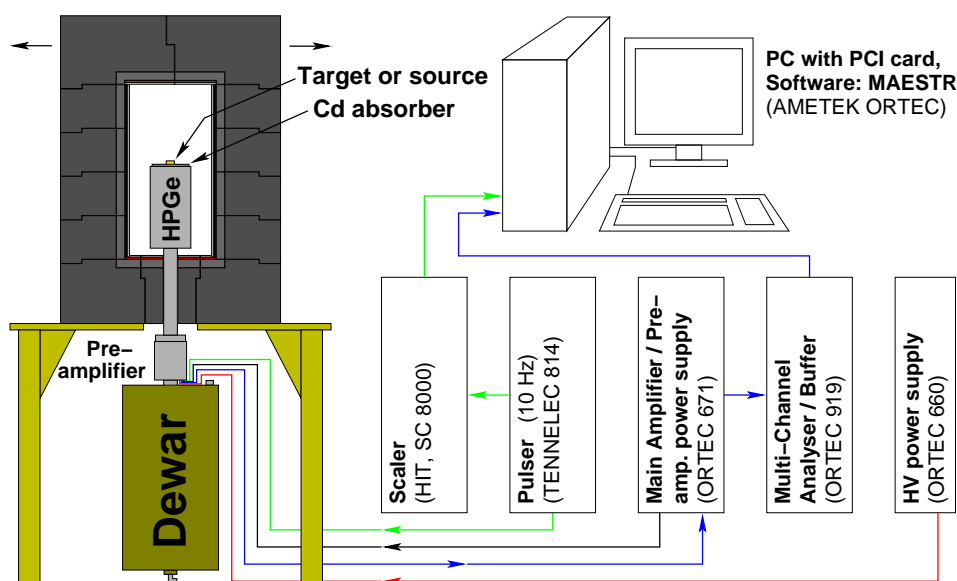


Figure 4.4: Sketch of the low-level counting setup showing the lead castle, HPGe detector and counting system.

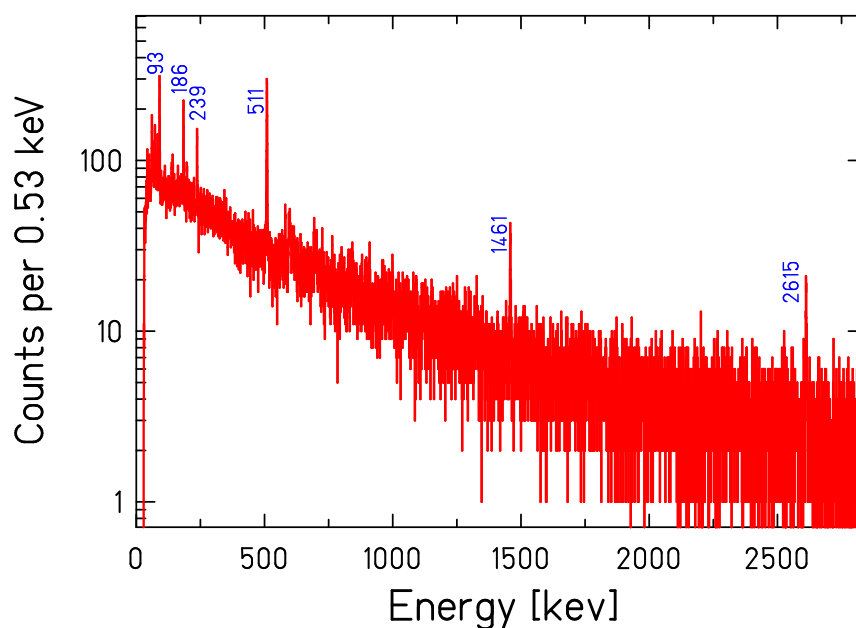


Figure 4.5: Natural background measured with the 90% HPGe detector in low-level counting setup. The spectrum was recorded for a period of one day. The peaks stemming from the decay chains of Pb, Ra and Th are marked. The transition at 1461 keV from the decay of  $^{40}\text{K}$  is also shown.

On the top of the detector crystal, we have put three layers of Cadmium absorber with an overall thickness of 1.535 mm (cf. Fig. 4.6) to block the coincidence summing, especially of X-ray summing with the gamma-rays [Nair04]. To maximize the absolute efficiency of the detector, the source/target is put on top of the Cd absorber which is situated directly on

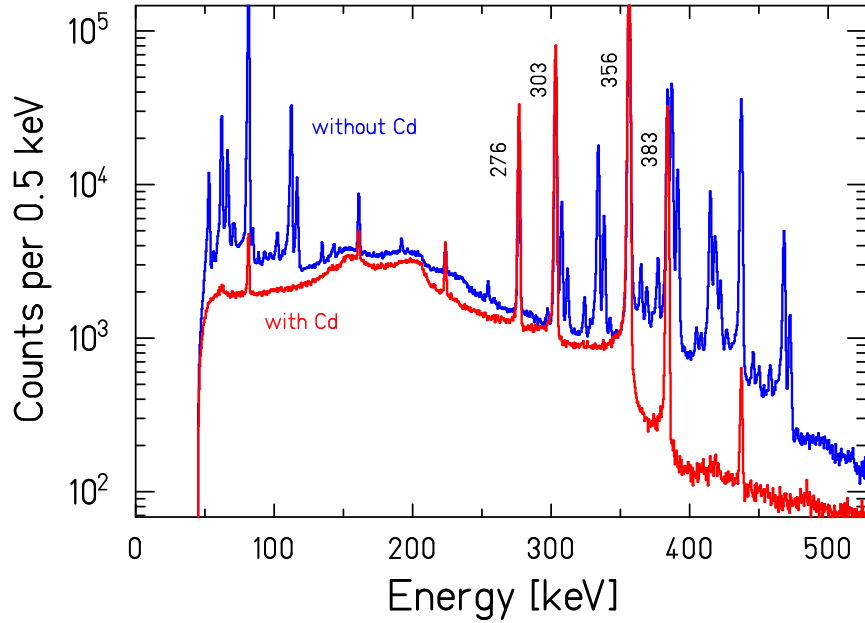


Figure 4.6: HPGe spectra of  $^{133}\text{Ba}$  - upper blue histogram is without absorber and lower red one is with a 1.535 mm thick Cd absorber. The strongest  $\gamma$ -transitions from the  $^{133}\text{Ba}$  decay are marked. It is clearly seen that the summing events are considerably reduced with the insertion of the Cd absorber.

the HPGe capsule. The preamplifier output signals are amplified by a spectroscopic amplifier (ORTEC 671) and then processed by a multi-channel analyzer (ORTEC 919). The dead time and pileup corrections were done by applying a 10 Hz pulser signal to the preamplifier test input (see Sect 4.1.2).

For recording/managing the decay spectra, the software MAESTRO-32 from ORTEC is used. It is an advanced, easy-to-use MCA Emulator which fits precisely for our purposes. Some of its features include multi-detector interface, automation of acquisitions with *job streaming*, complete interactive control of all Multi-Channel-Buffer hardware features etc.

For the precise and accurate analysis of the gamma-spectra, the detectors are calibrated with a certified set of sources with the properties listed in Table. B.1 of Appendix B. For a complex decay scheme when more than two photons are emitted in cascade, like the ones with  $^{133}\text{Ba}$ , the effect of absorbers becomes significant (see Fig. 4.6).

The efficiency curves for the detectors with 90% and 60% relative efficiency are shown in Fig. 4.7. For multi-gamma emitting nuclides, coincidence summing corrections have been applied. The efficiency determination procedure and corrections for the "summing-in" or "summing-out" effects are described in detail in Sect. B.2 of Appendix B.

The fit to the efficiency curve is from a GEANT3 simulation with realistic detector geometries. The dependence between simulated and measured efficiencies were in agreement by a constant factor close to unity for the considered energy range. In the estimation of uncertainties, both statistical and systematic errors are taken into account. The systematic uncertainties in the activity as given in the source certificates amount to 0.6-1.5% in the energy range from 0.12 to 1.9 MeV. The statistical error mainly originates from the peakfit for the calculation of peak areas and is typically in the order of 1-2%. The statistical error contribution is very small in the order of 0.2-0.5%.

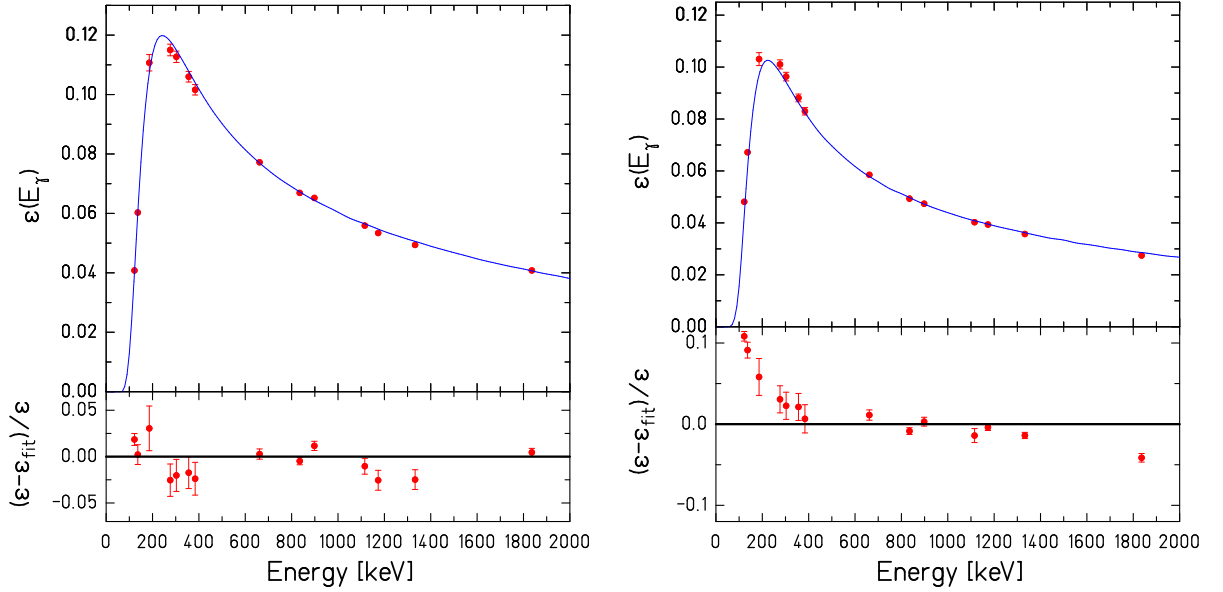


Figure 4.7: Full-energy peak efficiency curve for a HPGe detector with 90% efficiency (left panel) and 60% efficiency (right panel) relative to a 3"×3" NaI detector. The upper part is the fit curve overlaid on experimental data and the lower part shows the residuals with error bars of the data points.

#### 4.2.2 Efficiency variations with source-detector geometry

To test the variation of efficiency with source-detector distance, we measured point sources at various radial distances ( $r$ ) and vertical distances ( $d$ ) on the top of the endcap of the detector. For a point source positioned at various distances  $d$  from the symmetry axis of the detector, the efficiency  $\varepsilon(d)$  is related to the efficiency on the top of the detector endcap  $\varepsilon(d_0)$  as

$$\frac{\varepsilon(d)}{\varepsilon(d_0)} = \frac{\Omega(d)}{\Omega(d_0)} \quad (4.4)$$

with  $\Omega(d)$  as the solid-angle of the detector [Debe01] which depends on the photon energy. This is a valid approximation as long as  $d$  and  $d_0$  are large in comparison with the detector radius. The variation of the point source efficiency for the 90% detector with different radial and vertical distances from the endcap of the detector is shown in Fig. 4.8.

In Fig. 4.9, the point source efficiency variation for the 661 keV  $\gamma$ -transition of  $^{137}\text{Cs}$  source is given for the detector with 60% efficiency. For the efficiency variation with vertical distances  $d$ , the fit curve is created from a solid-angle dependent function for efficiency.

For the variation of point-source efficiency with radial distance  $r$  on the top of the endcap, the shape of the fit curve is described by the relation

$$\varepsilon(r, d) = \varepsilon(0, d) \exp^{-c(d)r^2} \quad (4.5)$$

where the parameter  $c(d)$  depends on the energy and the distance. For the ratio of the point source efficiency at a radial distance  $r$  to the one on the top of the endcap is show in the right panel of Fig. 4.9. From the figure on the left panel, one could see that the point source efficiency reduces by  $\approx 2\%$  when increasing the distance  $d$  on the symmetry axis by 1 mm.

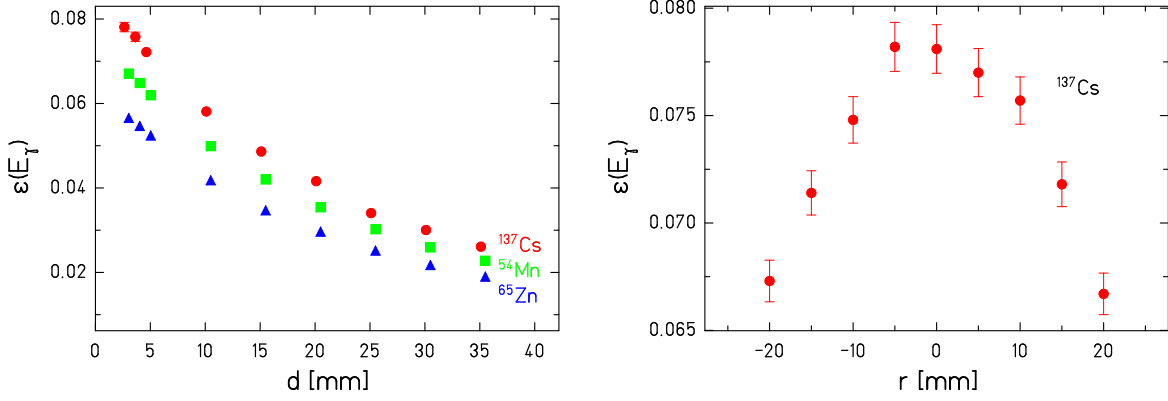


Figure 4.8: The variation of point source efficiency as a function of various distances on the symmetry axis and off-axis of the 90% HPGe detector in the low-level counting setup. The efficiency variation with distance  $d$  was measured for single-line nuclides like  $^{137}\text{Cs}$ ,  $^{54}\text{Mn}$  and  $^{65}\text{Zn}$  (left). The off-axis efficiency variation measured with the  $^{137}\text{Cs}$  source is shown on the right panel.

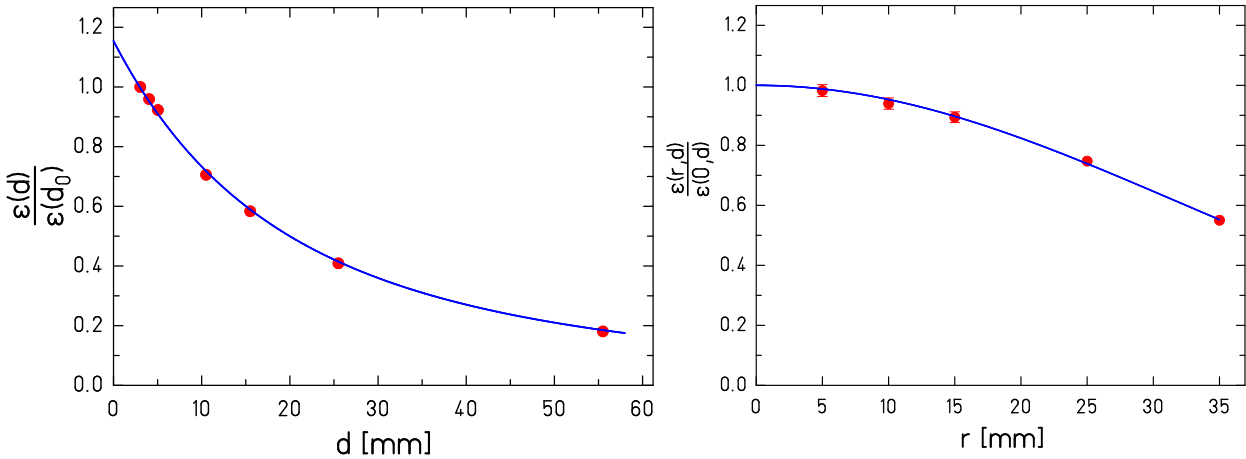


Figure 4.9: The point source efficiency ratio for 661 keV for different distances  $d$  on the symmetry axis of the 60% detector (left). The fit is created from the source-detector solid angle relationship for a point source. The ratio of the point source efficiency with radial off-axis distances  $r$  is shown in the right panel for a distance  $d=0$  mm (directly on endcap). The fit curve in this case is from Eq. 4.5.

### 4.2.3 Decay studies at the underground laboratory 'Felsenkeller'

The radioactive decay of irradiated targets with very low activity was studied at the low-background measurement laboratory "Felsenkeller" in Dresden. The Felsenkeller laboratory is located in the Weisseritz-valley in Dresden which is about 20 kilometers from FZ Dresden-Rossendorf where the samples are irradiated. The rock cover has a thickness of 47 m (110 m water equivalent). At this depth, the cosmic muon flux is reduced by 98% compared to that at the surface and the background rate is reduced by about a factor of 30 at 1 MeV.

The measuring chamber inside the cave is shielded by different layers of steel and lead [Nies98]. A comparison of the background spectra in the laboratories at earth's surface (ELBE) to that at medium depth (Felsenkeller-110 m w.e) and at deep underground (Gran Sasso-3800 m w.e,



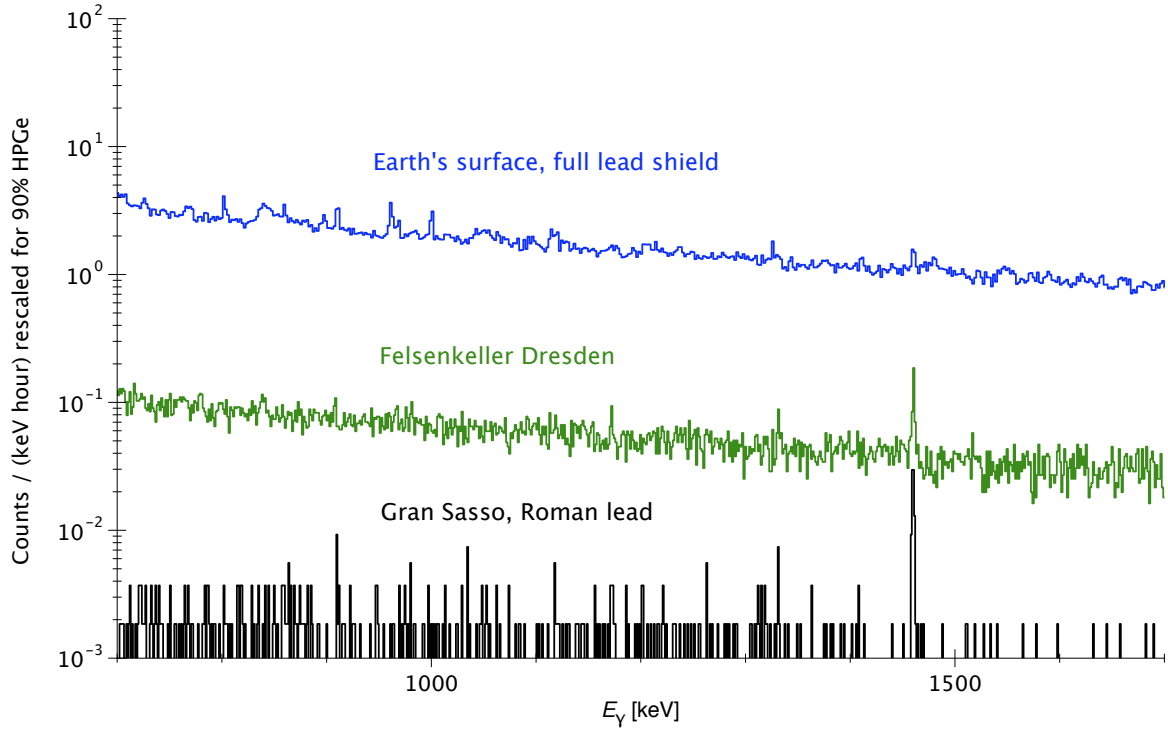


Figure 4.10: Comparison of background spectra from underground laboratories at different depths. The spectra measured at ELBE, at Felsenkeller and at Gran Sasso laboratories are shown (figure courtesy: Daniel Bemmerer, FZD). The laboratory background at Felsenkeller is about more than a factor of 10 lower than the laboratory background measured with a detector at earth's surface.

Italy) are given in Fig. 4.10. The deep underground laboratories like Gran Sasso in tunnels and mines far from the institutes are mainly used for the investigation of rare events in nuclear physics, whereas medium deep laboratories like Felsenkeller in the cellar or in the vicinity of institutes are applied to the measurements of larger series of samples.

At Felsenkeller, we use a well-type detector with 30% relative efficiency for the decay measurements. The detector properties are given in Table. A.2 of Appendix A. The efficiency of the detector has been measured with the calibration sources  $^{137}\text{Cs}$ ,  $^{65}\text{Zn}$ ,  $^{88}\text{Y}$  and  $^{60}\text{Co}$ . The decay properties of the sources are given in Table B.1 of Appendix B. Coincidence summing corrections were applied for multi-gamma emitting nuclides using the procedure discussed in Sect. B.2 of Appendix B. The photopeak efficiency curve for the 30% detector is shown in Fig. 4.11. The fit curve shown is an exponential fit of the first order.

The daughter nuclide originating from  $^{144}\text{Sm}(\gamma, \alpha)$  and  $^{144}\text{Sm}(\gamma, p)$  reactions were mainly studied at the Felsenkeller. The transition at 1596 keV following the  $^{140}\text{Nd}$  decay produced via the photodisintegration  $^{144}\text{Sm}(\gamma, \alpha)^{140}\text{Nd}$  was successfully detected at the Felsenkeller. A comparison of the sample measurement at ELBE to the measurements at Felsenkeller is shown in Fig. 4.12. It is clear that the cosmic background is noticeably lower in the spectra taken at Felsenkeller.

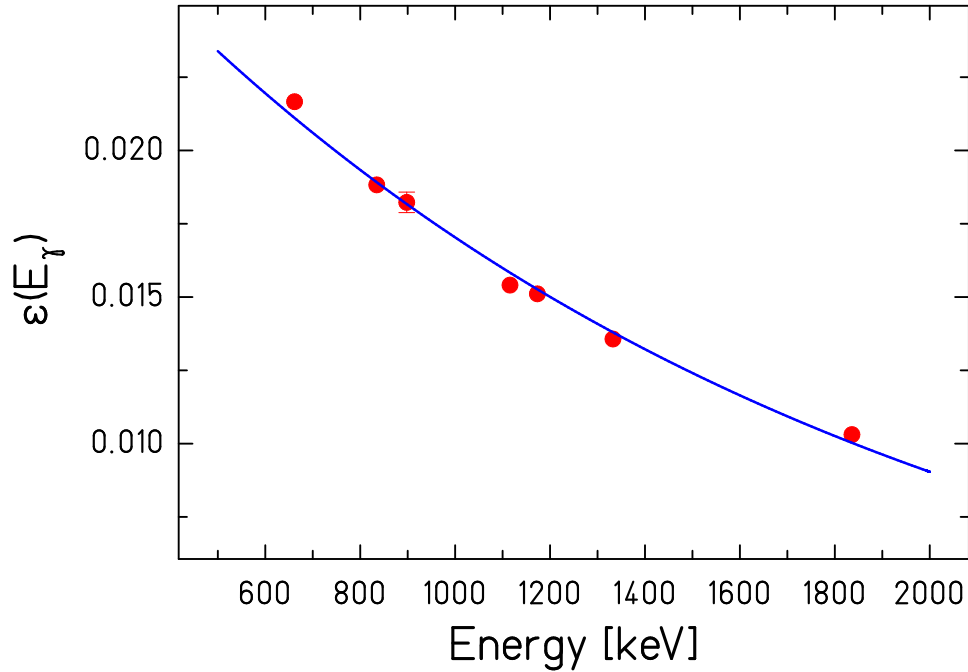


Figure 4.11: Full-energy peak efficiency curve for the 30% detector at Felsenkeller. The fit is an exponential function of first order.

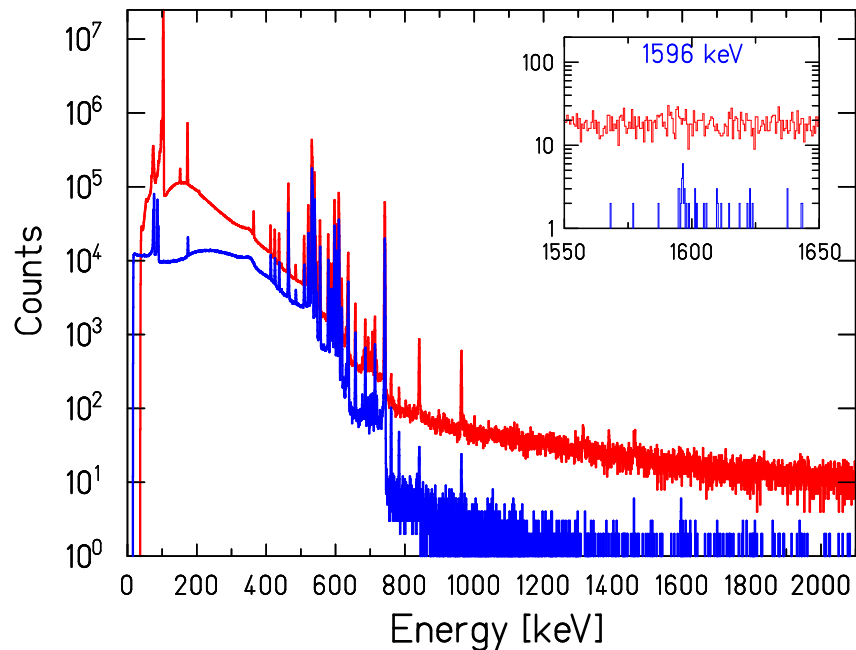


Figure 4.12: A comparison of the target measurement at ELBE (upper red spectrum) to the measurements at Felsenkeller (lower blue spectrum) for the decay originating from  $^{144}\text{Sm}(\gamma, \alpha)^{140}\text{Nd}$  reaction. The inset is a zoomed version of the high energy part of the spectrum from 1550-1650 keV. The cosmic background is noticeably lower in the spectrum taken at Felsenkeller and the line at 1596 keV is clearly visible (see inset).

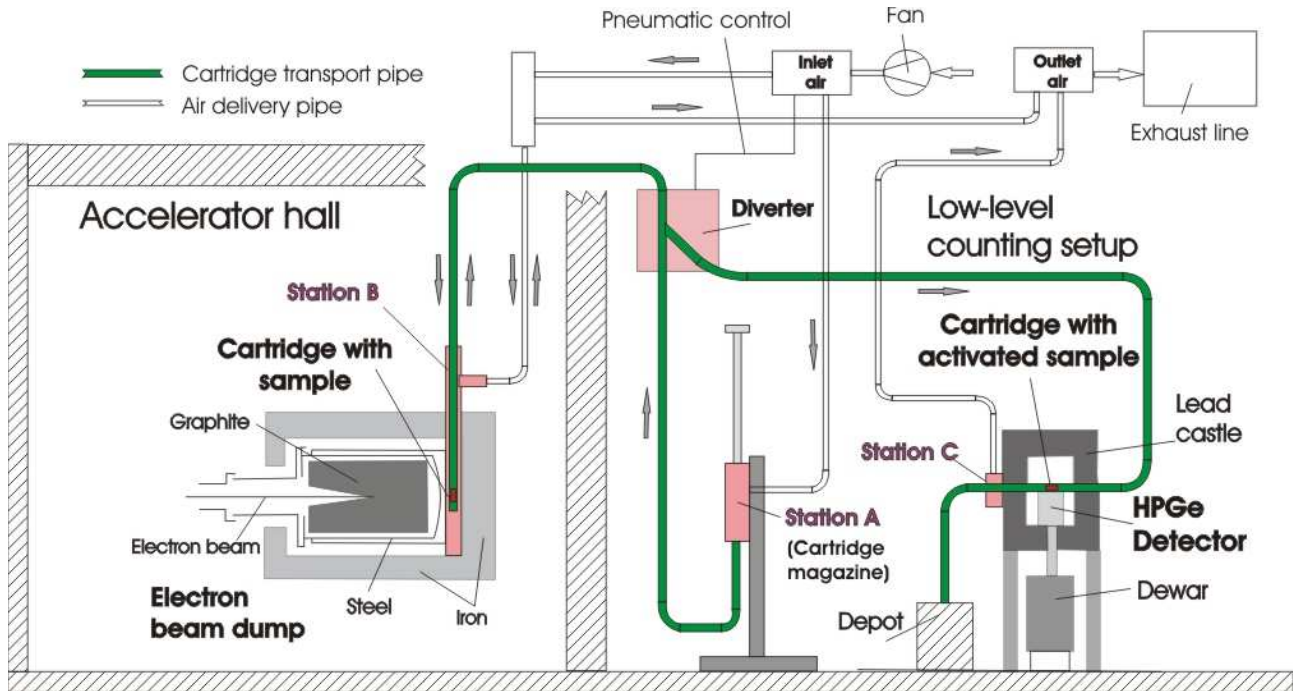


Figure 4.13: Pneumatic delivery system for fast transport of activated samples from the irradiation site to the decay measurement site. The different stations for sample loading (A), irradiation (B) and decay measurement (C) is shown.

### 4.3 The rabbit system

For measuring short-lived isotopes resulting from the activation experiment, we have built an air-driven pneumatic delivery system (*rabbit system*) [Nair08a]. A sketch of the setup is shown in Fig. 4.13.

The whole system uses compressed air to transport the samples through polyamide (PA) tubes with a diverter making way to the to-and-fro movement of the sample cartridges. The samples to be irradiated are enclosed in polyethylene cassettes and loaded in Station A. They are shot to the photoactivation site behind the vacuum steel vessel aligned on the axis of the electron beam (Station B). After irradiation, the samples are transported within about 15 s to the lead-shielded low-level counting setup where the decay is measured with a coaxial HPGe detector of relative efficiency 90% (Station C). The loss time of 15 seconds arises from the transport time of the sample plus placing the sample exactly on the top center of the HPGe detector. After the decay measurement, samples are shot to a radiation shielded container (depot, see figure). As an example, the gamma-ray spectrum of an activated sample of  $^{197}\text{Au}$  after 10 minutes of irradiation using the rabbit system is shown in Fig. 4.14. The decays following the  $^{197}\text{Au}(\gamma, n)$  and  $^{197}\text{Au}(n, \gamma)$  reactions with half-lives 6.2 days and 2.6 days respectively are shown. In particular, the decay of the isomeric state in  $^{197}\text{Au}$  with half life of  $7.73 \pm 0.06$  seconds [ENDSF] is identified by the  $\gamma$ -rays at 202 and 279 keV. The half-life of isomeric transition in  $^{197}\text{Au}$  has been determined using the exponential decay of  $^{197m}\text{Au}$ , identified with the  $\gamma$ -transition at 279 keV (see Fig. 4.15). The half-life was determined to be  $7.79 \pm 0.12$  s which is in agreement with the literature value of  $7.73 \pm 0.06$  s [ENDSF]. The decay properties of the daughter nuclei stemming from  $^{197}\text{Au}(\gamma, n)$  reaction is given in detail in Table. D.1 of Appendix D.

For irradiation and measurement using the rabbit system, we designed completely automated

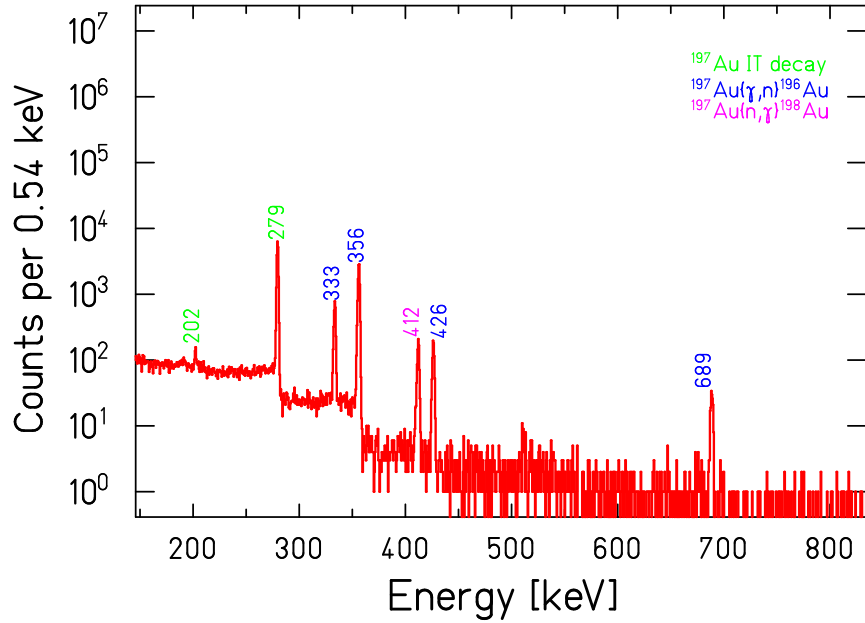


Figure 4.14: Decay spectrum following the reaction  $^{197}\text{Au}(\gamma, n)$ . The  $\gamma$ -ray energies are marked for the transitions from the decay of the isomeric state of  $^{197}\text{Au}$  which is short-lived (half-life of 7.73 s), and for the decay of the daughter nuclides stemming from  $^{197}\text{Au}(\gamma, n)$  and  $^{197}\text{Au}(n, \gamma)$  reactions. The target was irradiated for 10 minutes, the spectrum shown here is for a measurement period of 10 minutes.

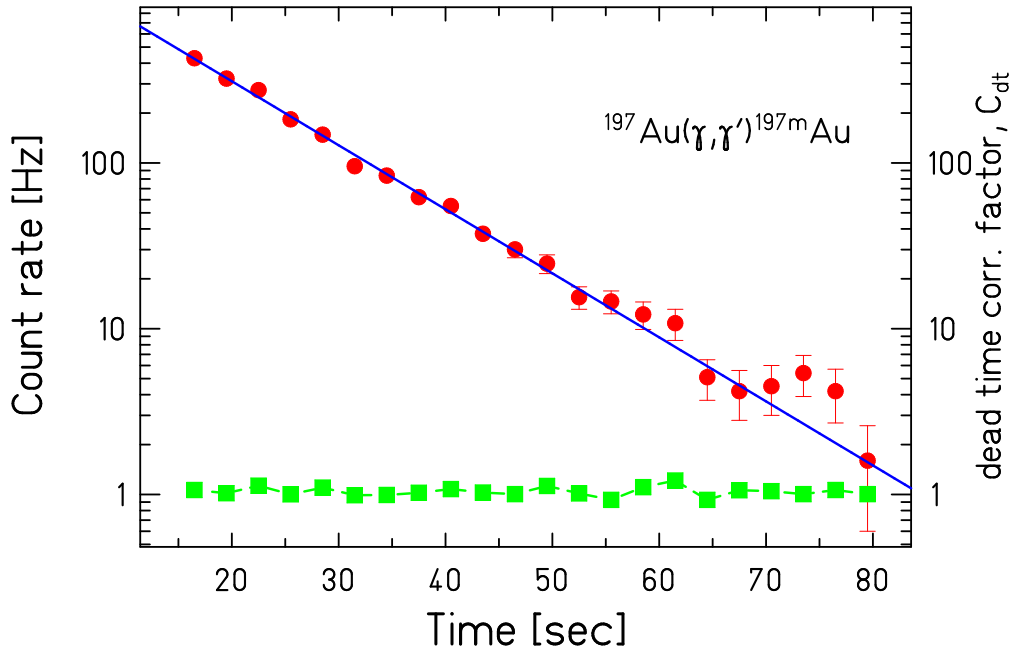


Figure 4.15: Half-life determination using the exponential decay of  $^{197m}\text{Au}$  (circles), identified with the  $\gamma$ -transition at 279 keV. The half-life was determined to be  $7.79 \pm 0.12$  s which is in agreement with the literature value ( $7.73 \pm 0.06$  s). The dead time correction factor  $C_{dt}$  is also shown (squares).

control modules with a LabVIEW<sup>2</sup> (Laboratory Virtual Instrumentation Engineering Workbench) program. The cycles of irradiation and measurement were controlled by the job files using the software addressable *change sample* or *sample ready* signals. To initiate the *change sample* signals, either the built-in signals from the ORTEC 919E module or the signals created using the specially designed acquisition system CAP were used. To actuate signals from the ORTEC 919E module, MAESTRO job files (see Sect. 4.2.1) including commands to initiate the sample change signals were used.

CAP(CAMAC Acquisition through PCI) is a CAMAC based data acquisition system developed at our institute [Faut07]. It consists of NIM and CAMAC modular electronics that are interfaced with the PCI bus of a personal computer by means of the CAMAC controller WIENER CC32. It is used for list mode data acquisition that allows data analysis with varying count rates, which is necessary for the evaluation of fast decaying samples. For the online data display, we used either the MAESTRO or the graphical user interface gCAP associated with the CAP acquisition system. The dead time of the system was determined on an event-by-event basis.

## 4.4 Corrections for self-absorption and target dimensions

The efficiency calibration using point-like sources has been discussed in Sect. 4.2.1. However, the targets used for the experiments discussed in this thesis were not always point-like. Different target dimensions were used depending on whether the decay measurement was done *manually* or using the rabbit system.

For example, the photodisintegration reaction  $^{144}\text{Sm}(\gamma, n)$  results in short-lived nuclei compared to the ones in  $^{144}\text{Sm}(\gamma, \alpha)$  or  $^{144}\text{Sm}(\gamma, p)$  reactions (see Table. D.1, Appendix D). For the latter ones, one could take out the sample from the irradiation site and put it on the detector *manually* whereas for the former one, the use of a rabbit system discussed in the previous section was necessary.

For the *manual* measurements, we used  $\text{Sm}_2\text{O}_3$  powder filled into cylindrical cans of radius 9 mm and height 5 mm. In such a situation, the photopeak efficiencies have to be corrected for the source extension. For this purpose, the Monte-Carlo efficiency transfer code EFF-TRAN [Vidm05] was used. By using a geometrical grid of point source efficiencies, the efficiency for an extended source is calculated by Monte-Carlo integration. The point source efficiency has been measured with the point source shifted to a distance which corresponds to the middle of the volume target. The point source efficiency is reduced by 7% in the center of the volume target, as compared to the top of cadmium absorber. The volume source effect is only 4%, comparing the point source in the center of the  $\text{Sm}_2\text{O}_3$  sample and a volume target  $\text{Sm}_2\text{O}_3$  placed on the top of the cadmium absorber. The  $^{197}\text{Au}$  activation standard targets were very thin discs (mass - 100 mg, thickness - 0.2 mm, radius - 9 mm) and the volume effect correction was not significant.

For experiments using the rabbit system, the target dimensions are different and are given in Table. 4.1. Under normal experimental conditions, the bottom of the pneumatic delivery tube touches the top of the Cd absorbers which are placed directly on top of the HPGe crystal (see Fig. 4.16). The tube has an outer diameter of 28 mm and an inner diameter of 23 mm. The cassettes used for mounting the target are made of polyethylene and have the following

---

<sup>2</sup>National Instruments Corporation, 11500 N Mopac Expwy, Austin, Texas, USA.

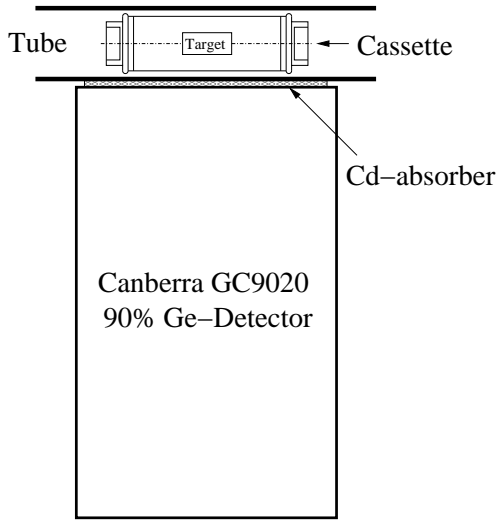


Figure 4.16: The measuring geometry for experiments using the rabbit system. The pneumatic delivery tube touches the top of the Cd absorber. Cassette is shown schematically inside the tube with the target mounted. For detailed dimensions, see text.



Figure 4.17: The cassettes used for mounting targets in measurements with rabbit system. a) The cassettes (either made of polyethylene or aluminum), compared to a pen to have a feeling of the dimensions. b) The cassette with Sm target mounted. The target is  $\text{Sm}_2\text{O}_3$  powder filled into a cylinder with dimensions given in Table. 4.1.

dimensions : outer diameter = 22 mm, length = 55.3 mm and thickness = 1 mm. Thus there is always 1 mm of air gap in the space between the pneumatic delivery tube and cassette.

target	form	$N_{nat}$ / %	$l$ / mm	$d$ / mm	mass / mg	$E_\gamma$ / keV	$C_{vol}$
Au	metal foil	100	36	5	200 - 250	333.03(5)	0.918(2)
						355.73(5)	0.925(2)
						426.10(8)	0.943(2)
$\text{Sm}_2\text{O}_3$	powder	3.1	16	10	2000 - 3000	754.4(7)	0.967(3)
						1056.58(7)	0.981(3)
						1173.18(7)	0.978(3)
						1403.06(7)	0.984(4)
						1514.98(7)	0.988(4)

Table 4.1: Dimensions of the targets used for decay studies with rabbit system. The natural abundance ( $N_{nat}$ ), length, thickness and mass ( $l, d, m$ ) of the targets are given.  $C_{vol}$ , the correction for volume source effect (see text) is given for the strongest decay lines ( $E_\gamma$ ) indicated.

A photograph of the cassette and target is shown in Fig. 4.17. The Au targets were sheets rolled to the dimensions given in Table. 4.1 where as the Sm targets were  $\text{Sm}_2\text{O}_3$  powder filled into a cylinder with dimensions given in Table. 4.1. The photopeak efficiency was measured with

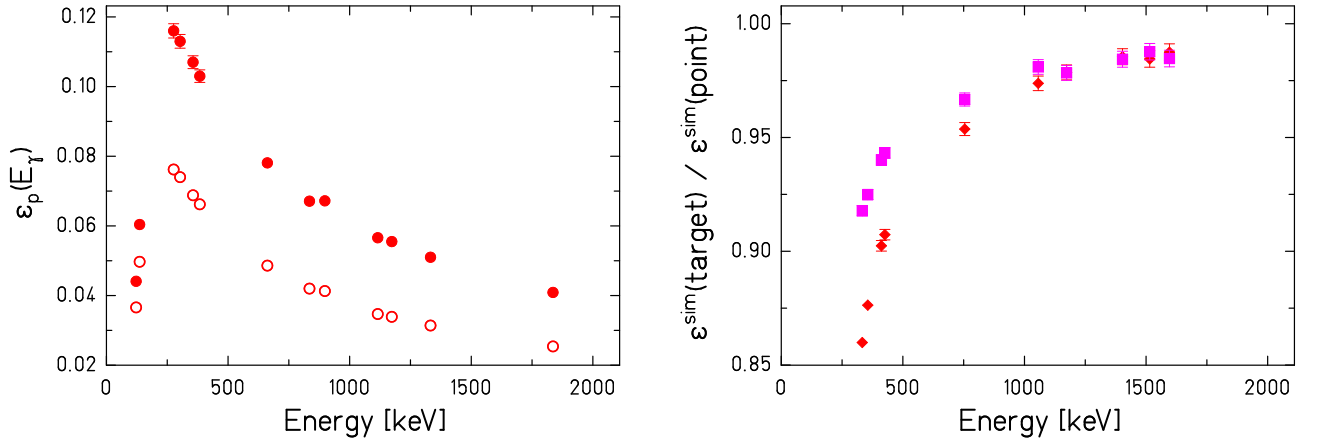


Figure 4.18: Absolute photopeak efficiencies for volume targets. On the left panel, a comparison of the efficiency curve for point-like sources directly on top of the Cd absorber (circles) and at a distance corresponding to the distance of the center of the volume target to the HPGe crystal (open circles) is given. The ratio of the volume and point efficiencies calculated using GEANT3 for the Au (squares) and Sm (diamonds) targets is given on the right panel.

point sources directly on the top of the cadmium absorber and at a distance corresponding to the distance of the center of the volume target to the HPGe crystal. A comparison is given in Fig. 4.18. The EFFTRAN code cannot be used for correcting the photopeak efficiency of targets with cylindrical dimensions. To account for the volume source effect, detailed simulations using GEANT3 were performed. The ratio of the volume and point efficiencies calculated using GEANT3 for the Au and Sm targets is given in Fig. 4.18.

The absolute photopeak efficiency for the rabbit system target dimensions is given by

$$\epsilon_{\text{target}}(E_\gamma) = \epsilon_{\text{point}}(E_\gamma) \cdot \frac{\epsilon_{\text{target}}^{\text{sim}}(E_\gamma)}{\epsilon_{\text{point}}^{\text{sim}}(E_\gamma)} \quad (4.6)$$

The efficiencies were measured with point-like sources at a distance 15.035 mm from the HPGe crystal ( $\epsilon_{\text{point}}(E_\gamma)$ ). This corresponds to the distance of the center of the volume target to the HPGe crystal. The simulated photopeak efficiencies for volume and point-like targets are denoted by  $\epsilon_{\text{target}}^{\text{sim}}$ ,  $\epsilon_{\text{point}}^{\text{sim}}$  respectively. The ratio is the correction to be applied for the volume source effect. The correction factor  $C_{\text{vol}} \left( \frac{\epsilon_{\text{target}}^{\text{sim}}(E_\gamma)}{\epsilon_{\text{point}}^{\text{sim}}(E_\gamma)} \right)$  for the  $\gamma$ -energies of short lived isotopes resulting from activation (for details about half-lives etc., see Table. D.1 of Appendix D) is given in Table. 4.1.





# Chapter 5

## Experimental results

In this Chapter, the results of the photoactivation experiments on the p-nuclei  $^{92}\text{Mo}$  and  $^{144}\text{Sm}$  are presented. The experimental activation yield is compared to the activation yield calculated using cross sections from previous experiments and using cross sections predicted by Hauser-Feshbach models. The activation yield data normalized to the photon fluence, are always plotted as a function of the bremsstrahlung endpoint energies.

The first section of this chapter briefly describes the basic assumptions of statistical model calculations. An overview of the two different model codes used in this thesis is presented. The next sections are dedicated to the activation yield results for the activation standard reaction  $^{197}\text{Au}(\gamma, n)$  and for the photodisintegration reactions on  $^{92}\text{Mo}$  and  $^{144}\text{Sm}$ .

### 5.1 The statistical model

For performing complete network calculations, information about the cross sections and astrophysical reaction rates for a large number of nuclei are necessary. Despite the several experimental efforts, many of the involved nuclei are presently not accessible in the laboratory. For most of the nuclear reactions in astrophysics, the predictions for reaction rates are theoretically provided by the statistical model, for e.g, by the Hauser-Feshbach approach [Haus52]. The basic ideas of the statistical model are presented in this section.

The low energy nuclear reactions are usually dominated by compound-nucleus reactions where the target nucleus and projectile form an excited compound system. The compound nucleus is characterized by excitation energy, angular momentum and parity. The excitation energy is distributed over all degrees of freedom of the compound nucleus whereas any other memory in the entrance channel is lost. The de-excitation phase is described by the statistical model.

For the reaction of the type  $i^\mu(j, o)m^\nu$ , from the target state  $i^\mu$  to the excited state  $m^\nu$  of the final nucleus, the reaction cross section  $\sigma^{\mu\nu}$  is given by

$$\begin{aligned} \sigma^{\mu\nu}(E_{ij}) &= \frac{\pi \hbar^2 / (2\mu_{ij} E_{ij})}{(2J_i^\mu + 1)(2J_j + 1)} \sum_{J, \pi} (2J + 1) \\ &\times \frac{T_j^\mu(E, J, \pi, E_i^\mu, J_i^\mu, \pi_i^\mu) T_o^\nu(E, J, \pi, E_m^\nu, J_m^\nu, \pi_m^\nu)}{T_{tot}(E, J, \pi)} \end{aligned} \quad (5.1)$$

In this expression, it is assumed that the reaction involves many compound states of spin  $J$  and parity  $\pi$  that can be excited. The center of mass energy is denoted by  $E_{ij}$  and reduced mass by  $\mu_{ij}$ . In this expression, it is assumed that the corresponding wave functions of the various

transitions have random phases and  $\sigma^{\mu\nu}$  is given by the sum over all participating compound states [Raus00]. In Eq. 5.1, when the properties are used without subscripts they describe the compound nucleus, subscripts refer to states of the participating nuclei in the reaction  $i^\mu(j, o)m^\nu$  and superscripts indicate the specific excited states.

The total transmission coefficient  $T_{tot}$  describes the transmission into all possible bound and unbound states  $\nu$  in all energetically accessible exit channels  $o$  (including the entrance channel  $i$ ) and is given by

$$T_{tot} = \sum_{\nu, o} T_o^\nu \quad (5.2)$$

In Eq. 5.1, the summation over  $\nu$  replaces  $T_o^\nu(E, J, \pi)$  by the total transmission coefficient into the exit channel  $o$ ,

$$\begin{aligned} T_o(E, J, \pi) &= \sum_{\nu=0}^{\nu_m} T_o^\nu(E, J, \pi, E_m^\nu, J_m^\nu, \pi_m^\nu) \\ &+ \int_{E_m^{\nu_m}}^{E-S_{m,o}} \sum_{J_m, \pi_m} T_o(E, J, \pi, E_m, J_m, \pi_m) \\ &\times \rho(E_m, J_m, \pi_m) dE_m \end{aligned} \quad (5.3)$$

The channel separation energy is denoted by  $S_{m,o}$  and the summation over excited states above the highest experimentally known state  $\nu_m$  is changed to an integration over the level density  $\rho$ .

Form Eqs. 5.1 through 5.3, it is understood that the important ingredients of statistical model calculations are the particle and  $\gamma$ -transmission coefficients  $T$  and the level density of excited states  $\rho$ . The reliability of the statistical model calculations depends very much on the accuracy with which these different components can be evaluated. The difference between various model calculations are also based on the difference in these inputs. More details about the statistical model calculations are given in [Haus52, Raus00].

### 5.1.1 The model codes TALYS and NON-SMOKER

In this thesis, the experimental data is compared to the predictions of two advanced model codes TALYS (Koning et al., [Koni04]) and NON-SMOKER (Rauscher et al., [Raus04]) which are based on the Hauser-Feshbach formalism [Haus52]. Unless otherwise specified, the results discussed in this chapter were calculated using default nuclear physics inputs to these model codes, i.e.  $\gamma$ -ray strength functions, nuclear level densities and optical-model potentials.

The TALYS software has been written to simulate nuclear reactions<sup>1</sup> in the 1 keV - 200 MeV incident energy range and for target mass numbers between 12 and 339. It covers all main reaction mechanisms and provides a complete description of all reaction channels and observables. TALYS was created at the Nuclear Research and consultancy Group (NRG, Petten, Netherlands) and Commissariat à l'Énergie Atomique (CEA, Bruyères-le-Châtel, France).

The calculations in the context of this thesis were made with the current version of the code TALYS1.0. The default option of this code uses the neutron optical-model potential parameterizations by Koning and Delaroche [Koni03]. The model for  $\gamma$ -ray strength function is the so-called Brink-Axel model [Brin57, Axel62] in which a standard lorentzian is used to describe the shape of the giant dipole resonance. The nuclear level density model is based on an approach using the Fermi-gas model [Koni08, Eric60].

<sup>1</sup><http://www.talys.eu>

The NON-SMOKER code is widely used for the prediction of nucleosynthesis reaction rates [Raus04]. The complete NON-SMOKER database<sup>2</sup> contains Hauser-Feshbach statistical model results for  $9 < Z < 84$  (Ne to Bi). The code uses the neutron optical-model potential by Jeukenne et al. [Jeuk74] with a low-energy modification by Lejeune [Leje80]. The  $\gamma$ -ray strength function is based on a description by Thielemann and Arnould [Thie83]. The low-energy modification of the GDR Lorentzian is by McCullagh et al. [McCu81]. The nuclear level density implemented in the NON-SMOKER code is based on a global parametrization by Rauscher et al. [Raus97] within the back-shifted Fermi-gas formalism.

In this chapter, the results from both the TALYS and the NON-SMOKER codes are compared with the experimental results from ELBE. The dependence of these model codes to their input parameters will be discussed in the next chapter in detail.

## 5.2 Activation yield for the $^{197}\text{Au}(\gamma, n)$ reaction

At ELBE, the  $^{197}\text{Au}$  targets are irradiated both at the photon scattering site as well as the photoactivation site. The activation yield at the photon scattering site is determined and checked against the calculated yield using cross sections from previous experiments for consistency. The standardization method using the  $^{197}\text{Au}(\gamma, n)$  reaction has been published [Nair08b].

The targets used were natural samples of  $^{197}\text{Au}$  (Au is monoisotopic) with the dimensions given in Sect. 4.4. The number of activated nuclei produced during the activation was determined offline by measuring the decay of daughter nuclei in the low-level counting setup discussed in Sect. 4.2.1.

The  $^{197}\text{Au}(\gamma, n)$  reaction produces the unstable  $^{196}\text{Au}$  nucleus which decays either to  $^{196}\text{Pt}$  by electron capture or positron emission ( $\text{EC}+\beta^+$ ) or to  $^{196}\text{Hg}$  by beta-decay ( $\beta^-$ ). The  $\gamma$ -transitions stemming from the decays are shown schematically in Fig. 5.1 and Fig. 5.2. The  $\gamma$ -energies, half-lives, etc., were adopted from the online nuclear data tables [ENDSF].

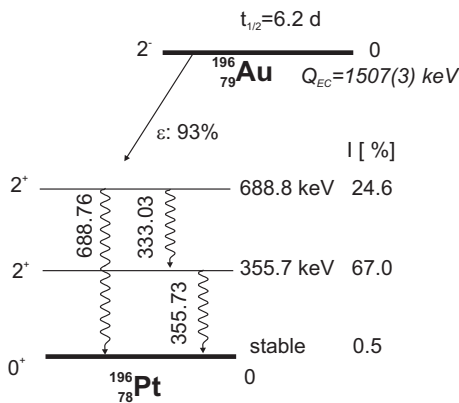


Figure 5.1: Decay scheme for the  $^{197}\text{Au}(\gamma, n)$  reaction. The transitions stemming from the electron capture decay of  $^{196}\text{Au}$  are shown.

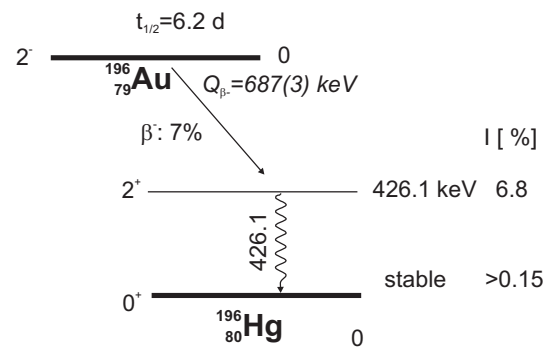


Figure 5.2: Decay scheme for the  $^{197}\text{Au}(\gamma, n)$  reaction. The transitions stemming from the beta decay ( $\beta^-$ ) of  $^{196}\text{Au}$  are shown.

A typical decay spectrum of a  $^{197}\text{Au}$  sample irradiated with bremsstrahlung of an endpoint energy 14.5 MeV for 17 hours is given in Fig. 5.3. The prominent peaks of the  $^{196}\text{Au}$  decay are marked and correspond to the ones given in Table D.1 of Appendix D. The spectrum shown

<sup>2</sup><http://nucastro.org/reaclib.html>

here was measured with a HPGe detector of 90% relative efficiency. The absolute efficiency of the detector has been determined as discussed in Sect. 4.2.1.

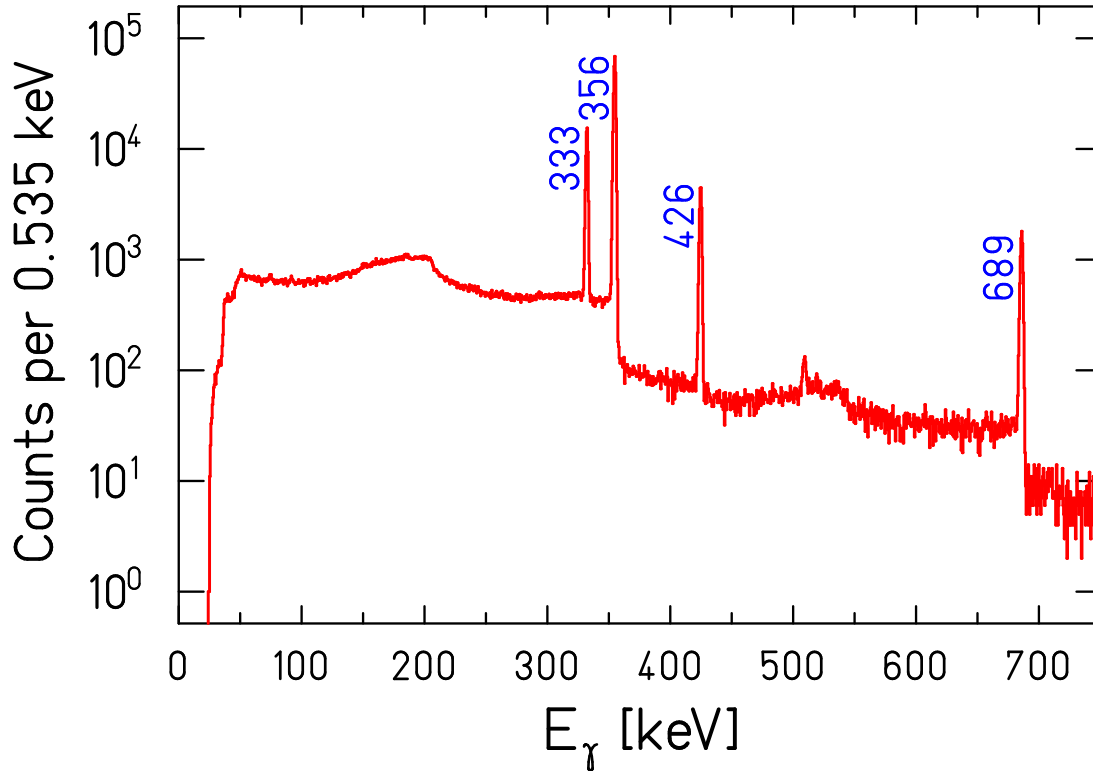


Figure 5.3: Spectrum of an irradiated  $^{197}\text{Au}$  target. The peaks originating from the  $^{196}\text{Au}$  decay are marked. The target was placed on top of the 90% HPGe detector. A 1.5 mm thick Cd absorber was used to suppress coincidence summing and low energy X-rays.

The coincidence summing effects depend strongly on the decay scheme and were determined for the corresponding counting geometry. The three prominent transitions in the  $^{196}\text{Au}$  decay used for analysis are at 333, 356 and 426 keV. The direct decay of the level at 689 keV into the ground state is obscured by coincidence summing of the 333 and 356 keV decay lines. The number of  $\gamma$ -rays counted at 333 and 356 keV lines have been corrected for 'summing-out' events using the method described in Sect. B.2 of Appendix B. For the transition at 333 keV, the coincidence summing correction amounts to 24% and for 356 keV it is 6%, both with a relative uncertainty of 5%.

The activation yield has been determined by studying the  $^{196}\text{Au}$  decay using Eq. 3.4 described in Sect. 3.2. The experimental ELBE yield is compared to the calculated yield from previous experimental cross sections as described in the next section.

### 5.2.1 Comparison with previous experiments

The photoneutron cross section of  $^{197}\text{Au}$  has been measured by various methods on different grounds. It has been shown that the cross sections in the isovector GDR region as measured at different laboratories may differ beyond their statistical and systematic uncertainties [Diet88]. In this section, the experimental activation yield from ELBE is compared to calculated yields using cross sections measured in previous experiments. A comparison of the  $^{197}\text{Au}(\gamma, n)$  cross sections from previous experiments [Fult62, Berm87, Veys70, Vogt02, Hara07] is given in Fig. 5.4.

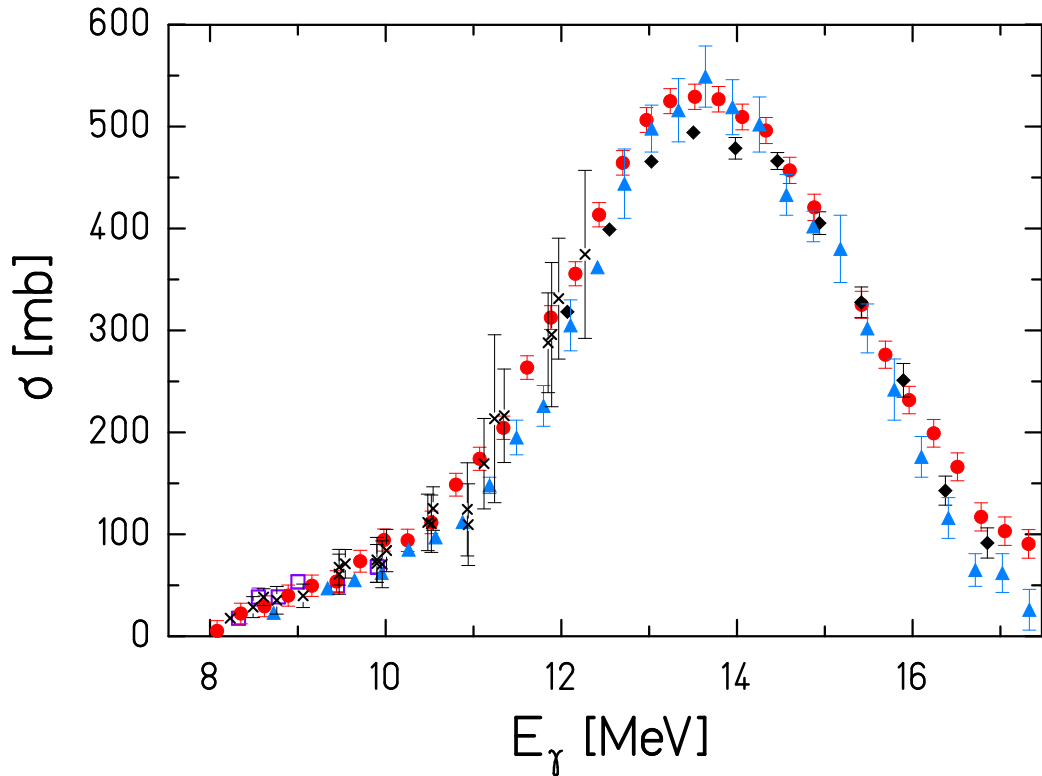


Figure 5.4: Photoneutron cross sections for  $^{197}\text{Au}(\gamma, n)$  from previous experiments. The symbols denote data from the respective experiments : triangles - Fultz et al. [Fult62], diamonds - Berman et al. [Berm87], circles - Veyssiere et al. [Veys70]. The cross sections measured by Veyssiere et al. have been rescaled by a factor of 0.93 based on a recommendation by Berman et al (Table VI, Ref. [Berm87]), see text for details. The  $^{197}\text{Au}(\gamma, n)$  cross section data below 10 MeV have been derived from bremsstrahlung activation by Vogt et al. (open squares) [Vogt02]. The cross sections determined from the Laser-Compton scattering experiment by Hara et al. ( $\times$ ) [Hara07] are also shown.

At the Lawrence Livermore National Laboratory (LLNL), the photoneutron cross section of the nucleus  $^{197}\text{Au}$  has been measured with quasi-monoenergetic photons from in-flight positron annihilation technique. There are two sets of published data - first by Fultz et al. [Fult62] and later by Berman et al. [Berm87]. The same technique has been used at Saclay (France) for studying photoneutron reactions on  $^{197}\text{Au}$  by Veyssiere et al. [Veys70]. The results from Livermore and Saclay disagree revealing the differences in the neutron multiplicity determination procedure used in both laboratories.

Berman et al. have remeasured photoneutron cross sections with quasi-monoenergetic photons at LLNL, with special emphasis on determining the absolute cross section at energies across the peak of the GDR. Based on this experiment, Berman et al. have recommended that the data given by Veyssiere et al. should be reduced by about 7% and the data of Fultz et al. should not be used at all (see Table VI, Ref. [Berm87]). This recommendation is taken into account for comparing the present ELBE data with the previously reported values.

At the Laser-Compton scattering facility at the TERAS storage ring at AIST Tsukuba, Japan quasi-monoenergetic photons were used to study photoneutrons from  $^{197}\text{Au}(\gamma, n)$  up to 12.4 MeV. These data agree very well with the data measured with the positron annihilation tech-

nique but as a photon difference method was used they have a rather large experimental uncertainty [Hara07].

The photoneutron cross section of  $^{197}\text{Au}$  for energies close above the  $(\gamma, n)$  threshold has been deduced by Vogt et al. [Vogt02] using photoactivation with bremsstrahlung at S-DALINAC (Darmstadt). The cross sections are in agreement with Veysiere et al., but they exist only for endpoint energies between 8.0 MeV and 10.0 MeV.

The total nuclear photoabsorption cross section of  $^{197}\text{Au}$  was measured at the synchrotron facility of the Institute of Nuclear Research (Moscow) by Gurevich et al. [Gure80]. Even though the data agree with the measurements by Veysiere et al., they scatter significantly (Fig. 2, Ref. [Gure80]). The tabulated errors are quite big and therefore were not included for comparison with the ELBE data reported here. The photoneutron yield for gold was measured by Sorokin et al. [Soro73], at a Betatron facility (Moscow State University) and the cross sections were deduced by the Penfold-Leiss [Penf59] method. This experiment was done with an energy resolution of 0.5 MeV for the range of energies considered here. The results from Sorokin et al. are not included in the present discussion because the uncertainties resulting from the unfolding process are quite large and the data itself differ significantly from the previous experimental data.

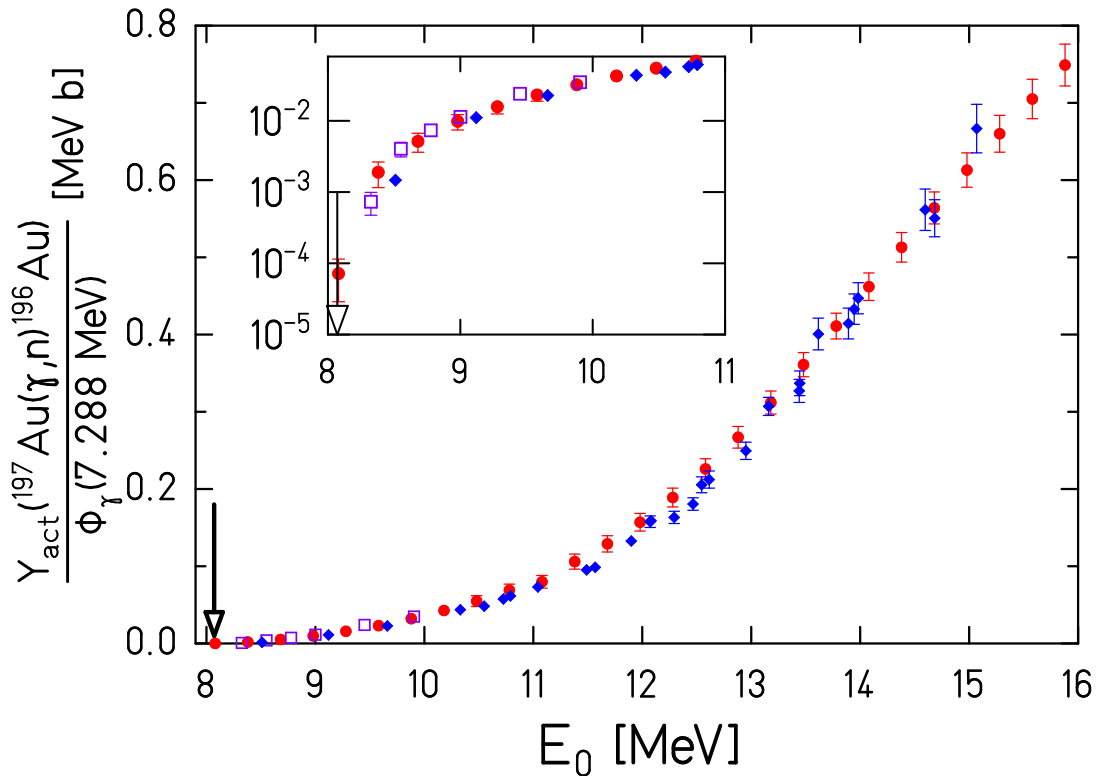


Figure 5.5: Activation yield for the  $^{197}\text{Au}(\gamma, n)$  reaction normalized to the photon fluence is compared to the yield calculated using cross sections measured in previous experiments. The present data are denoted by diamonds with an arrow pointing to the neutron emission threshold. Reaction yield calculated using the cross sections given by Veysiere et al. [Veys70] (circles) and Vogt et al. [Vogt02] (open squares) are in good agreement with the yield measured at ELBE. Based on the recommendation by Berman et al (Table VI, Ref. [Berm87]), the cross section data from Veysiere et al. have been rescaled by a factor of 0.93, see text for details.

In Fig. 5.5, the experimental activation yield from ELBE is compared to the yield calculated

using the cross sections measured previously. The activation yield is normalized to the photon fluence measured from the scattered photons in  $^{11}\text{B}$  (see Sect. 3.4). The experimental yield from ELBE is in agreement to the yield calculated by using the cross sections from Vogt et al. for the close-threshold endpoint-energies up to 10 MeV. The activation yield calculated using cross sections from Veysiere et al. is in agreement with the ELBE yield for the whole range of energies. Close to the neutron emission threshold, the reaction yield strongly depends on the precise value of endpoint energy  $E_0$  of the bremsstrahlung beam. In this case, small uncertainties in  $E_0$  result in large uncertainties of the activation yield.

The uncertainties in the experimental points shown in Fig. 5.5 are mainly from the determination of photon fluence as discussed in Sec. 3.4. The statistical uncertainties are very small and in the order of about 0.5-2%. The major systematic uncertainties arise from the extrapolation of measured photopeak efficiencies to the higher energies in  $^{11}\text{B}$  transitions (5%) and in the systematic deviation of measured photon fluence from the simulated curve (6%). The systematic errors have been added up quadratically and amount to about 7.8% but are not shown in Fig. 5.5.

### 5.2.2 Comparison with model calculations

In this section, the experimental activation yield is compared to the simulated yield calculated using cross sections predicted by Hauser-Feshbach models. From Fig. 5.6, it is evident that simulations using the TALYS and NON-SMOKER codes describe the experimental data only to a factor of 2. Both calculations were performed using cross sections derived from standard input parameters. The default option of TALYS for the GDR parameters originates from the Beijing GDR compilation, as present in the RIPL [RIPL-2] database.

In the case of  $(\gamma, n)$  reactions, one crucial ingredient for the model calculation is the photon strength function. As the  $(\gamma, n)$  channel in  $^{197}\text{Au}$  is the dominant decay channel for the energy range above threshold, the photon strength distribution directly determines the calculated  $(\gamma, n)$  cross section and the reaction yield. In the model calculations care is also taken for the fact that the  $(\gamma, p)$  channel is open above 5.8 MeV. Due to the large  $Z$  the  $p$ -emission is strongly suppressed by the Coulomb barrier. With default inputs, the TALYS calculation yields a  $(\gamma, p)$  cross section which is about four orders of magnitude smaller than the  $(\gamma, n)$  cross section.

The activation yields calculated using TALYS with different optical model potentials like Koning-Delaroche and Jeukenne-Lejeune-Mahaux (JLM) are very similar demonstrating that the  $^{197}\text{Au}(\gamma, n)$  reaction yield is not sensitive to the choice of optical model parameters. The sensitivity to the photon strength function is higher. We modified the deformation dependent parameters of the E1 strength function used in TALYS according to a new phenomenological parametrization. The improved new parametrization explains the experimental data better than the statistical models with default inputs and is discussed in the following section in detail.

### 5.2.3 Phenomenological parameterization of the photon strength function

If one assumes that the dipole strength in a heavy nucleus is dominated by the GDR then the strength function  $f_1(E_\gamma)$  according to Bartholomew et al. [Bart73] is related to the average photoabsorption cross section  $\langle\sigma_\gamma(E_\gamma)\rangle$  by

$$\frac{2J_0 + 1}{2J_x + 1} \cdot \frac{\langle\sigma_\gamma(E_\gamma)\rangle}{(\pi\hbar c)^2 E_\gamma} = f_1(E_\gamma) = \frac{\langle\Gamma_{E_1}\rangle}{E_\gamma^3 \cdot D}, \quad (5.4)$$

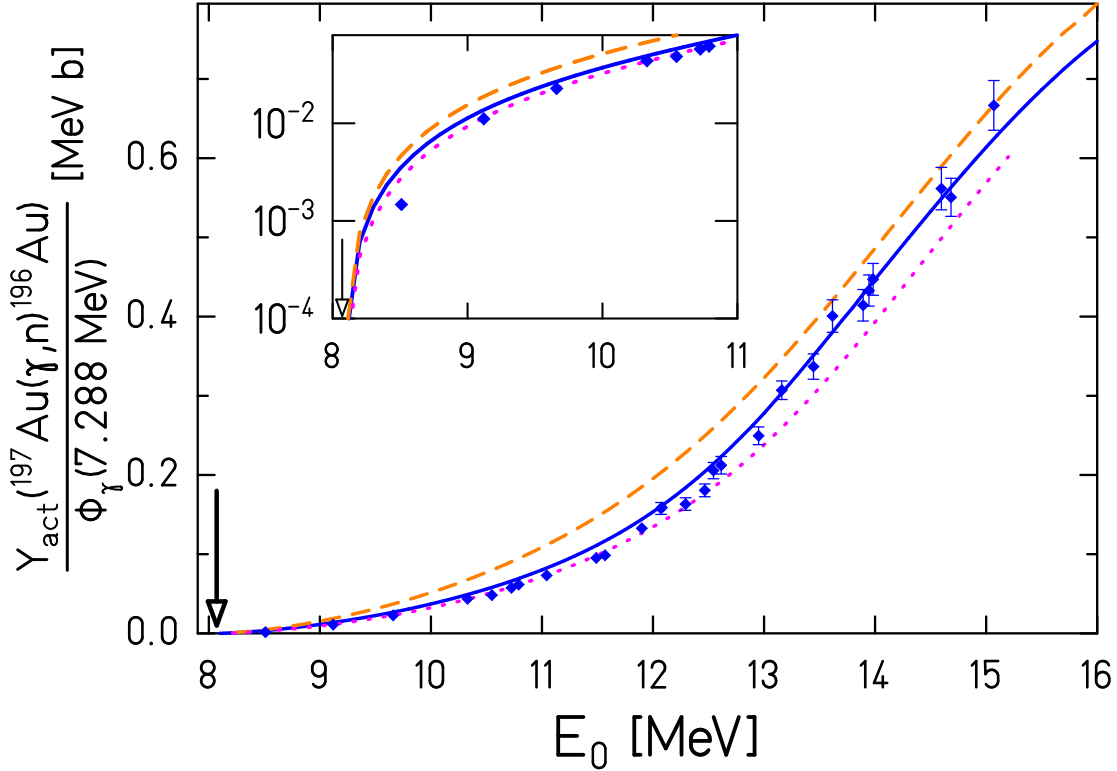


Figure 5.6: Experimental activation yield normalized to the photon fluence for the  $^{197}\text{Au}(\gamma, n)$  reaction compared to theoretical model calculations. The experimental data are denoted by diamond symbols with a downward arrow denoting the neutron emission threshold. The dashed and dotted lines denote yield calculations using cross sections from TALYS and NON-SMOKER codes respectively. The solid line represents a TALYS calculation with modified inputs, see text.

with  $\langle \Gamma_{E_1} \rangle$  and  $D$  denoting the average photon width and the average level distance at the endpoint of electromagnetic transition.  $J_0, J_x$  denote the spins of ground and excited states respectively. A new phenomenological description based on the ground state deformation parameters describes well the average photon absorption for nuclei with  $A > 80$  from  $E_x \approx 4$  MeV up to several MeV above the GDR [Jung08]. In particular, results from the detailed studies on the photon strength distributions in stable even-even molybdenum isotopes are given in [Wagn08].

A consistent description holds for the photon strength distribution in spherical, transitional, triaxial and well deformed nuclei. In nearly all nuclei the GDR is split into two or three components, whose energies are well predicted by the finite range droplet model (FRDM) [Myer77]. The splitting [Bush91] is due to the three different axes of the ellipsoid parameterizing the nuclear shape with its deformation parameter  $\beta$  and triaxiality parameter  $\gamma$ :

$$E_k = \frac{E_0 \cdot R_0}{R_k} = \frac{E_0}{\exp \left[ \sqrt{\frac{5}{4\pi}} \cdot \beta \cdot \cos \left( \gamma - \frac{2}{3} k \pi \right) \right]} \quad (5.5)$$

This results from the fact that the vibrational frequency  $E_k/\hbar$  along a given axis  $k$  is inversely proportional to the corresponding semi-axis length  $R_k$ . The nuclear radius is parameterized by  $R_0 = 1.16A^{1/3}\text{fm}$ . The GDR centroid energy  $E_0$  given in Ref. [Myer77] of a spherical nucleus with mass  $A$  is calculated with an effective nucleon mass of  $874 \text{ MeV}/c^2$ .



The average absorption cross section in the GDR is given by

$$\langle\sigma_\gamma(E_\gamma)\rangle = \frac{1.29 \cdot Z \cdot N}{A} \sum_{k=1}^3 \frac{E_\gamma^2 \Gamma_k}{(E_k^2 - E_\gamma^2)^2 + E_\gamma^2 \Gamma_k^2} \quad (5.6)$$

where the GDR widths  $\Gamma_k$  to be used in the sum of up to three Lorentzians have been assumed to be constant, in contrast to earlier descriptions [Kope90, Zani03]. The symbols  $E_\gamma$ ,  $E_k$  denote photon energy and resonance energies given in MeV and  $\langle\sigma_\gamma(E_\gamma)\rangle$  given in  $\text{fm}^2$ . The Thomas-Reiche-Kuhn sum rule as determined from general quantum mechanical arguments [Eise88] is included in this description for the average photon absorption cross section obtained on an absolute scale.

The width  $\Gamma_k$  for the different components of the GDR is dependent on the resonance energy  $E_k$  and is generally used for all stable nuclei with  $A > 80$

$$\Gamma_k(E_k) = 1.99 \text{ MeV} \cdot \left( \frac{E_k}{10 \text{ MeV}} \right)^\delta, \quad (5.7)$$

where  $\delta = 1.6$  is taken from the one body dissipation model [Bush91].

For the case of  $^{197}\text{Au}$  we assume that the average of the deformation parameters of the even-mass neighbor nuclei  $^{196}\text{Pt}$  and  $^{198}\text{Hg}$  [Maut90, Bock79] can be used to describe the shape of the odd nucleus  $^{197}\text{Au}$ , we insert  $\beta = 0.15$  and  $\gamma = \frac{\pi}{3}$  into Eq. (5.5). The GDR centroid energy is  $E_0 = 13.9$  MeV. These parameters are in accordance to the FRDM and result in the following resonance energies and widths:  $E_{1,3} = 13.2$  MeV,  $\Gamma_{1,3} = 3.1$  MeV and  $E_2 = 15.2$  MeV,  $\Gamma_2 = 3.9$  MeV. The TALYS code was modified with these inputs for oblate deformation. The yield curve created using the cross sections resulting from modified inputs is shown in Fig. 5.6 and is in better agreement to the ELBE data.

The photon strength function of  $^{197}\text{Au}$  derived from different theoretical models and compared to experimental data is shown in Fig. 5.7. The strength function created using the modified inputs as discussed above is compared to the default models [Brin57, Axel62, Kope90] in TALYS which treat  $^{197}\text{Au}$  as a spherical nucleus. It is clear that the new parameters lead to a reduced strength at energies below the GDR and thus describe its shape well with a constant spreading width. This agrees well to the experimental strength function given by Bartholomew et al. [Bart73] for energies below the neutron emission threshold. Above the separation energy, the strength functions shown were deduced from the  $^{197}\text{Au}(\gamma, n)$  cross sections by Veyssiere et al. The strength function derived using the modified parameters gives a clearly better fit to the data than calculations [Gori02, Khan01] on the basis of the quasi-particle random-phase approximation (QRPA) with phenomenological correction for deformation.

### 5.3 Photodisintegration of $^{144}\text{Sm}$

The photodisintegration reactions  $(\gamma, n)$ ,  $(\gamma, p)$  and  $(\gamma, \alpha)$  of  $^{144}\text{Sm}$  are shown in a nuclide chart in Fig. 5.8. In  $^{144}\text{Sm}$ , the neutron separation energy is 10.5 MeV and the proton separation energy 6.7 MeV. The bremsstrahlung endpoint energies of irradiation were chosen for each reaction accordingly. The photoactivation process and the resulting daughter decays are shown schematically in Fig. 5.9.

For the activation of samarium we used fine  $\text{Sm}_2\text{O}_3$  powder filled in polyethylene capsules with dimensions chosen according to the particular technique used (manual or rabbit system, see Sect. 4.4). Au targets were irradiated both at the photoactivation and photon scattering sites

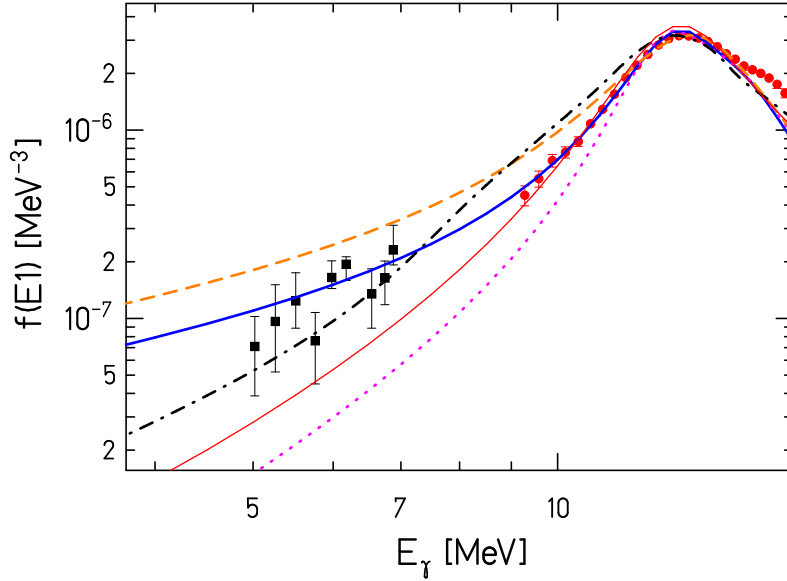


Figure 5.7: The photon strength function of  $^{197}\text{Au}$  derived on the assumption of oblate deformation (solid line) compared to different models. The dashed and dotted lines correspond to the strength functions given by Brink-Axel [Brin57, Axel62] and Kopecky-Uhl [Kope90] models respectively. The microscopic E1 photoabsorption strength-functions determined within a QRPA model [Gori02, Khan01] is shown by the dash-dotted line. All calculations were done using the Talys Code. The Enhanced Generalized Lorentzian (EGLO) model taken from the Reference Input Parameter Library RIPL-2 of the IAEA [RIPL-2] is shown as a thin solid line. The experimental strength function from Bartholomew et al. [Bart73] (squares) below the neutron emission threshold and the strength function derived using the  $^{197}\text{Au}(\gamma, n)$  photoneutron cross section measured by Veysiere et al. (circles) are also shown. For determining the dipole strength function, the cross sections measured by Veysiere et al. have been renormalized by a factor of 0.93, based on the recommendation by Berman et al (Table VI, Ref. [Berm87]), see text for details.

for flux normalization purposes. The irradiated targets were studied using the gamma-detection methods discussed in Chapter 4. The activation yield normalized to the photon fluence for the photodisintegration of  $^{144}\text{Sm}$  are discussed in the next sections in detail.

## 5.4 Activation yield for the $^{144}\text{Sm}(\gamma, n)$ reaction

The  $^{144}\text{Sm}(\gamma, n)$  reaction produces  $^{143}\text{Sm}$  or  $^{143m}\text{Sm}$ . Since both radionuclides produced are short-lived, the irradiation was carried out using the rabbit system (see Sect. 4.3). The irradiation was performed for various endpoint energies starting with  $E_0 = 11.00$  MeV which is 4.81 MeV above the neutron separation energy. The dimensions of the  $\text{Sm}_2\text{O}_3$  and Au targets used for irradiation is given in Table 4.1 of Sect. 4.4. The irradiation period for this experiment lasted between 15-45 minutes.

The gamma-ray spectrum of an activated sample of samarium after 10 minutes of irradiation using the rabbit system is shown in the left panel of Fig. 5.10. In the overlaid figure, the upper spectrum was taken 1 minute after the irradiation and the lower one after 9 minutes. The decays following  $^{144}\text{Sm}(\gamma, n)^{143m}\text{Sm}$  and  $^{144}\text{Sm}(\gamma, n)^{143}\text{Sm}$  reactions with half-lives 66 s and 8.75 min respectively are clearly seen. The  $^{144}\text{Sm}(\gamma, n)^{143m}\text{Sm}$  reaction is identified with the

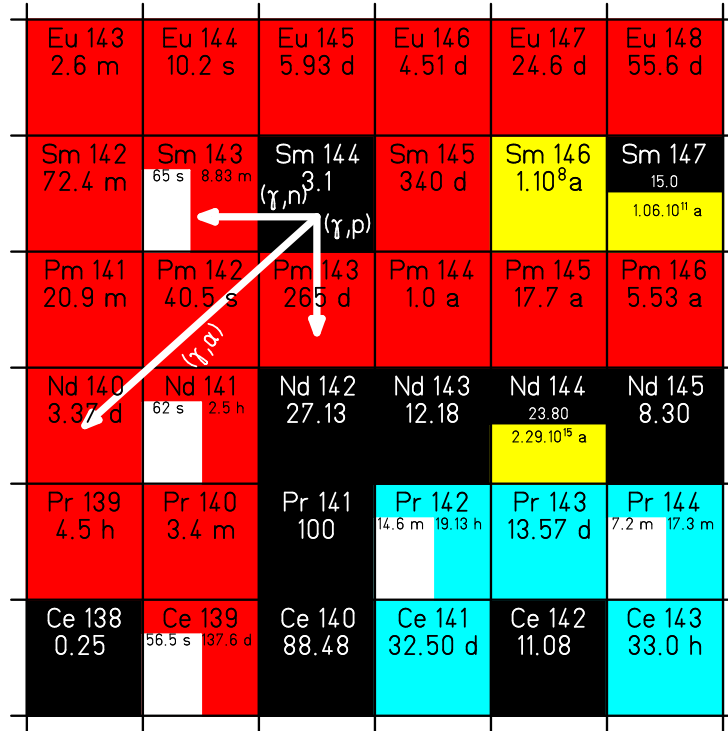


Figure 5.8: The photodisintegration reactions  $(\gamma, n)$ ,  $(\gamma, p)$  and  $(\gamma, \alpha)$  on  $^{144}\text{Sm}$ .

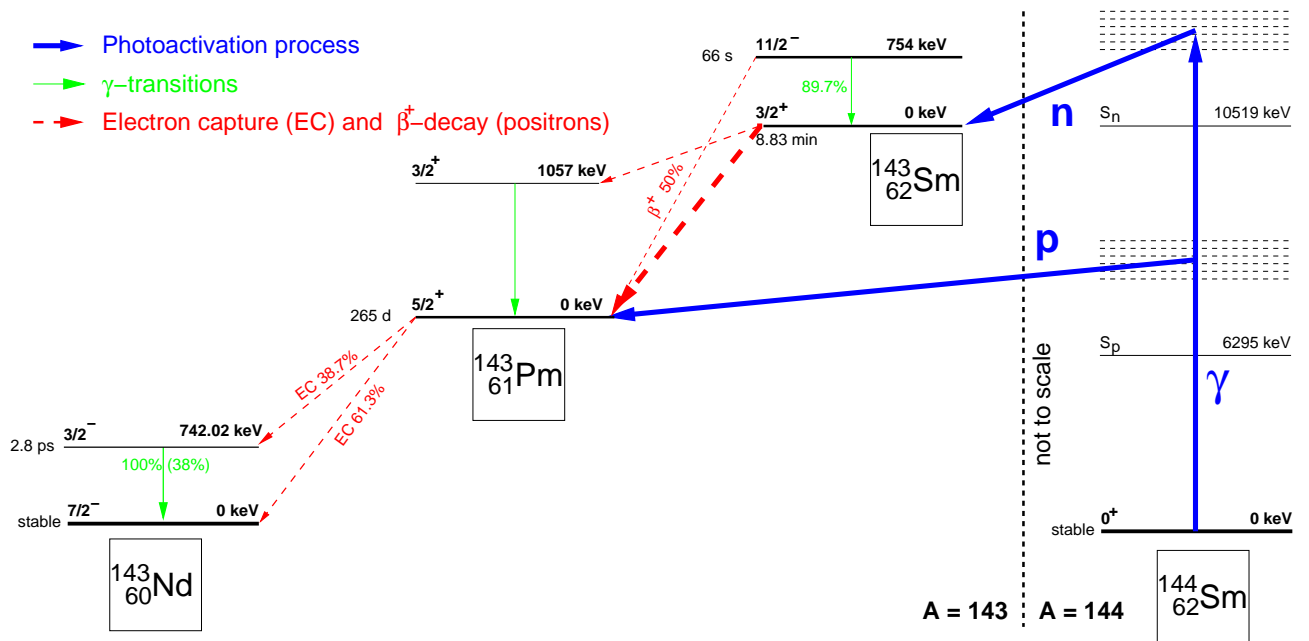


Figure 5.9: Decay scheme for the  $^{144}\text{Sm}(\gamma, p/n)$  reaction (not to scale). The neutron separation energy is well above the proton separation energy. The  $(\gamma, n)$  activation mainly populates the ground and isomeric states of  $^{143}\text{Sm}$ . The photoactivation process is shown with a thick arrow, gamma-transitions from daughter decays with thin arrows, and the electron capture and/or  $\beta$ -decay with dotted arrows.

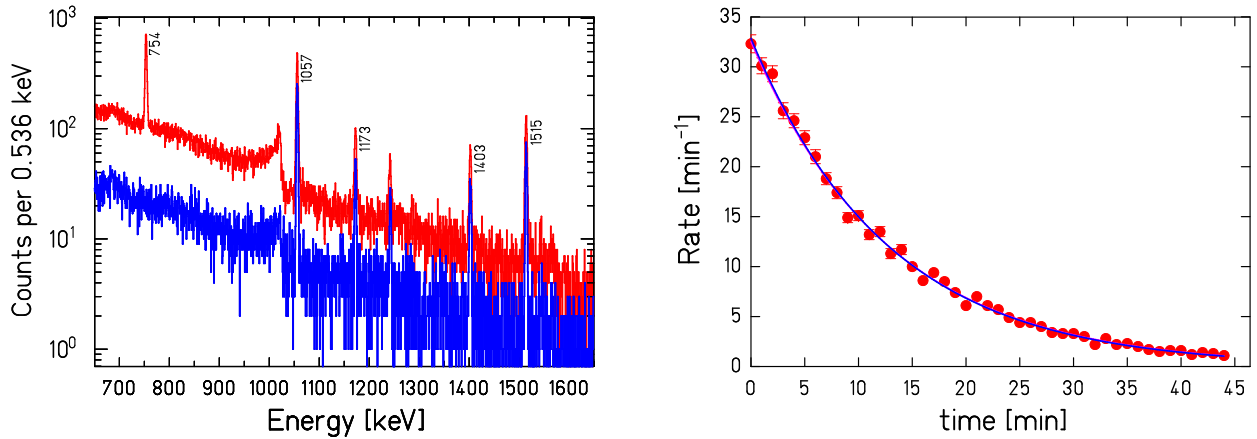


Figure 5.10: Decay spectrum following the reaction  $^{144}\text{Sm}(\gamma, n)$  is shown on the left panel. The  $\gamma$ -ray energies are marked for the transitions from the decay of the isomeric and ground states of  $^{143}\text{Sm}$ . In the overlaid figure, the upper spectrum was taken 1 minute after an irradiation (red) and the lower one after 9 minutes (blue). On the right panel, exponential decrease in the rate of  $^{143}\text{Sm}$  identified with the strongest line at 1057 keV is shown which was used for the half-life determination.

unique transition at 754 keV and the  $^{144}\text{Sm}(\gamma, n)^{143}\text{Sm}$  with the transitions above 1000 keV. On the right panel, exponential decay of the ground state of  $^{143}\text{Sm}$  is shown. The measured half-life is  $8.83 \pm 0.08$  min which is in agreement with the recent literature value  $8.75 \pm 0.08$  min given in [ENDSF]. The decay properties of the daughter nuclei stemming from the  $^{144}\text{Sm}(\gamma, n)$  reaction are given in detail in Table. D.1 of Appendix D.

### 5.4.1 Comparison with previous experiments

The photoneutron cross sections of the samarium isotopes have been measured by Carlos et al. [Carl74] using the positron annihilation technique at Saclay. In particular, Carlos et al. had presented a study of the transition from spherical to deformed isotopes in the samarium region. The partial photoneutron cross sections -  $[\sigma(\gamma, n) + \sigma(\gamma, np)]$  and  $\sigma(\gamma, 2n)$  of  $^{144}\text{Sm}$  are given in Fig. 2 of [Carl74].

The isomeric state excitations have been investigated for several  $N=82$  shell nuclei by Mazur et al. [Mazu95] in the energy range 8-18 MeV. The experiments were carried out via the activation technique using bremsstrahlung beams from the M-30 microtron facility at Uzhgorod (Ukraine). The cross sections were calculated using the Penfold-Leiss method [Penf59], see Fig. 1, [Mazu95]. Mazur et al. have also measured the isomeric yield ratio  $\eta = \frac{Y_m}{Y_m + Y_g}$  [Vans81] as a function of endpoint energy for the  $^{144}\text{Sm}(\gamma, n)^{143g, m}\text{Sm}$  reaction.

The experimental cross sections for the  $^{144}\text{Sm}(\gamma, n)^{143}\text{Sm}$  [Carl74] and  $^{144}\text{Sm}(\gamma, n)^{143m}\text{Sm}$  [Mazu95] are shown in the right panel of Fig. 5.11. The cross sections calculated using the TALYS and NON-SMOKER codes are also shown (left panel, Fig. 5.11).

At ELBE, we determined the activation yield for the  $^{144}\text{Sm}(\gamma, n)$  reaction using the method described in Chapter 3 (see Sect. 3.2). The samarium targets were irradiated in the photoactivation site (see Fig. 3.2, Sect. 3.3). The activation yield  $Y_{\text{act}}$  is normalized to the photon fluence  $\Phi_\gamma$  at  $E_\gamma^X = 7.288$  MeV.

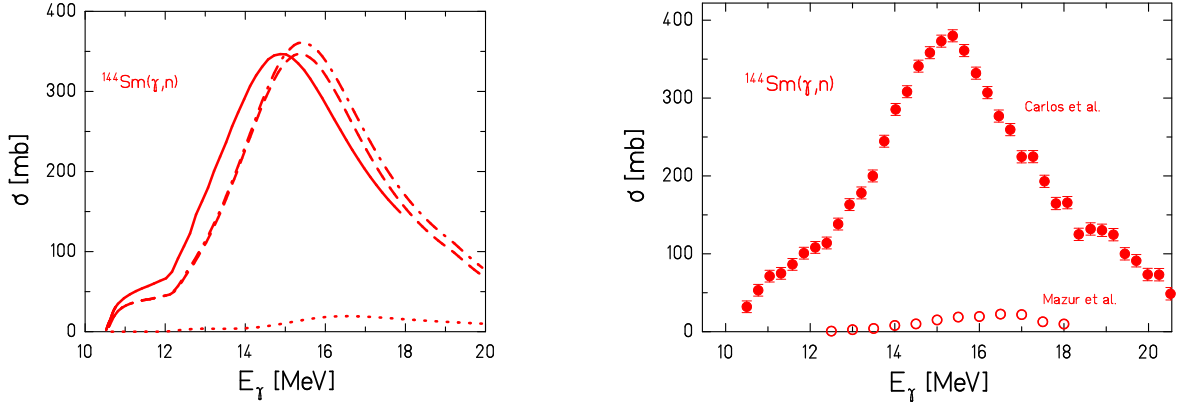


Figure 5.11: Photoneutron cross sections for  $^{144}\text{Sm}$  from model calculations (left) and previous experiments (right). The statistical model calculations using the NON-SMOKER code (full line) give the total photoneutron cross sections. The TALYS code also calculates the separate components from the activation of  $^{144}\text{Sm}$  to the ground state of  $^{143}\text{Sm}$  (dashed line), to the isomeric state  $^{143m}\text{Sm}$  (dotted line) and the total (dash-dotted line) cross sections. The experimental data on the right are from Carlos et al. [Carl74] ( $^{144}\text{Sm}(\gamma, n)^{143}\text{Sm}$ , circles) and Mazur et al. [Mazu95] ( $^{144}\text{Sm}(\gamma, n)^{143m}\text{Sm}$ , open circles) respectively.

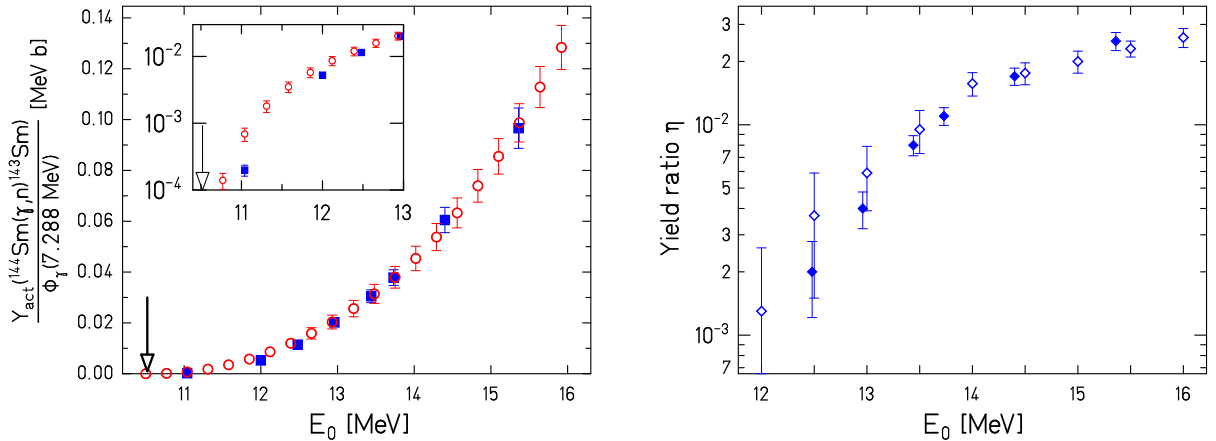


Figure 5.12: On the left panel, the experimental activation yield (blue squares) for the  $^{144}\text{Sm}(\gamma, n)^{143}\text{Sm}$  reaction normalized to the photon fluence is compared to the yield calculated using cross sections measured by Carlos et al. (red open circles). The cross sections measured by Carlos et al. have been rescaled by a factor of 0.8; based on the recommendations by Berman et al. [Berm87] for the measurements at Saclay (see text for details). The downward arrow denotes the neutron emission threshold. The yield ratio  $\eta = \frac{Y_m}{Y_m + Y_g}$  measured in the ELBE experiment (diamonds) is compared to the yield ratio given by Mazur et al. (open diamonds) as shown on the right panel.

The experimental activation yield for the  $^{144}\text{Sm}(\gamma, n)^{143}\text{Sm}$  reaction ( $Y_g$ ) normalized to the photon fluence is compared to the calculated yield using the cross sections by Carlos et al. as shown on the right panel of Fig. 5.12. The cross section data from Carlos et al. had to be corrected for two effects:

1. The target used by [Carl74] had a contamination of 11.4 % of other Sm-isotopes. We

have subtracted the possible contamination using earlier data obtained with natural-Sm at the same laboratory [Berg69] at nearly the same photon energies.

- As shown in a precision experiment by Berman et al. [Berm87], the cross sections measured at Saclay are too large by 20% in quite a few cases. For this particular case, we applied an additional correction factor of 0.8.

The corrected cross sections were then used to calculate the activation yield which compares to the ELBE experimental yield as in Fig. 5.12.

In addition, we determined the activation yield for the population of the isomeric state ( $Y_m$ ) using the same method described in Sect. 3.2. With known  $Y_g$  and  $Y_m$ , the yield ratio  $\eta = \frac{Y_m}{Y_m + Y_g}$  was determined which is shown in the right panel of Fig. 5.12. The yield ratio given by Mazur et al. is also shown. The experimental yield ratio from ELBE is in good agreement to the data from Mazur et al.

### 5.4.2 Comparison with model calculations

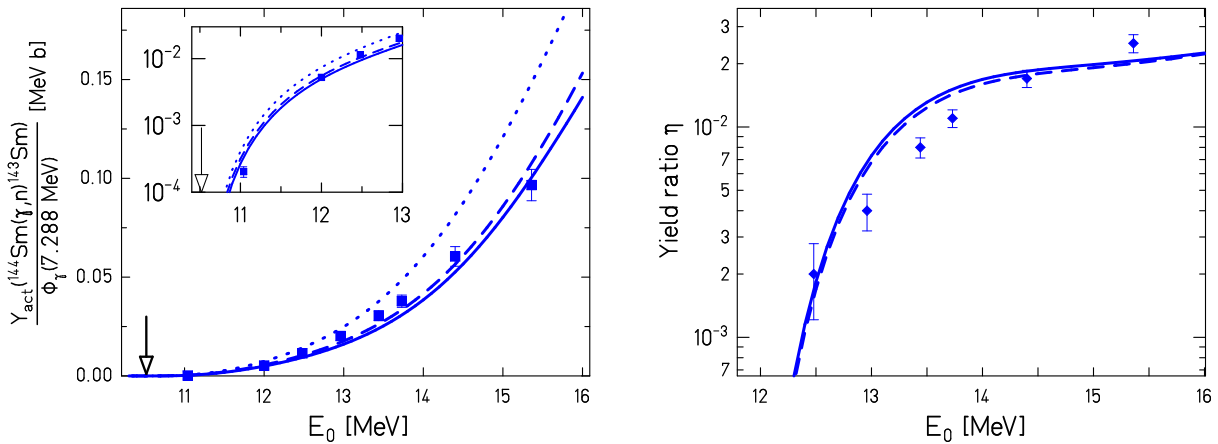


Figure 5.13: Experimental activation yield normalized to the photon fluence for the  $^{144}\text{Sm}(\gamma, n)^{143}\text{Sm}$  reaction compared to theoretical model calculations. The experimental data are denoted by squares with a downward arrow denoting the neutron emission threshold. The dashed and dotted lines denote yield calculations using cross sections from TALYS and NON-SMOKER codes respectively. The solid line represents a TALYS calculation with modified inputs, see text.

In Fig. 5.13, the  $^{144}\text{Sm}(\gamma, n)^{143}\text{Sm}$  reaction yield normalized to the photon fluence is compared to the simulated yield calculated using cross sections predicted by Hauser-Feshbach models. The experimental yield agrees to the simulated yield integrals using cross sections predicted by the default inputs to TALYS (agrees within 20%) and NON-SMOKER (agrees within a factor of 2) models. The TALYS code was modified with  $\gamma$ -ray strength functions derived on the basis of the discussion given in Sect. 5.2.3. The following resonance parameters were used:  $E_1 = 14.84$  MeV,  $\sigma_1 = 356.6$  mb and  $\Gamma_1 = 3.74$  MeV. The yield curve created using the cross sections resulting from modified inputs is also shown in Fig. 5.13.

On the right panel of Fig. 5.13, the yield ratio measured at ELBE is compared to the yield ratio calculated using cross sections predicted by the TALYS code with default and modified inputs. The cross sections for the population of the isomeric state are not given in the tables by Rauscher et al. and hence it was not possible to calculate a yield ratio.

## 5.5 Activation yield for the $^{144}\text{Sm}(\gamma, p)$ and $^{144}\text{Sm}(\gamma, \alpha)$ reactions

This section is dedicated to the activation yield measured for photon-induced reactions in  $^{144}\text{Sm}$  with charged particles in the exit channel. The  $^{144}\text{Sm}(\gamma, p)$  and  $^{144}\text{Sm}(\gamma, \alpha)$  were measured for the first time at ELBE at astrophysically relevant energies. The cross section predictions for the  $(\gamma, p)$  and  $(\gamma, \alpha)$  reactions by the default TALYS and NON-SMOKER model codes are given in Fig. 5.14. The decay properties of the daughter nuclei stemming from the respective photodisintegration reactions on  $^{144}\text{Sm}$  are given in Table. D.1 of Appendix D.

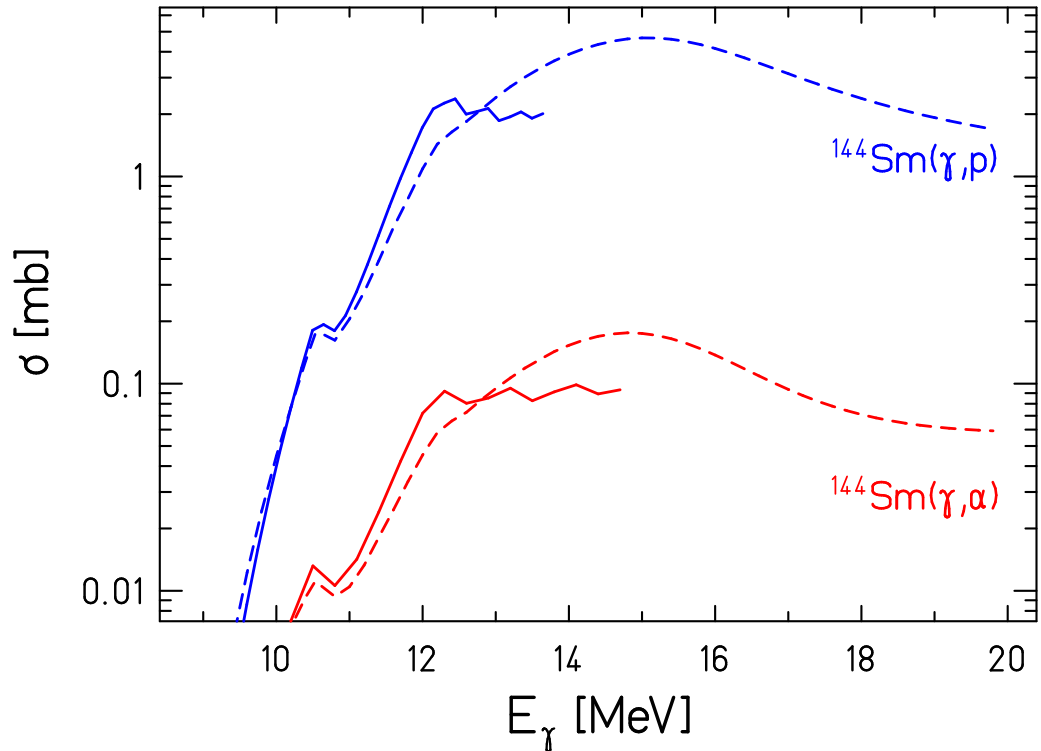


Figure 5.14:  $^{144}\text{Sm}(\gamma, p)$  and  $^{144}\text{Sm}(\gamma, \alpha)$  cross sections from model calculations. TALYS and NON-SMOKER predictions are shown with dashed and solid lines respectively.

In the photoactivation of  $^{144}\text{Sm}$ ,  $(\gamma, n)$  and  $(\gamma, p)$  cannot be distinguished at high energies above the neutron separation energy ( $S_n=10.5$  MeV) since the  $(\gamma, n)$  daughter nucleus decays very quickly to the  $(\gamma, p)$  daughter nucleus. Therefore, to measure the pure  $(\gamma, p)$  reactions, we used bremsstrahlung energies sufficiently below 10.5 MeV. The rather small  $(\gamma, p)$  cross sections at these low energies ( $<0.1$  mb, see Fig. 5.14) results in a decay spectrum with weak counting statistics. Therefore, the decay measurements were performed under optimized background conditions in the underground laboratory "Felsenkeller" (see Sect. 4.2.3).

The decay spectrum of a  $\text{Sm}_2\text{O}_3$  target irradiated at an endpoint energy of 15.0 MeV is given in Fig. 5.15. The target was placed on top of the 30% HPGe detector at Felsenkeller. The target specifications were discussed in Sect. 4.4. The  $^{144}\text{Sm}(\gamma, p)$  reaction is identified by the transition at 742 keV from  $^{143}\text{Pm}$  decay (EC) with a half life of 265 days, see figure. The other peaks in the spectrum are stemming from the contamination reactions in the other isotopes of samarium (e.g.,  $^{154}\text{Sm}(\gamma, n)$ ).

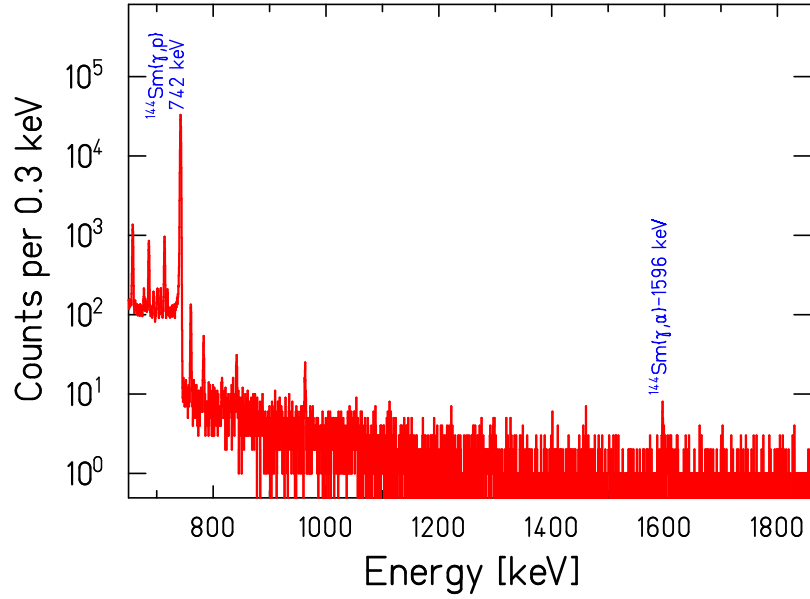


Figure 5.15: Spectrum of an irradiated  $\text{Sm}_2\text{O}_3$  target. The peaks originating from the  $^{144}\text{Sm}(\gamma, p)$  and  $^{144}\text{Sm}(\gamma, \alpha)$  reactions are marked. The target was placed on top of the 30% HPGe detector at the underground laboratory "Felsenkeller". The other peaks are from the contamination reactions like  $^{154}\text{Sm}(\gamma, n)$  etc. The target was irradiated at a bremsstrahlung endpoint energy of 15.0 MeV and the spectrum shown here was recorded for a period of 1 day.

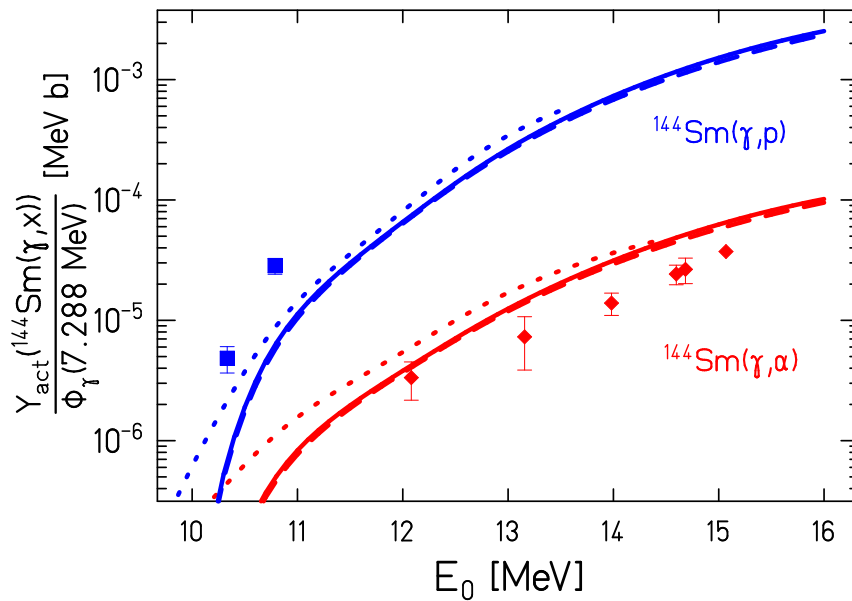


Figure 5.16: Absolute activation yield as a function of endpoint energy for photodisintegration reactions in  $^{144}\text{Sm}$ . The yields for  $^{144}\text{Sm}(\gamma, p)$  (blue squares) and  $^{144}\text{Sm}(\gamma, \alpha)$  (red diamonds) are shown. The dashed and dotted lines denote yield calculations using cross sections from the TALYS and NON-SMOKER codes with default inputs whereas the solid line represents a TALYS calculation with modified inputs, see text.



The  $^{144}\text{Sm}(\gamma, \alpha)$  reaction was identified by the transition at 1596 keV from  $^{140}\text{Pr}$  which is the short-lived daughter of the  $(\gamma, \alpha)$  reaction product  $^{140}\text{Nd}$ . For  $^{144}\text{Sm}$  the  $Q(\alpha)$  value is -0.145 MeV. Half-lives for  $^{140}\text{Nd}$  and  $^{140}\text{Pr}$  are 3.37 days and 3.4 minutes respectively. In the spectrum shown in Fig. 5.15, the 1596 keV transition is also marked.

The activation yields for the  $^{144}\text{Sm}(\gamma, p)$  and  $^{144}\text{Sm}(\gamma, \alpha)$  reactions compared to the simulated yields using cross sections predicted by TALYS and NON-SMOKER are shown in Fig. 5.16. The predictions given by the TALYS code with modified inputs to the  $\gamma$ -ray strength function (see Sect. 5.4.2) are also shown. The sensitivity of the theoretical predictions to the nuclear physics inputs will be discussed in detail in the following chapter.

The uncertainties in the experimental yield shown in Fig. 5.16 are mainly the statistical uncertainties arising from the peak fit for the rather low-statistics peaks (10-35%). For a detailed discussion on the fit routines for such low-statistics peaks, see Fig. 4.2, Sect. 4.1.1. The statistical uncertainty from the calculation of the full-energy peak efficiency is very small (0.2-0.5%). The systematic uncertainties arise from the photon emission probabilities for the decays stemming from the  $(\gamma, p)$  (6%) and  $(\gamma, \alpha)$  (8%) reactions (see Table. D.1, Appendix D) and from the full-energy peak efficiency calculations (2%). The systematic errors are not shown in Fig. 5.16.

## 5.6 Activation yield for the $^{92}\text{Mo}(\gamma, \alpha)$ reaction

As discussed in Sect. 2.4, Mo and Ru isotopes are underproduced in the network calculations and need particular attention in the experimental frame. At ELBE, the photon induced reactions of  $^{92}\text{Mo}$  isotope are studied to test if the reaction rates that are part of the nuclear physics input to the network calculations are correct. The experimental results from  $^{92}\text{Mo}(\gamma, n/p)$  reactions are given in the thesis work of [Erha09]. The results of the  $^{92}\text{Mo}(\gamma, \alpha)$  experiment will be discussed in this section.

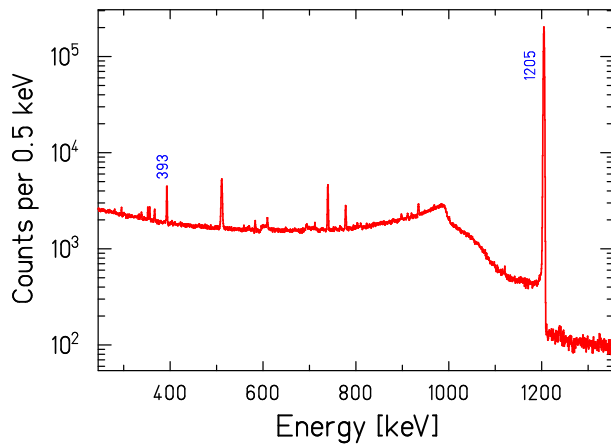


Figure 5.17: Spectrum of an irradiated  $^{92}\text{Mo}$  target. The peaks stemming from the decays following the  $^{92}\text{Mo}(\gamma, p)$  (1205 keV) and  $^{92}\text{Mo}(\gamma, \alpha)$  (393 keV) reactions are marked. The spectra shown here was measured using a 90% HPGe detector for about 6 days.

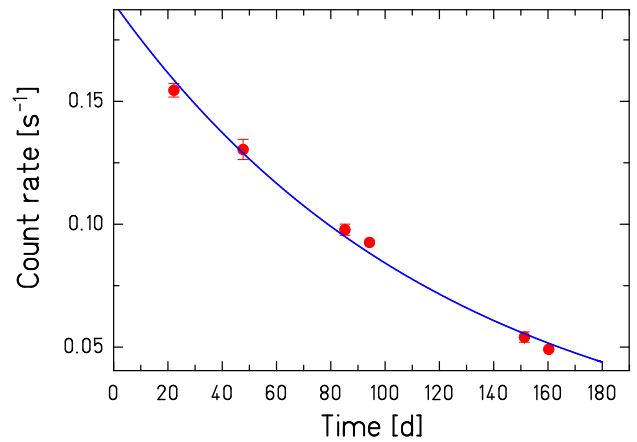


Figure 5.18: Half-life calculations by studying the  $^{92}\text{Mo}(\gamma, \alpha)$  photodisintegration. The 393 keV peak stemming from the  $^{88}\text{Zr}$  decay was studied periodically and the half-life was calculated from an exponential fit to the descending count rate.

At the photoactivation site, natural samples of molybdenum (mass 1 - 3 g, disc diameter 20 mm) were irradiated together with the Au samples for flux normalization. The decay of the

irradiated Mo targets were studied at the low-level counting setup discussed in Sect. 4.2.1. The  $^{92}\text{Mo}(\gamma, \alpha)$  reaction is identified by the transition at 393 keV from  $^{88}\text{Zr}$  decay (EC) with a half life of 83.4 days. A sample spectrum is given in Fig. 5.17. The peaks stemming from the  $^{92}\text{Mo}(\gamma, \alpha)^{88}\text{Zr}$  (393 keV) and  $^{92}\text{Mo}(\gamma, p)^{91}\text{Nb}$  (1205 keV) are marked. By measuring the exponential decay of  $^{88}\text{Zr}$  (see Fig. 5.18), we determined the half-life to be  $85.1 \pm 2.1$  days which is in good agreement with the literature value  $83.4 \pm 0.3$  days [ENDSF]. The decay properties of the daughter nuclei stemming from  $^{92}\text{Mo}(\gamma, \alpha)$  reaction are given in Table. D.1 of Appendix D.

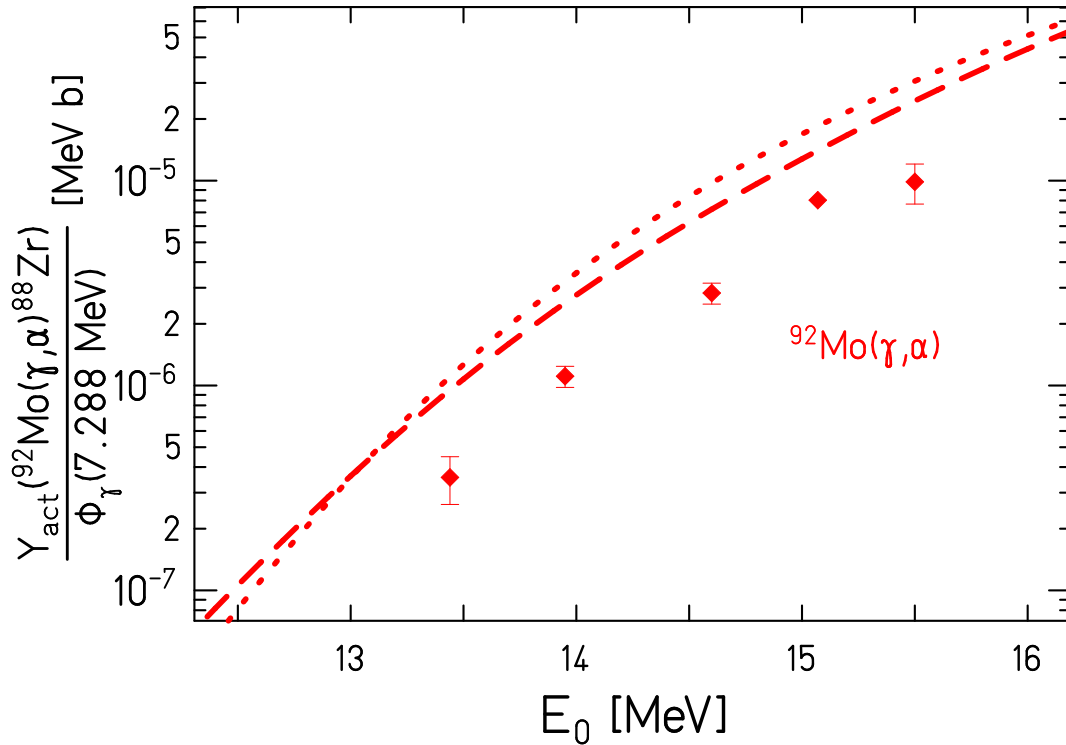


Figure 5.19: Absolute activation yield for the  $^{92}\text{Mo}(\gamma, \alpha)$  reaction (diamonds) are shown. The dashed and dotted lines denote yield calculations using cross sections from TALYS and NON-SMOKER codes with default inputs.

The activation yield measured for the  $^{92}\text{Mo}(\gamma, \alpha)$  reaction is given in Fig. 5.19. The simulated yields using cross sections predicted by the default TALYS and NON-SMOKER models are also shown. The measured activation yields for  $(\gamma, n)$  and  $(\gamma, p)$  given by Erhard et al [Erha06a, Erha06b] and the  $(\gamma, \alpha)$  results given here indicate that the underproduction of Mo in the p-process nucleosynthesis is likely *not* due to wrong photodisintegration rates in the theoretical calculations (see also: [Nair08c]).

The uncertainty in the experimental yield shown in Fig. 5.19 is mainly the statistical uncertainty arising from the peak fit for the rather low-statistics peaks (4-26%), see Sect. 4.1.1. The systematic (1.5%) and statistical (0.2-0.5%) uncertainties from the calculation of full-energy peak efficiency is very small. An overview of the overall uncertainties entering into the experimental yield calculation is provided in the next section.

## 5.7 Statistical and systematic uncertainties

In this section, a brief overview of the uncertainties involved in the data analysis of the photodisintegration experiments presented in this thesis are given. In the following discussion, the statistical and systematic uncertainties will be referred as  $\Delta_{stat}$  and  $\Delta_{sys}$ .

The uncertainties in counting experiments due to the poisson distribution of the observed decay processes are named as *statistical uncertainties*. These can be reduced by several individual measurements. *Systematic uncertainties* are reproducible inaccuracies that are typically consistent in the same direction and are often due to a problem which persists throughout the entire experiment. An overview of how the statistical and systematic uncertainties contribute to the total uncertainty in the photoactivation experiments is given in Table. 5.1.

In the activation yield determination procedure discussed in Chapter 3 (see Sect. 3.2), the major uncertainties are from the detection efficiency, half-life, photon emission probability and from the determination of peak areas in the measured decay spectra.

As discussed in Sect. 4.2.1, the statistical uncertainty in the full-energy peak efficiency determination for the detectors at the *low-level counting setup* are very small in the order of 0.2-0.5%. The systematic uncertainties are mostly from the activity given in the source certificates and amount to about 0.6-1.5%. The statistical uncertainty in the measured full-energy peak efficiency for the detectors at the *photon scattering site* is about 0.5-2% and systematic uncertainties are 0.6-1.5%.

Quantity	$\Delta_{stat} / \%$	$\Delta_{sys} / \%$
full-energy peak efficiency <sup>a</sup>	0.2-0.5	0.6-1.5
full-energy peak efficiency <sup>b</sup>	0.5-2	0.6-1.5
$\gamma$ -emission probability		5-13
half-lives		0.2-2.6
target mass	0.2-1	
summing correction	0.6-1.5	
peak area	0.5-33	
photon fluence	0.5-2	7.8

Table 5.1: The uncertainties in the activation experiments discussed in the scope of this thesis. The statistical ( $\Delta_{stat}$ ) and systematic ( $\Delta_{sys}$ ) uncertainties are given, see text for details. The superscripts *a* and *b* distinguish the full-energy peak efficiencies at the *low-level counting setup* and *photon scattering site* respectively.

The uncertainty contributions stemming from half-lives, target mass and summing corrections are very small and are in the order of a few percent only (see Table. 5.1). The statistical uncertainty from the peak area determination falls into a wide spectrum, depending on the counting statistics. A more detailed discussion of the peak fit routine was given in Sect. 4.1.1. For  $\gamma$ -peaks with very low statistics, the uncertainties can be quite large and are given in Table. 5.1.

The most significant uncertainty in the reaction yield is from the photon fluence determination using photon scattering from  $^{11}\text{B}$  (see Sect. 3.4.2). The statistical uncertainties from the  $\gamma$ -counting in this case are quite small and in the order of 0.5-2%. The systematic uncertainty in the extrapolation of the full-energy peak efficiency is about 5% in the energy range of the observed transitions in  $^{11}\text{B}$ . The systematic deviation of the measured photon fluence from the

simulated fluence is about 6% (see Fig. 3.9, Sect. 3.4.2). While adding up quadratically, the total systematic uncertainty in the fluence determination procedure amounts to 7.8%.

The statistical uncertainties in the activation yield for the photon induced reactions in  $^{144}\text{Sm}$  and  $^{92}\text{Mo}$  depends very much on the  $\gamma$ -counting statistics and are given along with the results at the end of respective sections (see Sect. 5.4, Sect. 5.5 and Sect. 5.6). The systematic uncertainty is mainly from the photon fluence determination. The samarium/molybdenum targets were irradiated at the *photoactivation site* discussed in Sect. 3.3.1 where the photon fluence is given by the ratio of the measured  $^{197}\text{Au}(\gamma,n)$  activation yield and the calculated activation yield using the known photoneutron cross sections from  $^{197}\text{Au}$  and a simulated thick target bremsstrahlung spectrum using the code MCNP (see Sect 3.2). The activation yield of  $^{197}\text{Au}(\gamma,n)$  was determined at the *photon scattering site* (see Fig. 3.2) to verify the photoneutron cross sections to be used for the photon fluence determination. At the *photon scattering site*, the photon flux was determined from the scattering of  $^{11}\text{B}$  (see Sect. 3.4). The systematic uncertainties in the photon fluence at both the target sites are, in principle, identical and amount to about 7.8%.

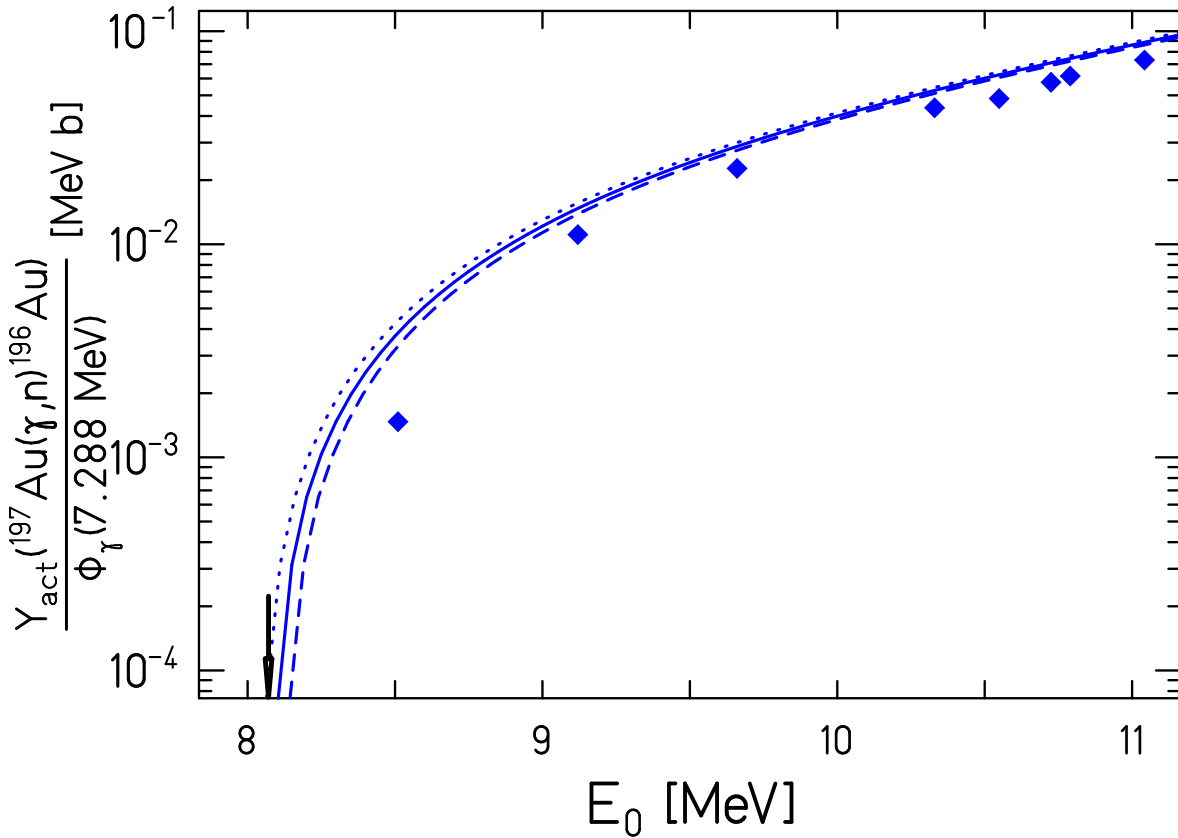


Figure 5.20: Experimental activation yield normalized to the photon fluence for the  $^{197}\text{Au}(\gamma,n)$  reaction close to threshold compared to the TALYS model calculations with default inputs. The dashed and dotted lines denote yield calculations with a deviation of  $\pm 40$  keV in the endpoint energy. The experimental data are denoted by diamond symbols with a downward arrow denoting the neutron emission threshold. At 8.50 MeV, which is about 4.29 MeV above the threshold, the 40 keV deviation in the endpoint energy gives rise to about 20% difference in the activation yield curves.

As pointed out earlier in Chapter 3, an essential requisite of the photoactivation experiment is the precision measurement of the bremsstrahlung beam energy. As discussed in Sect. 3.5.2,

the endpoint energy of the bremsstrahlung distribution is determined by measuring the proton energy from the photodisintegration of the deuteron. The measured spectra are fitted to a simulated proton spectrum for beam energy determination. The statistical uncertainties stemming from the fit amount to about 2-8 keV for the range of energies discussed in the scope of this thesis. The systematic deviation of the experimental proton spectrum from the simulated one is 40 keV. This deviation plays a significant role only for endpoint energies close-above the neutron/proton-emission threshold of the photodisintegration reaction under consideration. An example depicting the case of the  $^{197}\text{Au}(\gamma, n)$  reaction yield is shown in Fig 5.20. At 8.50 MeV (4.29 MeV above the neutron emission threshold), the 40 keV deviation in the endpoint energy gives rise to a significant effect of 20% on the activation yield calculated using cross sections from TALYS. At higher energies, the effect becomes smaller. For the  $^{197}\text{Au}(\gamma, n)$  and  $^{144}\text{Sm}(\gamma, n)$  experiments presented in this work, the close-threshold experimental data are thus prone to larger uncertainties than the high-energy data.



# Chapter 6

## Discussion

For simulating the photoactivation yields discussed in this thesis, we used the TALYS and NON-SMOKER codes which are based on the Hauser-Feshbach formalism. The cross sections given by the NON-SMOKER code were adopted from the database of [Raus04] and the predictions by TALYS were from the recent version of the code (TALYS1.0). The difference in predictions between the two codes are mostly linked to the nuclear physics input involved, e. g., optical-model potentials, nuclear level densities and  $\gamma$ -ray strength functions. In this chapter, a study of the sensitivity of the theoretical models to the various input parameters are presented.

### 6.1 Sensitivity of the statistical model calculations to nuclear physics input

Both the TALYS and NON-SMOKER codes use different nuclear physics inputs such as  $\gamma$ -ray strength functions, optical model potentials and nuclear level densities. As already mentioned in Sect. 5.1.1, the NON-SMOKER code uses the neutron optical-model potential by Jeukenne et al. [Jeuk77b] and the  $\gamma$ -ray strength function is based on a description by Thielemann and Arnould [Thie83]. The nuclear level densities are based on a global parametrization by Rauscher et al. [Raus97]. The experimental activation yield for all the photon induced reactions discussed in this thesis have been compared to the predicted yield from NON-SMOKER code. The calculations were based on the default nuclear physics inputs to the code.

In contrast to the NON-SMOKER model, the TALYS code allows the user to modify each single input entering the calculations. The default option of the code uses the neutron optical-model potential parameterizations by Koning and Delaroche [Koni03] and the  $\gamma$ -ray strength functions using the Brink-Axel model [Brin57, Axel62]. The nuclear level density model is the constant-temperature model with a Fermi-Gas model approach for higher energies [Eric60]. The different options and keywords of the TALYS code inputs are summarized in Table. 6.1. In the next sections, the impact of choosing different nuclear physics inputs to the TALYS code is discussed in detail.

#### 6.1.1 The $\gamma$ -ray strength functions

In the TALYS code, 4 different models for the  $\gamma$ -ray strength functions are included. The standard is the so-called Brink-Axel option [Brin57], in which a standard Lorentzian is used to describe the giant dipole resonance shape. At present, the Brink-Axel option is used for all transition types other than E1. For E1 radiation, the default option used in TALYS is the

Notation	Model / Parametrization	TALYS keyword
PSF0	Brink-Axel / This work	strength 2 + parametr.
PSF1	Kopecky-Uhl	strength 1
PSF2	Brink-Axel / Dietrich-Berman	strength 2 (standard)
PSF3	Hartree-Fock-BCS	strength 3
PSF4	Hartree-Fock-Bogolyubov	strength 4
OMP1	Koning-Delaroche	alphaomp 1 (standard)
OMP2	McFadden-Satchler	alphaomp 2
OMP3	Jeukenne-Lejeune-Mahaux	jlmomp y
NLD1	Constant temperature + Fermi gas model	ldmodel 1 (standard)
NLD2	Back-shifted Fermi gas model	ldmodel 2
NLD3	Generalized superfluid model + Fermi gas model	ldmodel 3
NLD4	Microscopic level density: Goriely + Fermi gas model	ldmodel 4
NLD5	Constant temperature + Fermi gas model	ldmodel 5

Table 6.1: The different options used for the photon strength functions (PSF), optical-model potentials (OMP) and nuclear level densities (NLD) in the TALYS model code. The second column denotes the theoretical models used in the calculations and the last column is the TALYS keyword to initiate a calculation with the respective model.

generalized Lorentzian form of Kopecky and Uhl [Kope90]. The notations for different models as used in TALYS1.0 are given in Table. 6.1.

The GDR parameters for the individual nuclides are stored in the nuclear structure database of TALYS for E1 transitions. They originate from the Beijing GDR compilation, as present in the RIPL database [Diet88]. For each isotope, the corresponding  $Z$ ,  $A$ , energy  $E_0$  (MeV), strength  $\sigma_0$  (mb) and width of the GDR  $\Gamma_0$  (MeV) are stored along with the nuclear symbol. In case when there is more than one resonance, a second set of Lorentzian parameters is used. For all transitions other than E1, the resonance parameters are from the compilation by Kopecky [RIPL-2]. The resonance parameterizations used for transitions other than E1 or in case when there is no tabulated data for E1, are given in the TALYS1.0 user's manual in detail. For E1 radiation, two microscopic options also exist in TALYS. These are the  $\gamma$ -ray strength functions calculated by Goriely according to the Hartree-Fock BCS model and the Hartree-Fock-Bogolyubov model (see [RIPL-2] also). The notations and keywords indicating the models are given in Table. 6.1. The microscopical strength functions have not been adjusted to experimental data.

The default inputs can always be combined or overruled with user-defined input parameters. We modified the  $\gamma$ -ray strength functions for each experiment in the scope of this thesis using the parametrization given by [Jung08] (cf. Sect. 5.2.3, Chapter 5). The resonance energy  $E_k$ , cross section  $\sigma_k$  and width  $\Gamma_k$  has been modified and a new yield curve was created using the cross sections resulting from modified inputs. The resulting calculations are denoted with PSF0, see Table. 6.1.

The activation yield calculated using cross sections from TALYS predictions with different options for the  $\gamma$ -ray strength functions are compared to the experimental yields in Fig. 6.1 and Fig. 6.2. For the  $^{144}\text{Sm}(\gamma, n)^{143}\text{Sm}$  reaction yield, the simulated yield calculated using cross sections predicted by the TALYS code with the  $\gamma$ -ray strength function models PSF1 and PSF2 seem to agree within 20%. The TALYS calculations with the  $\gamma$ -ray strength function



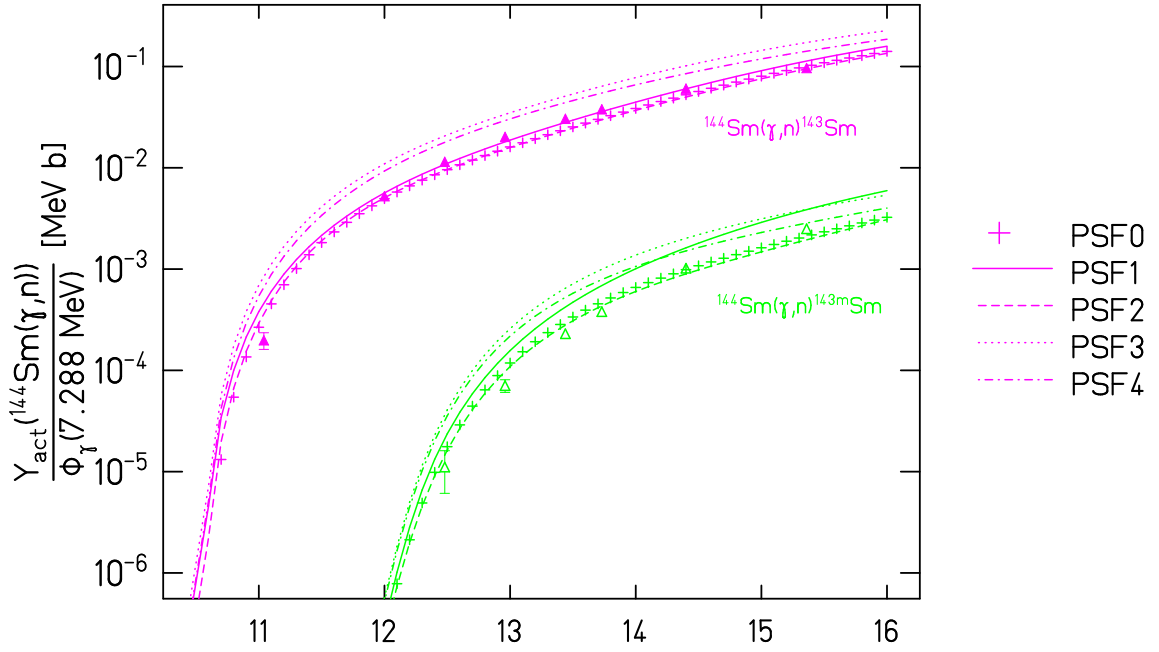


Figure 6.1: Experimental activation yield normalized to the photon fluence for the  $^{144}\text{Sm}(\gamma, n)^{143}\text{Sm}$  (triangles) and  $^{144}\text{Sm}(\gamma, n)^{143m}\text{Sm}$  (open triangles) reaction compared to TALYS model calculations with different inputs for the photon strength functions. The simulations are shown by different lines denoting different strength function models (PSF0 to PSF4) which correspond to Table. 6.1.

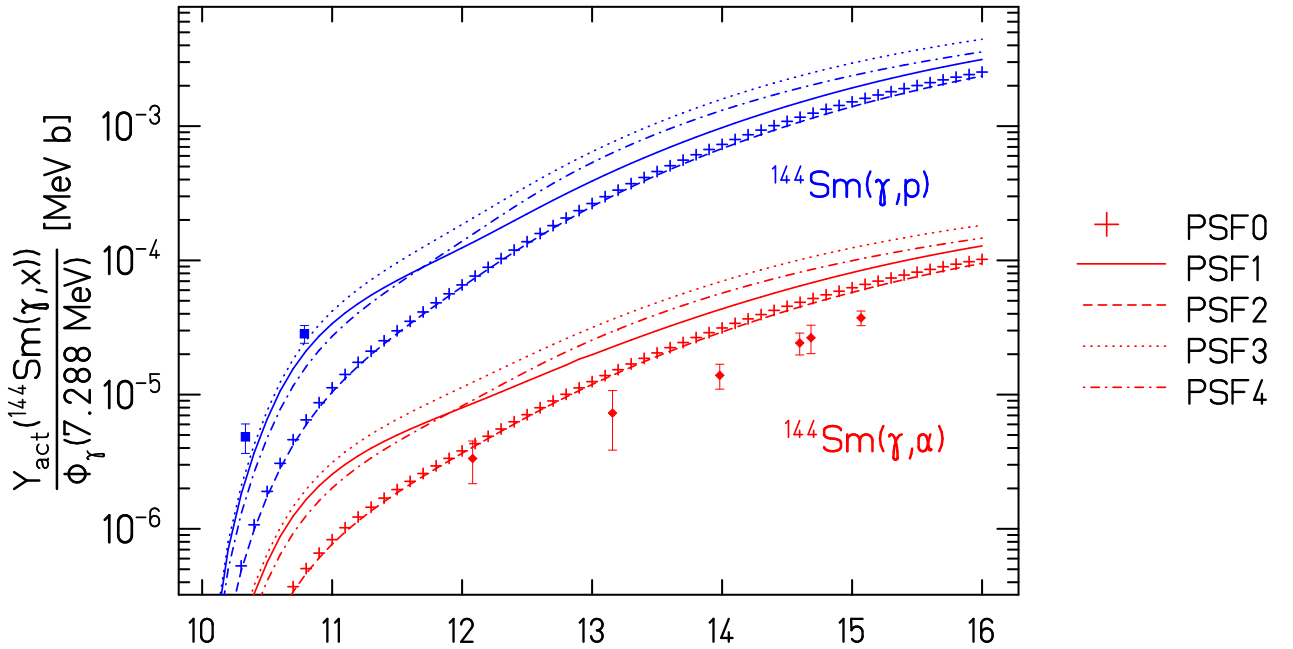


Figure 6.2: Sensitivity of the model calculations to different inputs for the photon strength functions. The absolute activation yields for  $^{144}\text{Sm}(\gamma, p)$  (squares) and  $^{144}\text{Sm}(\gamma, \alpha)$  (diamonds) are shown. The different lines correspond to the yield calculations with different inputs for the photon strength functions (PSF0 to PSF4) and correspond to the models given in Table. 6.1.

parametrization given in Sect. 5.2.3 are denoted by PSF0. The yield curve created using the microscopic strength functions (PSF3, PSF4) is found to group separately and gives higher activation yields as compared to the experimental data. For the  $^{144}\text{Sm}(\gamma, n)^{143m}\text{Sm}$  reaction yield, the simulated yield calculated using cross sections predicted using the  $\gamma$ -ray strength function model PSF1 seem to disagree from the experimental data and group with the microscopic models.

The activation yield for the  $^{144}\text{Sm}(\gamma, p)$  reaction is compared to the simulated yield as shown in Fig. 6.2. The prediction given by PSF0 is in agreement to the predictions using the model 2 (PSF2), but both deviate from the experimental data. The yield curve created using the microscopic strength functions (PSF3, PSF4) as well as the model PSF1 are different from the calculations using the strength function models 0 and 2, but these predictions are closer to the observed yields. In contrast, for the  $^{144}\text{Sm}(\gamma, \alpha)$  reaction, the simulated yields (Fig. 6.2) using microscopic strength function models as well as PSF1 deviate from the experimental data whereas the predictions using strength function models PSF0 and PSF2 are more close to the experimental yields.

### 6.1.2 Optical model potentials

The default for the optical model potentials (OMPs) used in TALYS are the local and global parameterizations of Koning and Delaroche [Koni03]. The Koning and Delaroche optical model potentials are based on smooth energy dependent forms for the potential depths with the associated geometry parameters constrained within acceptable limits around a global average. These enable one to predict basic scattering observables over a broad mass range ( $24 \leq A \leq 209$ ) and over an energy range that covers several orders of magnitude in MeV (1 keV-200 MeV). The detailed phenomenological description of the optical model potentials (OMP) for nucleon-nucleus scattering are given in the TALYS user manual. A local OMP can be constructed if there is existing experimental scattering data for a certain nucleus. In case if there is no experimental information, a built-in global optical model is automatically used which can be applied for any Z/A combination.

Besides the phenomenological OMP, a semi-microscopic nucleon-nucleus spherical optical model potential is also included in TALYS. The model description is based on [Baug01]. In the TALYS 1.0 version the so called Jeukenne-Lejeune-Mahaux (JLM) OMP calculations are performed using Bauge's microscopic optical model code [RIPL-2] as a subroutine. The JLM OMP is based on the Brückner-Hartree-Fock work of Jeukenne, Lejeune and Mahaux [Jeuk74, Jeuk76, Jeuk77a, Jeuk77b]. A detailed description of the JLM OMP model is given in the TALYS user manual. Another option in the OMP models is the alpha optical potential of McFadden and Satchler [McFa66]. The yield curve created using the three different options for the OMPs are shown in Fig. 6.3 and Fig. 6.4. For these calculations, the  $\gamma$ -ray strength functions predicted by the model PSF0 (see Table. 6.1) were used.

For the  $^{144}\text{Sm}(\gamma, n)^{143g,m}\text{Sm}$  and  $^{144}\text{Sm}(\gamma, p)^{143}\text{Pm}$  reaction yields, the simulated yields calculated using cross sections with the optical model inputs 1 and 2 (OMP1, OMP2) do not differ much from each other. In the case of  $^{144}\text{Sm}(\gamma, p)^{143}\text{Pm}$  reaction yield, the yield curve created using the semi-microscopic spherical optical model JLM is higher for endpoint energies above 12 MeV when compared to the calculations using the Koning-Delaroche and McFadden-Satchler models. For the  $^{144}\text{Sm}(\gamma, \alpha)^{140}\text{Nd}$  reaction, the simulated yields (Fig. 6.4) using the different OMPs deliver similar result towards higher energies. At the same time, we could see that the sensitivity to the OMP is not as large as to the PSF. The JLM parametrization seem to favor proton emission over neutron emission, while the alpha emission is reduced. In brief, the

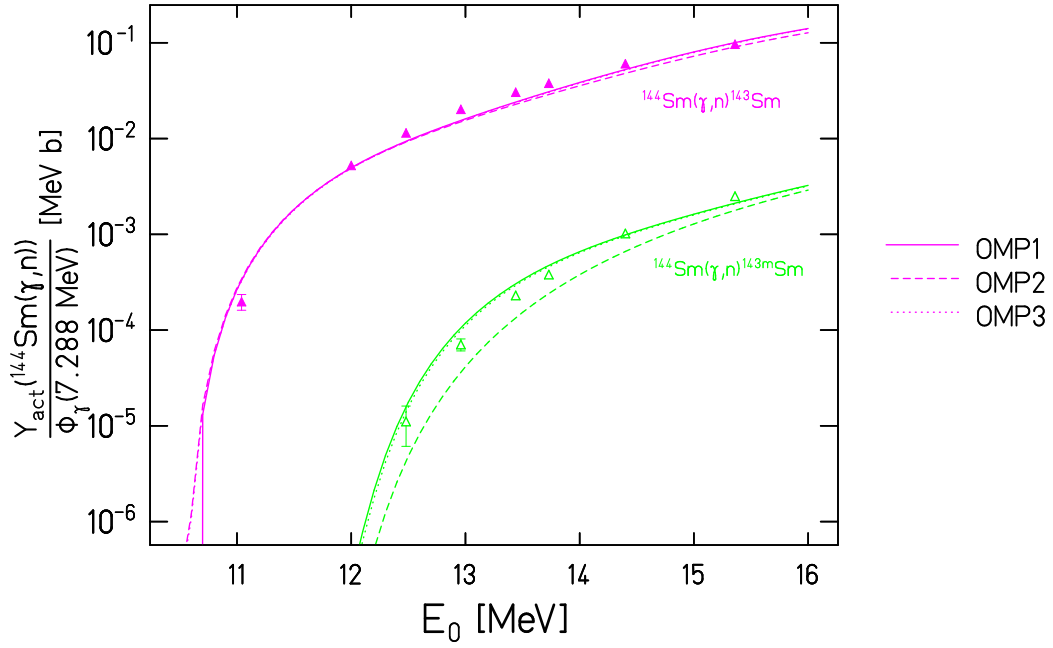


Figure 6.3: Experimental activation yield normalized to the photon fluence for the  $^{144}\text{Sm}(\gamma,n)^{143}\text{Sm}$  (triangles) and  $^{144}\text{Sm}(\gamma,n)^{143m}\text{Sm}$  (open triangles) reactions compared to TALYS model calculations with different inputs for the optical model potentials. The simulated yields are shown by different lines denoting calculations with different optical model potentials (OMP1 to OMP3) which correspond to the models given in Table. 6.1.

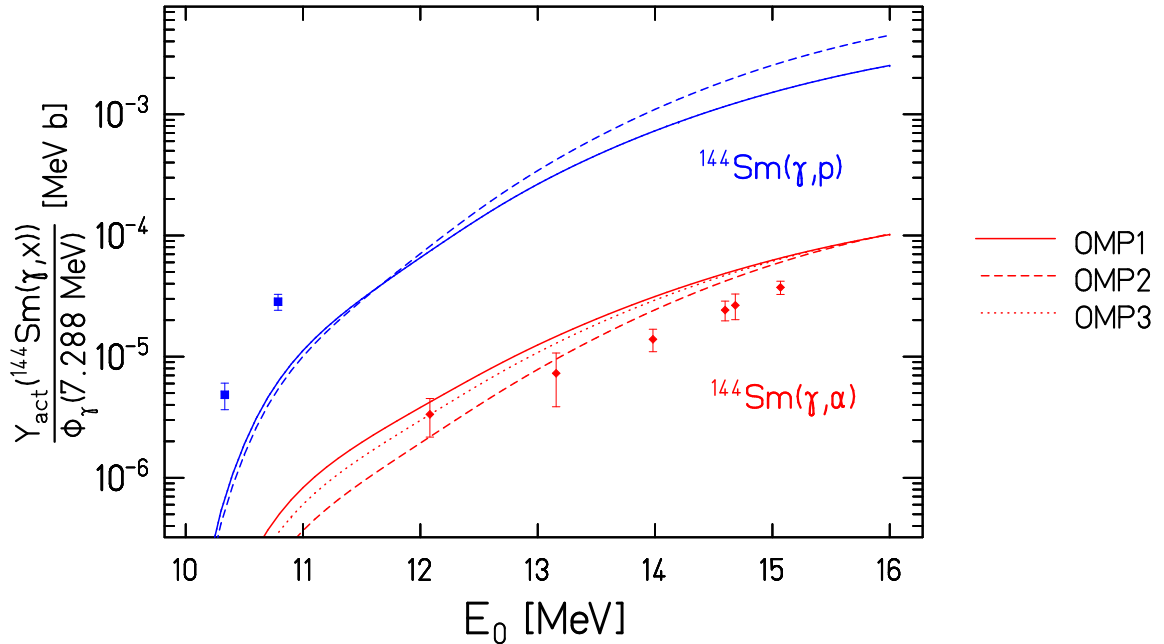


Figure 6.4: Absolute activation yields for  $^{144}\text{Sm}(\gamma,p)^{143}\text{Pm}$  (squares) and  $^{144}\text{Sm}(\gamma,\alpha)^{140}\text{Nd}$  (diamonds) normalized to the photon fluence are compared to simulated yields with different inputs for the optical model potentials. The theoretical calculations are shown by different lines which correspond to the OMP models (OMP1, OMP2 and OMP3) given in Table. 6.1.

influence of the alpha-nucleus potential on the activation yield is below a factor of 2.

### 6.1.3 Nuclear level densities

In TALYS 1.0, several models are implemented for the nuclear level densities which range from phenomenological analytical expressions to tabulated ones derived from microscopic models. Different level densities are calculated as a function of the excitation energy, spin, parity and fission barrier. The simplest and the standard model used in TALYS (NLD1) is the constant-temperature model with a Fermi-Gas model (FGM) approach for higher energies. It is based on the assumption that the single particle states which construct the excited levels of the nucleus are equally spaced, and that collective levels are absent. The other two options for the level density models are the Back-shifted Fermi gas model (NLD2) and the generalized superfluid model (NLD3). The models and the corresponding identifier keywords are given in Table. 6.1.

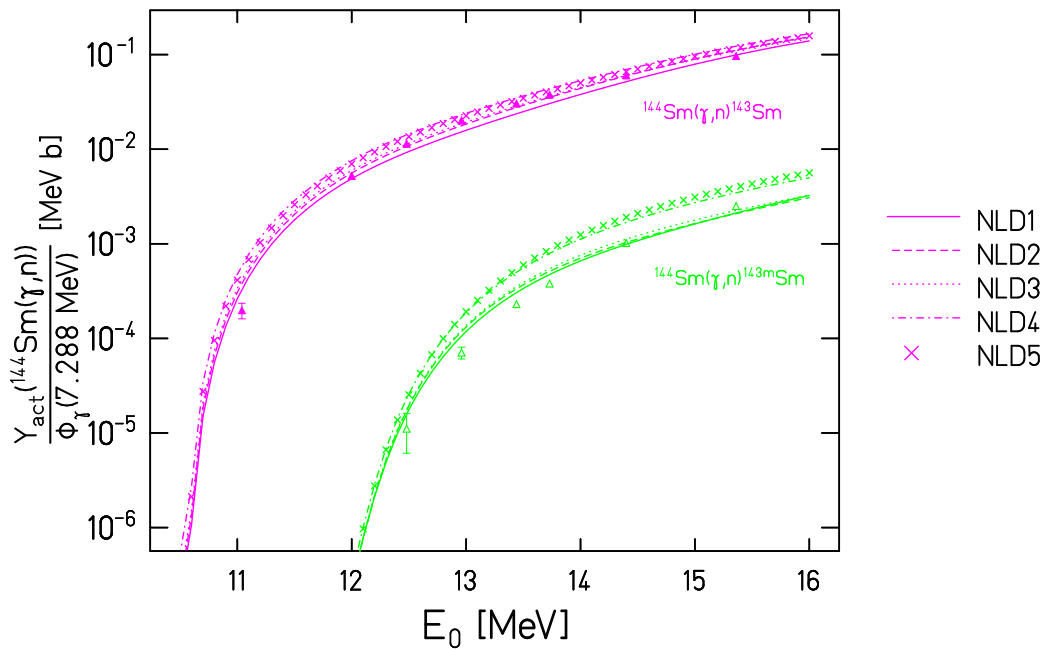


Figure 6.5: Experimental activation yield normalized to the photon fluence for the  $^{144}\text{Sm}(\gamma,n)^{143}\text{Sm}$  (triangles) and  $^{144}\text{Sm}(\gamma,n)^{143m}\text{Sm}$  (open triangles) are compared to the simulated yield curves with different inputs to the nuclear level densities. The calculated yields are shown by lines corresponding to the level density models 1 to 4 (NLD1 to NLD4), see Table. 6.1 also. The calculations using the level density model 5 (NLD5) is shown with cross symbols.

The microscopic approaches to the level density models are also included in TALYS1.0. The level densities from S. Goriely calculated on the basis of Hartree-Fock calculations [Gori01] are implemented with the keyword `ldmodel 4` (NLD4). Besides this, new energy-, spin- and parity-dependent nuclear level densities based on the microscopic combinatorial model proposed by Hilaire and Goriely [Hila06] are also included. This combinatorial model is a detailed microscopic calculation of the intrinsic state density and collective enhancement. The nuclear structure properties determined within the deformed Skyrme-Hartree-Fock-Bogolyubov framework are used for the calculations. These level densities are included with the identifier keyword `ldmodel 5` (NLD5, see Table. 6.1).

The experimental activation yield for the photodisintegration reactions in  $^{144}\text{Sm}$  compared

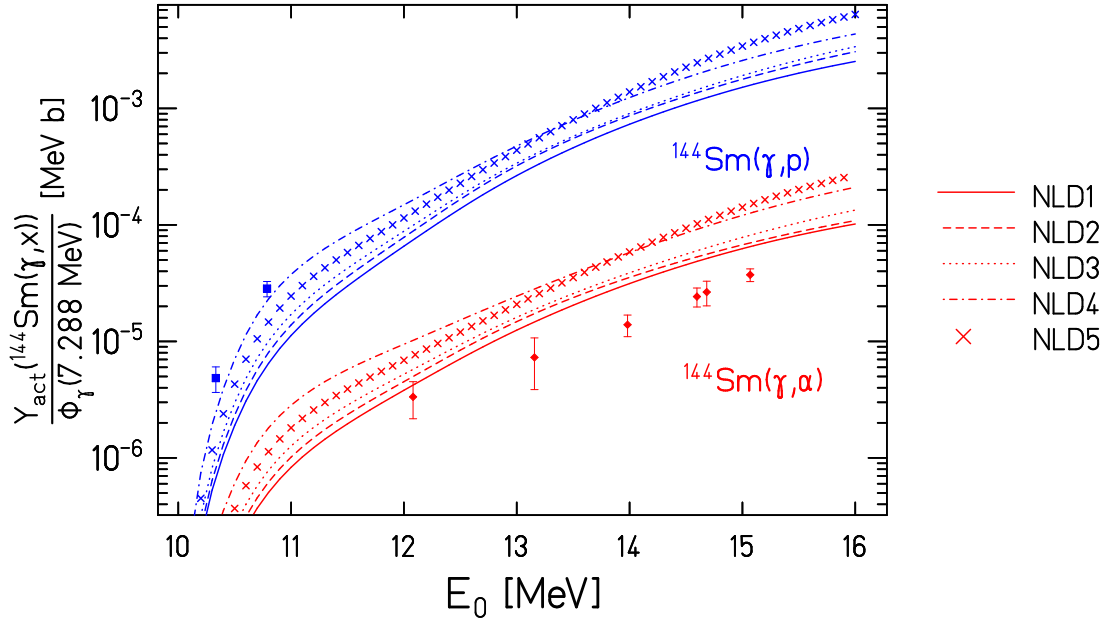


Figure 6.6: The  $^{144}\text{Sm}(\gamma, p)^{143}\text{Pm}$  (squares) and  $^{144}\text{Sm}(\gamma, \alpha)^{140}\text{Nd}$  (diamonds) activation yields compared to the simulated yields with different inputs for the nuclear level densities. The simulated yield curves are shown by different lines corresponding to the NLD models given in Table. 6.1 (NLD1 to NLD4). The cross symbols stand for predictions using the level density model 5 (NLD5).

to the simulated yield curves with different inputs to the nuclear level densities are given in Fig. 6.5 and Fig. 6.6. In these calculations, the  $\gamma$ -ray strength functions predicted by the model PSF0 and the optical model potentials by Koning and Delaroche (OMP1, see Table. 6.1) were used. For the  $^{144}\text{Sm}(\gamma, n)^{143g,m}\text{Sm}$  reaction yield, the simulated yields calculated using cross sections with the nuclear level density models NLD1, NLD2 and NLD3 do not differ much from each other and are in agreement with the experimental data within about 20% (see Fig. 6.5). The yield curve created using the microscopic models (NLD4, NLD5) are different from the analytical models. For the  $^{144}\text{Sm}(\gamma, p)^{143}\text{Pm}$  and  $^{144}\text{Sm}(\gamma, \alpha)^{140}\text{Nd}$  reactions, the simulated yields (Fig. 6.6) using different NLD models differ significantly from each other. For the  $(\gamma, \alpha)$  reaction yield, none of the models could describe the experimental results whereas for the  $(\gamma, p)$  reaction, the activation yield calculated using the microscopic level density model (NLD4, see Fig. 6.6) is in agreement with the experimental data.

In conclusion, most of the experimental results presented in thesis are well-described by the statistical model calculations. The yield calculations with different nuclear physics inputs reveals the predictive power of the model codes. The difference in the predictions between the NON-SMOKER and TALYS codes calls for a further investigation.



# Chapter 7

## Summary and Outlook

The 35 neutron-deficient heavy nuclides, so-called p-nuclei, are shielded from the rapid neutron capture by stable isobars and hence cannot be produced by the neutron capture processes. These are synthesized from the r- or s- seed nuclei by a combination of (p, $\gamma$ ) captures or the photon-induced reactions  $(\gamma,n)$ ,  $(\gamma,p)$  and  $(\gamma,\alpha)$ . The reaction rate predictions for the p-process flow is mostly from statistical models. The motivation behind this thesis work was to provide experimental data to test and improve statistical models.

The photon-induced reactions  $(\gamma,n)$ ,  $(\gamma,p)$  and  $(\gamma,\alpha)$  of  $^{144}\text{Sm}$  were investigated via the photoactivation method. The  $(\gamma,p)$  and  $(\gamma,n)$  reactions on  $^{92}\text{Mo}$  are included in [Erha09] and the  $^{92}\text{Mo}(\gamma,\alpha)$  experiments are discussed in Chapter 5 of this work. The photoneutron reactions discussed in this thesis have been studied for the whole region from the neutron threshold to beyond the top of the giant dipole resonance. The bremsstrahlung endpoint energies for the measurements range from 9.0 to 15.5 MeV. Special care was taken at each accelerator setting to measure the bremsstrahlung endpoint energy without relying on the magnetic beam transport elements. The endpoint energies have been measured via the photodisintegration of the deuteron.

The residual nuclei resulting from photoactivation were studied by  $\gamma$ -ray spectroscopy. A rabbit system has been used for the decay studies of nuclei with very short half-lives. For the  $^{144}\text{Sm}(\gamma,p)$  and  $^{144}\text{Sm}(\gamma,\alpha)$  reactions, the photoactivation experiments result in decay spectra with weak counting statistics. Therefore, the decay studies were performed under optimized background conditions in an underground laboratory (Felsenkeller) in Dresden.

The  $^{144}\text{Sm}(\gamma,n)$  and  $^{197}\text{Au}(\gamma,n)$  reaction yields have been compared to the yield calculated using cross sections from previous photoneutron experiments. A comparison of the two data sets leads to a conclusion on the inaccuracies in previous data. The activation yield for all the photodisintegration reactions has been compared with theoretical model predictions. For simulating the photoactivation yield, the Hauser-Feshbach model codes TALYS and NON-SMOKER were used. The experimental activation yields, in general, agree within a factor of 2 to the simulated yield using statistical model predictions. A new phenomenological parametrization of the photon strength function is proposed (see also [Jung08]). For the photoneutron reactions, the TALYS simulated yield calculated using the modified photon-strength functions describe the experimental data very well. In addition, the sensitivity of the TALYS code to the nuclear physics inputs like optical-model potentials, nuclear level densities and  $\gamma$ -ray strength functions has been discussed. The difference in the model predictions are strongly related to their nuclear physics inputs and calls for a further investigation.

The experimental data presented here are the very first results for the  $(\gamma,p)$  and  $(\gamma,\alpha)$  photodisintegration of p-nuclei. The statistical uncertainties involved are very small except for the

case of decay spectra with weak counting statistics. The systematic uncertainties are mostly from the photon flux determination (see Sect. 5.7). The systematic uncertainties involved in the endpoint energy determination is about 40 keV which plays a significant role only for endpoint energies close-above the neutron/proton-emission threshold of the photodisintegration reaction under consideration.

The advantage of the photoactivation experiments at ELBE is the availability of the high intense photon flux in the energy range up to 18 MeV which makes it possible to study the reactions of low-cross sections. However, the deduction of cross sections from the activation yield is tedious since the uncertainties involved in the unfolding procedure are very large.

The major limitation, in general, arises from the fact that the reaction products from the photoactivation are studied from the complimentary  $\beta$ -decays. If the resulting isotope is unstable, or if the half-life of the daughter nucleus is too long, or if the  $\gamma$ -intensity of the transition is too small, this method fails. For such cases, an alternative method known as Accelerator Mass Spectrometry (AMS) could be used. For instance, this highly promising technique is being used at the Munich Tandem accelerator and at the new facility DREAMS at FZ Dresden-Rossendorf. At Munich, efforts are being made to study the neutron capture cross sections of  $^{62,63}\text{Ni}$  (I. Dillmann et al.) which are of astrophysical importance for the s-process flow. In a collaboration with our group at FZD, the activation experiment  $^{64}\text{Ni}(\gamma, n)$  has been performed at the bremsstrahlung facility of the ELBE accelerator. The resulting isotope  $^{63}\text{Ni}$  ( $t_{1/2} \approx 100$  yrs) is now being studied in Munich.

Another approach to study the photon-induced reactions of importance to the p-process is by using the synchrotron radiation at the SPring-8 facility in Japan. At SPring-8, the high-energy part of synchrotron radiation produced by a 10T superconducting wiggler could successfully mimic the blackbody radiation of temperatures around 1.5 - 4.4 GK, the typical temperatures for p-process conditions. Simulations based on the statistical model calculations predict that a noticeable number of  $\gamma$ -induced reactions can be measured at this facility (expected yields for selected  $(\gamma, \alpha)$  reactions are given in Table 2 of Ref. [Mohr07]). This may help to reduce the uncertainties of p-process nucleosynthesis calculations.

At ELBE, one of our future plans is to measure the photon-induced reactions of  $^{96}\text{Ru}$ , to test the theoretical predictions for this p-nucleus. Similar to Mo, Ru-isotopes are also underproduced in the network calculations and experimental studies are highly recommended.

In conclusion, the results presented in the scope of this thesis work are extremely interesting for the Nuclear Astrophysics community. Further experiments to understand the heavy element formation, in general, are being pursued at different parts of the globe. The theoretical models are being tested and improved with observational astronomical as well as experimental nuclear physics data. The continuing enthusiasm will certainly keep Nuclear Astrophysics as a fascinating field of research, revealing the secrets behind the origin and formation of our universe.



# Appendix A

## Detector dimensions

### A.1 HPGe detectors at photon scattering site

detector	$d$ / mm	$l$ / mm	operating bias / V	polar angle	distance to target / mm
#1 Ortec 41-N31587A	79.1	90	-4500	127°/90°	320/280
#2 Eurisys 73615	76.5	86.9	+4500	90°	280
#3 Ortec 41-N31569A	78.2	93.1	-4800	127°/90°	320/280
#4 Eurisys 73633	76.7	86.9	+5000	90°	280

Table A.1: Specifications of the n-type High Purity Germanium (HPGe) detectors at the photon scattering site. The diameter and length of the detector crystal are denoted respectively by  $d$  and  $l$ .

### A.2 HPGe detectors at the counting facilities

detector	crystal diameter / mm	crystal length / mm	operating bias / V
LC1 Ortec 43-N31529A	68.3	76.7	-4500
LC2 Canberra b-04097	78.5	79	+4500
FK1 DSG PGB:-3010	58.0	61.0	+3500

Table A.2: Specifications of the 90% and 60% detectors (LC1, LC2) used in the low-level counting setup for decay spectroscopy studies. The properties of the well-type detector with 30% efficiency used at the underground laboratory (Felsenkeller) is also given.

### A.3 Silicon detectors for endpoint energy determination

Det. no	U/V	I/ $\mu$ A	FWHM/keV at 5486 keV
1	+145	0.04	19
2	+145	0.02	18
3	+145	0.02	23
4	+145	0.03	24

Table A.3: Specifications of the Si-detectors used for recording the proton spectra from deuteron breakup reaction.

# Appendix B

## Photopeak efficiency determination

### B.1 Calibration standards

For precise measurement of the activation yields at ELBE, it is important to have well-calibrated detectors for scattering and/or decay measurements. As given in Appendix A, different sets of detectors are used for the experiments discussed in this thesis - both at the photon scattering site and at the counting facilities. For calibration, we used the standard sources like  $^{57}\text{Co}$ ,  $^{226}\text{Ra}$ ,  $^{133}\text{Ba}$ ,  $^{54}\text{Mn}$ ,  $^{65}\text{Zn}$ ,  $^{137}\text{Cs}$ ,  $^{60}\text{Co}$  and  $^{88}\text{Y}$ . The spectrometric properties of the sources are listed in Table.B.1.

Nuclide	half-life/days	$A_0/\text{kBq}$	$E_\gamma/\text{keV}$	p	$C_i(60\%)$	$C_i(90\%)$
$^{57}\text{Co}$	271.83(8)	3.41(4)	122.06	0.8560(17)	1	1
			136.47	0.1068(8)	1	1
$^{226}\text{Ra}$	$5.84(3)\times 10^5$	52.5(26)	186.1	0.0351(6)	1	1
$^{137}\text{Cs}$	$1.100(9)\times 10^4$	25.01(25)	661.66	0.8500(20)	1	1
$^{54}\text{Mn}$	312.15(8)	8.91(7)	834.84	0.999750(12)	1	1
$^{65}\text{Zn}$	243.94(21)	18.40(26)	1115.54	0.5060(22)	1	1
$^{133}\text{Ba}$	$3.842(6)\times 10^3$	38.4(19)	276.398	0.07164(22)	0.9913	0.9910
			302.853	0.1833(6)	0.9951	0.9962
			356.017	0.6205(19)	0.9956	0.9966
			383.851	0.0894(3)	1.0083	1.0070
$^{60}\text{Co}$	1925.3(4)	42.9(17)	1173.237	0.999(3)	0.8187	0.7805
			1332.501	0.9998(1)	0.8144	0.7752
$^{88}\text{Y}$	106.63(25)	18.61(19)	898.036	0.940(3)	0.8323	0.7960
			1836.052	0.9933(3)	0.8160	0.7790

Table B.1: Spectrometric Properties of the calibration standards as given in the respective source certificates. The used  $\gamma$ -transitions, half-lives, respective reference activities and photon emission probabilities are given. The last two columns denote the correction factor due to coincidence summing for the multi gamma emitting nuclides, for the 60% and 90% detector respectively.

The definition for full-energy-peak efficiency is

$$\epsilon(E_\gamma) = \frac{N_\gamma}{N_s} = \frac{N_\gamma}{t_r p A_0 \exp\left(-\frac{\Delta t}{\tau}\right)} \quad (\text{B.1})$$

with  $N_\gamma$  = number of counts in the photopeak, corrected for dead-time and pile-up losses and  $N_s$  = number of photons emitted from the source. The other terms describe themselves as  $\Delta t$  - time elapsed since calibration up to measurement,  $A_0$  - activity of the source on the reference date,  $p$  - branching ratio corresponding to the energy  $E_\gamma$ ,  $\tau$  - the mean lifetime and  $t_r$  denotes the real time taken for data run.

## B.2 Coincidence summing corrections

For multi-gamma emitting nuclides like  $^{60}\text{Co}$ , the coincidence summing corrections has to be applied. Coincidence summing is a process in which the emission of  $\gamma$ -rays in cascade from the decay of a single radionuclide occurs within the resolving time of the detector and ends up being recorded together as a single event. This causes counts to be lost from the full-energy peaks and the peak areas need to be corrected. The magnitude of the corrections depends on the sample-detector geometry and the nuclide's decay scheme. For a simple decay scheme, the calculation of the correction factor is straightforward and depends on whether it is a "summing-in" or "summing-out" correction [Debe01].

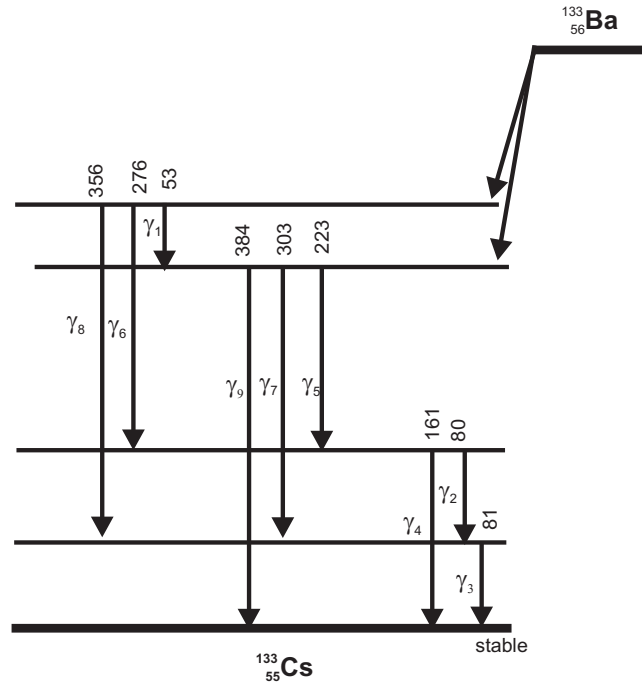


Figure B.1: Decay scheme of  $^{133}\text{Ba}$  - energies displayed in keV. The scheme is not drawn to scale.

For a complex decay scheme like  $^{133}\text{Ba}$ , more than one photons are emitted in cascade and for each cascade the correction factors have to be derived separately. Referring to the decay scheme given in Fig. B.1, we can group the correction factors for 276 keV ( $\gamma_6$ ) transition into two: one which comes out from the "summing-out" effects due to coincidence of  $\gamma_6$  with  $\gamma_4$  and with  $\gamma_2$ - $\gamma_3$  cascade and the other factor from "summing-in" effects due to  $\gamma_1$ - $\gamma_5$  cascade.

Accordingly, we developed a correction factor for this transition which is given by the expression

$$\frac{1}{C_6} = \left( 1 - f_{64}\epsilon_{t4} - f_{62}\epsilon_{t2} - \frac{\epsilon_{t3}}{(1 + \alpha_3)} \right) \cdot \left( 1 + \frac{p_1 f_{15} \epsilon_1 \epsilon_5}{p_6 \epsilon_6} \right) \quad (\text{B.2})$$

with

$$f_{64} = \frac{p_4}{p_4(1 + \alpha_4) + p_2(1 + \alpha_2)}$$

$$f_{15} = \frac{p_5}{p_5(1 + \alpha_5) + p_7(1 + \alpha_7) + p_9(1 + \alpha_9)}$$

and likewise. Here  $C_i$  stands for the correction factor,  $\alpha_i$  - total internal conversion coefficients,  $p_i$  -  $\gamma$  emission probabilities,  $\epsilon_i$  - full energy peak efficiencies and  $\epsilon_{ti}$  - total efficiencies for the detector used with  $i = 1, \dots, 9$ . The correction factors  $C_i$  for the corresponding  $\gamma$ -transitions are given in Table. B.1.

The total efficiencies needed for the coincidence summing corrections were measured with monoenergetic sources and compared with the simulated values. Coincidence summing effects depend strongly on the decay scheme. For example, the three dominant decay transitions of  $^{196}\text{Au}$  used for analysis of the  $^{197}\text{Au}(\gamma, n)$  reaction yield are at 333, 356 and 426 keV. For the transition at 333keV, the coincidence summing correction amounts to 24% and for 356 keV it is 6%, both with a relative uncertainty of 5%.



# Appendix C

## Photon scattering from $^{11}\text{B}$

The level-properties of  $^{11}\text{B}$  used for scattering studies will be discussed in this section. The information about the level energy  $E_x$ , the angular momentum  $J_x^\pi$ , the level width  $\Gamma$  were adopted from the online library of Evaluated Nuclear Structure Data Files (ENSDF) which refers to the revised Ajzenberg-Selove compilation ([Ajze90]). The correction to be applied for nuclear self absorption is given in the last column. It is for a  $^{11}\text{B}$  target made of pressed pill of 4.5 g boron powder inside cylindrical container which is 20 mm in diameter and has a thickness of 9 mm.

$E_x$ keV	$J_x^\pi$	$\Gamma_\gamma(\text{total})$ eV	$\frac{\Gamma_{\gamma 0}}{\Gamma_\gamma(\text{total})}$ %	$C_{nsac}$ %
2124.693(27)	$1/2^-$	0.120(9)	100	11.8
4444.89(50)	$5/2^-$	0.56(2)	100	17.2
5020.31(30)	$3/2^-$	1.901(554)	85.6(6)	22.8
7285.51(43)	$5/2^+$	1.141(86)	87(2)	7.5
8920.2(20)	$5/2^-$	4.37(2)	95(1)	15.9

Table C.1: Properties of the levels in  $^{11}\text{B}$  used for photon scattering experiments.

The known transitions of  $^{11}\text{B}$  given in Table. C.1 were used for energy calibration in the spectra measured at the photon scattering site. Since the  $\gamma$ -rays are emitted from a recoiling nucleus their energy is shifted with respect to the transition energy due to the recoil energy and the Doppler shift. Expressions for Doppler shift and recoil energy are derived from the momentum and energy conservation laws. Considering the decay of a nucleus of mass  $M$  at rest, from an initial excited state  $E_i$  to a final state  $E_f$ ,  $E_x = E_i - E_f$ , the recoil corrected  $\gamma$ -ray energy  $E_\gamma$  is given by the expression:

$$E_\gamma \cong E_x - \frac{(E_x)^2}{2Mc^2} \quad (\text{C.1})$$

If the  $\gamma$ -rays are emitted under angles different than  $90^\circ$  then their energies change due to the Doppler shift:

$$E'_\gamma = E_\gamma \cdot \frac{1}{1 + \frac{E_\gamma}{Mc^2} \cdot (1 - \cos \theta)} \quad (\text{C.2})$$

where  $\theta$  is the angle of the detector relative to the beam. The calibration-transition energy is

transformed to  $\gamma$ -ray energy according to Eqs. (C.1) and (C.2) and used for energy calibration of the measured spectra.



At ELBE, the spectra are measured with HPGe detectors at angles  $90^\circ$  and  $127^\circ$ . The  $\gamma$ -energies  $E_\gamma$ , the angular correlation coefficient  $W(\theta)$ , and the mixing ratio  $\delta$  is given in the following table. The mixing ratio is given in Krane-Steffen phase convention.

$E_\gamma(90^\circ)$ keV	$W(90^\circ)$	$E_\gamma(127^\circ)$ keV	$W(127^\circ)$	$\delta$	$\Pi L$
2124.47(3)	1.000	2124.21(3)	1.000		$M1$
4443.9(5)	1.000	4442.8(5)	1.000	+0.19(3)	$M1 + E2$
5019.1(3)	0.938	5017.6(3)	1.005	-0.03(5)	$M1$
7282.9(4)	0.931	7279.8(4)	1.006		$E1$
8916(2)	0.837	8912(2)	1.001	-0.11(4)	$M1 + E2$



# Appendix D

## Decay properties of the photodisintegration targets

Key reaction	Daughter decay	$t_{1/2}$	$E_\gamma/\text{keV}$	p
$^{197}\text{Au}(\gamma, n)$	$^{196}\text{Au}(\beta^+)^{196}\text{Pt}$	6.1669(6) d	333.03(5)	0.229(10)
			355.73(5)	0.87(3)
	$^{196}\text{Au}(\beta^-)^{196}\text{Hg}$		426.10(8)	0.066(3)
$^{144}\text{Sm}(\gamma, n)$	$^{143}\text{Sm}(\text{EC}+\beta^+)^{143}\text{Pm}$	8.75(8) m	1056.58(7)	0.019(2)
			1173.18(7)	0.004161(544)
			1514.98(7)	0.006593(75)
			1403.06(7)	0.003496(414)
	$^{143}\text{Sm}$ IT decay	66(2) s	754.4(7)	0.8988(6)
$^{144}\text{Sm}(\gamma, \alpha)$	$^{140}\text{Nd}(\text{EC})^{140}\text{Pr}(\text{no } \gamma)$	3.37(2) d	1596.11(19)	0.0050(4)
	$^{140}\text{Pr}(\beta^+)^{140}\text{Ce}$			
$^{144}\text{Sm}(\gamma, p)$	$^{143}\text{Pm}(\text{EC})^{143}\text{Nd}$	265(7) d	741.98(4)	0.385(24)
$^{92}\text{Mo}(\gamma, \alpha)$	$^{88}\text{Zr}(\text{EC})^{88}\text{Y}(\text{unstable})$	83.4(3) d	392.9(1)	1
	$^{88}\text{Y}(\beta^+)^{88}\text{Sr}$			

Table D.1: Decay properties of the daughter nuclei stemming from the respective photodisintegration reactions on Au/Sm/Mo. The first two columns describe the photodisintegration reaction and daughter decay. The half life of the decay, transition energies and photon emission probabilities are given respectively in the next three columns. The decay properties were all taken from the Evaluated Nuclear Structure Data Files of the National Nuclear Data Center online service [ENDSF].



# Bibliography

- [Ajze90] F. Ajzenberg-Selove. Energy Levels of Light Nuclei  $A = 11-12$ . *Nuclear Physics A*. 506, page 1, 1990.
- [Ande89] E. Anders and N. Grevesse. Abundances of the elements - meteoritic and solar. *Geochimica Et Cosmochimica Acta*. 53, page 197, 1989.
- [Angu99] C. Angulo, M. Arnould, M. Rayet, P. Descouvemont, D. Baye, C. Leclercq-Willain, A. Coc, S. Barhoumi, P. Aguer, C. Rolfs, R. Kunz, J. W. Hammer, A. Mayer, T. Paradellis, S. Kossionides, C. Chronidou, K. Spyrou, S. Degl'Innocenti, G. Fiorentini, B. Ricci, S. Zavatarelli, C. Providencia, H. Wolters, J. Soares, C. Grama, J. Rahighi, A. Shotter, and M. L. Racht. A compilation of charged-particle induced thermonuclear reaction rates. *Nuclear Physics A*. 656, page 3, 1999.
- [Arno03] M. Arnould and S. Goriely. The p-process of stellar nucleosynthesis: astrophysics and nuclear physics status. *Physics Reports*. 384, page 1, 2003.
- [Audo72] J. Audouze and D. N. Schramm. Sm-146 - chronometer for p-process nucleosynthesis. *Nature*. 237, page 447, 1972.
- [Axel62] P. Axel. Electric Dipole Ground-State Transition Width Strength Function and 7-MeV Photon Interactions. *Physical Review*. 126, page 671, 1962.
- [Bao00] Z. Y. Bao, H. Beer, F. Kappeler, F. Voss, K. Wisshak, and T. Rauscher. Neutron cross sections for nucleosynthesis studies. *Atomic Data and Nuclear Data Tables*. 76, page 70, 2000.
- [Bart73] G. A. Bartholomew, E. D. Earle, A. J. Ferguson, J. W. Knowles, and M. A. Lone. Gamma-ray strength functions. *Advances in Nuclear Physics*. 7, page 229, 1973.
- [Baug01] E. Bauge, J. P. Delaroche, and M. Girod. Lane-consistent, semimicroscopic nucleon-nucleus optical model. *Physical Review C*. 63, 024607, 2001.
- [Berg69] R. Bergere, H. Beil, P. Carlos, and A. Veyssiere. Photoneutron cross sections of I, Ce, Sm, Er, and Lu. *Nuclear Physics A*. 133, page 417, 1969.
- [Berm87] B. L. Berman, R. E. Pywell, S. S. Dietrich, M. N. Thompson, K. G. McNeill, and J. W. Jury. Absolute photoneutron cross sections for Zr, I, Pr, Au, and Pb. *Physical Review C*. 36, page 1286, 1987.
- [Beth39] H. A. Bethe. Energy production in stars. *Physical Review*. 55, page 103, 1939.
- [Beth38] H. A. Bethe and C. L. Critchfield. The formation of deuterons by proton combination. *Physical Review*. 54, page 248, 1938.

- [Bock79] A. Bockisch, K. Bharuth-Ram, A. M. Kleinfeld, and K. P. Lieb. Reorientation Effect Measurements of Even Mercury Isotopes. *Zeitschrift Fur Physik A*. 291, page 245, 1979.
- [Boot06] A. I. Boothroyd. Heavy elements in stars. *Science*. 314, page 1690, 2006.
- [Brin57] D. M. Brink. Individual Particle and Collective Aspects of the Nuclear Photoeffect. *Nuclear Physics*. 4, page 215, 1957.
- [Burb57] E. M. Burbidge, G. R. Burbidge, W. A. Fowler, and F. Hoyle. Synthesis of the elements in stars. *Reviews of Modern Physics*. 29, page 547, 1957.
- [Bush91] B. Bush and Y. Alhassid. On the width of the giant dipole resonance in deformed nuclei. *Nuclear Physics A*. 531, page 27, 1991.
- [Carl74] P. Carlos, H. Beil, R. Bergere, A. Lepretre, A. Deminiac, and Veyssier.A. Giant dipole resonance in transition region of samarium isotopes. *Nuclear Physics A*. 225, page 171, 1974.
- [Chlo99] F. R. Chloupek, A. S. Murphy, R. N. Boyd, A. L. Cole, J. Gorres, R. T. Guray, G. Raimann, J. J. Zach, T. Rauscher, J. V. Schwarzenberg, P. Tischhauser, and M. C. Wiescher. Measurements of proton radiative capture cross sections relevant to the astrophysical rp- and gamma-processes. *Nuclear Physics A*. 652, page 391, 1999.
- [Cost00] V. Costa, M. Rayet, R. A. Zappala, and M. Arnould. The synthesis of the light Mo and Ru isotopes: how now no need for an exotic solution? *Astronomy and Astrophysics*. 358, page L67, 2000.
- [Cowa91] J. J. Cowan, F. K. Thielemann, and J. W. Truran. The r-process and nucleochronology. *Physics Reports*. 208, page 267, 1991.
- [Debe01] K. Debertin and R. G. Helmer.  *$\gamma$  and X-ray Spectrometry with Semiconductor Detectors*. Elsevier Science Publications, 2001.
- [Diet88] S. S. Dietrich and B. L. Berman. Atlas of Photoneutron Cross-Sections Obtained with Monoenergetic Photons. *Atomic Data and Nuclear Data Tables*. 38, page 199, 1988.
- [Dill06] I. Dillmann, M. Heil, F. Kppeler, R. Plag, T. Rauscher, and F.-K. Thielemann. KADoNiS - The Karlsruhe Astrophysical Database of Nucleosynthesis in Stars. *AIP Conference Proceedings*. 819, page 123, 2006.
- [Eise88] J.M. Eisenberg and W. Greiner. *Nuclear Theory Vol. 2: Excitation mechanisms of the nucleus, Third Edition*. North Holland Physics Publishers, Amsterdam, 1988.
- [ENDSF] Evaluated Nuclear Structure Data Files (ENDSF). *The database service of National Nuclear Data Center (NNDC)*. <http://www.nndc.bnl.gov/ensdf/>, 2008.
- [Erha09] M. Erhard. Photoaktivierung des p-Kerns  $^{92}\text{Mo}$  am Bremsstrahlungsmessplatz von ELBE. *PhD thesis*, 2009.

- [Erha04] M. Erhard, E. Grosse, A. Hartmann, A. R. Junghans, C. Nair, K. D. Schilling, W. Schulze, R. Schwengner, and A. Wagner. The Photoactivation Setup at ELBE. *Wissenschaftlich-Technische Berichte FZR-372*, page 14, 2004.
- [Erha06b] M. Erhard, A. R. Junghans, R. Beyer, E. Grosse, K. Klug, K. Kosev, C. Nair, N. Nankov, G. Rusev, K. D. Schilling, R. Schwengner, and A. Wagner. Photodissociation of p-process nuclei studied by bremsstrahlung induced activation. *European Physical Journal A* 27, 135, 2006.
- [Erha06a] M. Erhard, C. Nair, R. Beyer, E. Grosse, A. R. Junghans, K. Klug, K. Kosev, N. Nankov, G. Rusev, K. D. Schilling, R. Schwengner, and A. Wagner. Electromagnetic excitations in nuclei: from photon scattering to photodisintegration. *Proceedings of Science, PoS (NIC IX) 056*, 2006.
- [Eric60] T. Ericson. The statistical model and nuclear level densities. *Advances in Physics*. 9, page 425, 1960.
- [Faut07] M. Fauth, P. Crespo, A. R. Junghans, and A. Wagner. CAP - a CAMAC Acquisition through PCI. *Internal status report, Institute of Radiation Physics, Forschungszentrum Dresden-Rossendorf*, 2007.
- [Froe06] C. Fröhlich, G. Martinez-Pinedo, M. Liebendorfer, F. K. Thielemann, E. Bravo, W. R. Hix, K. Langanke, and N. T. Zinner. Neutrino-induced nucleosynthesis of  $A > 64$  nuclei: The  $\nu$  p process. *Physical Review Letters*. 96, page 4, 2006.
- [Fulo96] Z. Fulöp, A. Z. Kiss, E. Somorjai, C. E. Rolfs, H. P. Trautvetter, T. Rauscher, and H. Oberhummer. Ge-70(alpha,gamma)Se-74 cross section measurements at energies of astrophysical interest. *Zeitschrift Fur Physik A*. 355, page 203, 1996.
- [Fult62] S. C. Fultz, J. T. Caldwell, R. L. Bramblett, and N. A. Kerr. Photoneutron Cross-Section Measurements on Gold Using nearly Monochromatic Photons. *Physical Review*. 127, page 1273, 1962.
- [Gabr00] F. Gabriel, P. Gippner, E. Grosse, D. Janssen, P. Michel, H. Prade, A. Schamlott, W. Seidel, A. Wolf, R. Wünsch, and ELBE-crew. The Rossendorf radiation source ELBE and its FEL project. *Nuclear Instruments and Methods B*. 161, page 1143, 2000.
- [Gala03] S. Galanopoulos, P. Demetriou, M. Kokkoris, S. Harissopoulos, R. Kunz, M. Fey, J. W. Hammer, G. Gyurky, Z. Fulop, E. Somorjai, and S. Goriely. The Sr-88(p,gamma)Y-89 reaction at astrophysically relevant energies. *Physical Review C*. 67, 015801, 2003.
- [Gori02] S. Goriely and E. Khan. Large-scale QRPA calculation of E1-strength and its impact on the neutron capture cross section. *Nuclear Physics A*. 706, page 217, 2002.
- [Gori01] S. Goriely, F. Tondeur, and J. M. Pearson. A Hartree-Fock nuclear mass table. *Atomic Data and Nuclear Data Tables*. 77, page 311, 2001.
- [Gure80] G. M. Gurevich, L. E. Lazareva, V. M. Mazur, S. Y. Merkulov, and G. V. Solodukhov. Total photoabsorption cross sections for high-Z elements in the energy range 7–20 MeV. *Nuclear Physics A*. 338, page 97, 1980.

- [Gyur03] G. Gyurky, Z. Fulop, E. Somorjai, M. Kokkoris, S. Galanopoulos, P. Demetriou, S. Harissopulos, T. Rauscher, and S. Goriely. Proton induced reaction cross section measurements on Se isotopes for the astrophysical p process. *Physical Review C*. *68*, 055803, 2003.
- [Gyur01] G. Gyurky, E. Somorjai, Z. Fulop, S. Harissopulos, P. Demetriou, and T. Rauscher. Proton capture cross section of Sr isotopes and their importance for nucleosynthesis of proton-rich nuclides. *Physical Review C*. *64*, 065803, 2001.
- [Hara07] K. Y. Hara, H. Harada, F. Kitatani, S. Goko, S. Y. Hohara, T. Kaihori, A. Makinaga, H. Utsunomiya, H. Toyokawa, and K. Yamada. Measurements of the Sm-152( $\gamma$ ,n) cross section with laser-compton scattering gamma rays and the photon difference method. *Journal of Nuclear Science and Technology*. *44*, page 938, 2007.
- [Haris01] S. Harissopulos, E. Skreti, P. Tsagari, G. Souliotis, P. Demetriou, T. Paradellis, J. W. Hammer, R. Kunz, C. Angulo, S. Goriely, and T. Rauscher. Cross section measurements of the Nb-93(p, $\gamma$ )Mo-94 reaction at E-p=1.4-4.9 MeV relevant to the nucleosynthetic p process. *Physical Review C*. *64*, 055804, 2001.
- [Hasp08a] J. Hasper, S. Muller, D. Savran, L. Schnorrenberger, K. Sonnabend, and A. Zilges. Investigation of photoneutron reactions close to and above the neutron emission threshold in the rare earth region. *Physical Review C*. *77*, 015803, 2008.
- [Hasp08b] Jens Hasper. Systematic study of photoneutron reactions just above the neutron emission threshold. *PhD thesis*, Verlag Dr. Hut Publications, Munich, Germany, <http://www.dr.hut-verlag.de/>, 2008.
- [Haug08] E. Haug. Bremsstrahlung cross-section with screening and Coulomb corrections at high energies. *Radiation Physics and Chemistry*. *77*, page 207, 2008.
- [Haus52] W. Hauser and H. Feshbach. The inelastic scattering of neutrons. *Physical Review*. *87*, page 366, 1952.
- [Haya04] T. Hayakawa, N. Iwamoto, T. Shizuma, T. Kajino, H. Umeda, and K. Nomoto. Evidence for nucleosynthesis in the supernova gamma process: Universal scaling for p nuclei. *Physical Review Letters*. *93*, 161102, 2004.
- [Hila06] S. Hilaire and S. Goriely. Global microscopic nuclear level densities within the HFB plus combinatorial method for practical applications. *Nuclear Physics A*. *779*, page 63, 2006.
- [RIPL-2] <http://www-nds.iaea.or.at/RIPL-2/>. *Handbook for calculations of nuclear reaction data: Reference Input Parameter Library*.
- [Jaeg01] M. Jaeger, R. Kunz, A. Mayer, J. W. Hammer, G. Staudt, K. L. Kratz, and B. Pfeiffer. Ne-22( $\alpha$ ,n)Mg-25: The key neutron source in massive stars. *Physical Review Letters*. *87*, 202501, 2001.
- [Jeuk74] J. P. Jeukenne, A. Lejeune, and C. Mahaux. Optical-model potential in finite nuclei from Reid's hard core interaction. *Physical Review C*. *10*, page 1391, 1974.



- [Jeuk76] J.-P. Jeukenne, A. Lejeune, and C. Mahaux. Many-body theory of nuclear matter. *Physics Reports*. 25C, page 83, 1976.
- [Jeuk77a] J. P. Jeukenne, A. Lejeune, and C. Mahaux. Microscopic calculation of symmetry and coulomb components of complex optical-model potential. *Physical Review C*. 15, page 10, 1977.
- [Jeuk77b] J. P. Jeukenne, A. Lejeune, and C. Mahaux. Optical-model potential in finite nuclei from reids hard-core interaction. *Physical Review C*. 16, page 80, 1977.
- [Jung08] A. R. Junghans, G. Rusev, R. Schwengner, A. Wagner, and E. Grosse. Photon data shed new light upon the GDR spreading width in heavy nuclei. *Physics Letters B*. 670, page 200, 2008.
- [Just07] M. Justus, U. Lehnert, P. Michel, and P. Evtushenko. Design of an electron beam energy control loop using transverse dispersion. *Proceedings of DIPAC 2007-8th European Workshop on Beam Diagnostics and Instrumentation for Particle Accelerators; 20.-23.05.2007; Venice,Italy*, <http://www.elettra.trieste.it/dipac07/>, <http://www.jacow.org/>, 2007.
- [Kaep99] F. Käppeler. The origin of the heavy elements: The s process. *Progress in Particle and Nuclear Physics*. 43, page 419, 1999.
- [Khan01] E. Khan, T. Suomijarvi, Y. Blumenfeld, N. Van Giai, N. Alamanos, F. Auger, E. Bauge, D. Beaumel, J. P. Delaroche, P. Delbourgo-Salvador, A. Drouart, S. Fortier, N. Frascaria, A. Gillibert, M. Girod, C. Jouanne, K. W. Kemper, A. Lagoyannis, V. Lapoux, A. Lépine-Szily, I. Lhenry, J. Libert, F. Maréchal, J. M. Maison, A. Musumarra, S. Ottini-Hustache, P. Piattelli, S. Pita, E. C. Pollacco, P. Roussel-Chomaz, D. Santonocito, J. E. Sauvestre, J. A. Scarpaci, and T. Zerguerras. Proton scattering from the unstable nuclei S-30 and Ar-34: structural evolution along the sulfur and argon isotopic chains. *Nuclear Physics A* 694, page 103, 2001.
- [Koni03] A. J. Koning and J. P. Delaroche. Local and global nucleon optical models from 1 keV to 200 MeV. *Nuclear Physics A*. 713, page 231, 2003.
- [Koni08] A. J. Koning, S. Hilaire, and S. Goriely. Global and local level density models. *Nuclear Physics A*. 810, page 13, 2008.
- [Koni04] A.J. Koning, S. Hilaire, and M.C. Duijvestijn. TALYS: Comprehensive nuclear reaction modeling. *Proceedings of International Conference on Nuclear Data for Science and Technology - ND2004, AIP vol. 769, eds. R.C. Haight, M.B. Chadwick, T. Kawano, and P. Talou, Sep. 26 - Oct. 1, 2004, Santa Fe, USA*, page 1154, 2005.
- [Kope90] J. Kopecky and M. Uhl. Test of gamma-ray strength functions in nuclear reaction model calculations. *Physical Review C*. 41, page 1941, 1990.
- [Lamb92] D. L. Lambert. The p-nuclei: abundances and origins. *Astronomy and Astrophysics Review*. 3, page 201, 1992.
- [Lehn06] U. Lehnert. NMR magnetic field measurements and beam energy calibration. *Wissenschaftlich-Technische Berichte FZD-473*, page 9, 2006.

- [Leje80] A. Lejeune. Low-energy optical-model potential in finite nuclei from reid hard-core interaction. *Physical Review C*. 21, page 1107, 1980.
- [Maut90] A. Mauthofer, K. Stelzer, J. Idzko, T. W. Elze, H. J. Wollersheim, H. Emling, P. Fuchs, E. Grosse, and D. Schwalm. Triaxiality and gamma-softness in Pt-196. *Zeitschrift Fur Physik A*. 336, page 263, 1990.
- [Mazu95] V. M. Mazur, V. A. Zheltonozhskii, and Z. M. Bigan. Excitation of isomeric states in the reaction  $(\gamma, n)$  for  $N=82$  shell nuclei. *Physics of Atomic Nuclei*. 58, page 898, 1995.
- [McCu81] C. M. McCullagh, M. L. Stelts, and R. E. Chrien. Dipole radiative strength functions from resonance neutron-capture. *Physical Review C*. 23, page 1394, 1981.
- [McFa66] L. McFadden and G. R. Satchler. Optical-Model Analysis of Scattering of 24.7 MeV Alpha Particles. *Nuclear Physics*. 84, page 177, 1966.
- [Mohr07] P. Mohr, Z. Fulop, and H. Utsunomiya. Photo-induced nucleosynthesis: Current problems and experimental approaches. *European Physical Journal A*. 32, page 357, 2007.
- [Mohr97] P. Mohr, T. Rauscher, H. Oberhummer, Z. Mate, Z. Fulop, E. Somorjai, M. Jaeger, and G. Staudt. Sm-144-alpha optical potential at astrophysically relevant energies derived from Sm-144(alpha,alpha) Sm-144 elastic scattering. *Physical Review C*. 55, page 1523, 1997.
- [Mohr00] P. Mohr, K. Vogt, M. Babilon, J. Enders, T. Hartmann, C. Hutter, T. Rauscher, S. Volz, and A. Zilges. Experimental simulation of a stellar photon bath by bremsstrahlung: the astrophysical gamma-process. *Physics Letters B*. 488, page 127, 2000.
- [Mori06] Vance Ryan Morrison. The photodisintegration of deuterium-Calibration of the Lund Photon Tagger. *BSc honours thesis*, Department of Physics, Mount Allison University, Sackville, New Brunswick, Canada, 2006.
- [Muel06] S. Müller, A. Kretschmer, K. Sonnabend, A. Zilges, and D. Galaviz. Re-187(gamma,n) cross section close to and above the neutron threshold. *Physical Review C*. 73, 025804, 2006.
- [Myer77] W. D. Myers, W. J. Swiatecki, T. Kodama, L. J. Eljaick, and E. R. Hilf. Droplet model of giant dipole resonance. *Physical Review C*. 15, 2032, 1977.
- [Nair08c] C. Nair, M. Erhard, A. R. Junghans, D. Bemmerer, R. Beyer, E. Grosse, J. Klug, K. Kosev, G. Rusev, K. D. Schilling, R. Schwengner, and A. Wagner. Photodisintegration of the p-nuclei 92Mo and 144Sm in the astrophysically relevant energy window. *Proceedings of Science, PoS (NIC X) 045*, 2008.
- [Nair08b] C. Nair, M. Erhard, A. R. Junghans, D. Bemmerer, R. Beyer, E. Grosse, K. Kosev, G. Rusev, K. D. Schilling, R. Schwengner, and A. Wagner. Photoactivation experiment on 197Au and its implications on the dipole strength in heavy nuclei. *Physical Review C*. 78, 055802, 2008.

- [Nair08a] C. Nair, A. R. Junghans, M. Erhard, D. Bemmerer, R. Beyer, P. Crespo, E. Grosse, M. Fauth, K. Kosev, G. Rusev, K. D. Schilling, R. Schwengner, and A. Wagner. Photodisintegration studies on p-nuclei: the case of Mo and sm isotopes. *Journal of Physics G*. 35, 014036, 2008.
- [Nair04] C. Nair, A.R. Junghans, A. Wagner, M. Erhard, and E. Grosse. Coincidence Summing Corrections and Peak Fit Functions for  $\gamma$ - Spectra. *Wissenschaftlich-Technische Berichte FZR-372*, page 18, 2004.
- [Nies98] S. Niese, M. Koehler, and B. Gleisberg. Low-level counting techniques in the underground laboratory "Felsenkeller" in Dresden. *Journal of Radioanalytical and Nuclear Chemistry*. 233, page 167, 1998.
- [Ozka02] N. Ozkan, A. S. J. Murphy, R. N. Boyd, A. L. Cole, A. Famiano, R. T. Guray, M. Howard, L. Sahin, J. J. Zach, R. deHaan, J. Gorres, M. C. Wiescher, M. S. Islam, and T. Rauscher. Cross section measurements of the Pd-102(p, gamma)Ag-103 Sn-116(p, gamma)Sb-117, and Sn-112(alpha, gamma)Te-116 reactions relevant to the astrophysical rp- and gamma-processes. *Nuclear Physics A*. 710, page 469, 2002.
- [Penf59] A. S. Penfold and J. E. Leiss. Analysis of Photonuclear Cross Sections. *Physical Review*. 114, page 1332, 1959.
- [Radf95] D. C. Radford. ESCL8R and LEVIT8R: Software for interactive graphical analysis of HPGe coincidence data sets. *Nuclear Instruments and Methods A*. 361, page 297, 1995.
- [Rapp01] W. Rapp, H. J. Brede, R. Heil, D. Hentschel, F. Kappeler, H. Klein, R. Reifarh, and T. Rauscher. Alpha and neutron induced reactions on ruthenium. *Nuclear Physics A*. 688, page 427C, 2001.
- [Rapp06] W. Rapp, J. Gorres, M. Wiescher, H. Schatz, and F. Kappeler. Sensitivity of p-process nucleosynthesis to nuclear reaction rates in a 25 M $\odot$  supernova model. *Astrophysical Journal*. 653, page 474, 2006.
- [Raus00] T. Rauscher and F. K. Thielemann. Astrophysical reaction rates from statistical model calculations. *Atomic Data and Nuclear Data Tables*. 75, page 1, 2000.
- [Raus04] T. Rauscher and F. K. Thielemann. Predicted cross-sections for photon-induced particle emission. *Atomic Data and Nuclear Data Tables*. 88, page 1, 2004.
- [Raus97] T. Rauscher, F. K. Thielemann, and K. L. Kratz. Nuclear level density and the determination of thermonuclear rates for astrophysics. *Physical Review C*. 56, page 1613, 1997.
- [Roch72] G. Roche, J. Proriol, and C. Ducos. Bremsstrahlung Cross-Section Formula Including a High-Order Coulomb Correction. *Physical Review A*. 5, page 2403, 1972.
- [Ruse08] G. Rusev, R. Schwengner, F. Donau, M. Erhard, E. Grosse, A. R. Junghans, K. Kosev, K. D. Schilling, A. Wagner, F. Becvar, and M. Krlicka. Low-energy tail of the giant dipole resonance in Mo-98 and Mo-100 deduced from photon-scattering experiments. *Physical Review C*. 77, 064321, 2008.

- [Salv87] F. Salvat, J. D. Martinez, R. Mayol, and J. Parellada. Analytical Dirac-Hartree-Fock-Slater screening function for atoms ( $Z = 1-92$ ). *Physical Review A*. 36, page 467, 1987.
- [Saut97] T. Sauter and F. Kappeler.  $(p,\gamma)$  rates of Mo-92, Mo-94, Mo-95, Mo-98: Towards an experimentally founded database for p-process studies. *Physical Review C*. 55, page 3127, 1997.
- [Schi51] L. I. Schiff. Energy-Angle Distribution of Thin Target Bremsstrahlung. *Physical Review*. 83, page 252, 1951.
- [Schi03a] K.D. Schilling, F. Dönau, E. Grosse, L. Käubler, R. Schwengner, A. Wagner, B. Wustmann, U. Lehnert, A. Nowak, B. Rimarzig, and R. Schlenk. Radiator for the Production of Bremsstrahlung at ELBE. *Wissenschaftlich-Technische Berichte FZR-372*, page 30, 2003.
- [Schi02a] K.D. Schilling, F. Dönau, L. Käubler, A. Wagner, W. Neumann, Th. Riedel, and R. Schlenk. Bremsstrahlung Collimator for the NRF Set-Up at ELBE. *Wissenschaftlich-Technische Berichte FZR-341*, page 37, 2002.
- [Schi03c] K.D. Schilling, M. Langer, U. Lehnert, and W. Schulze. Beam Separation Magnet of the Bremsstrahlung Facility at ELBE. *Wissenschaftlich-Technische Berichte FZR-372*, page 33, 2003.
- [Schi02b] K.D. Schilling, A. Wagner, F. Dönau, L. Käubler, R. Schwengner, W. Neumann, and R. Schlenk. Beam Shutter and Hardener for the NRF Set-Up at ELBE. *Wissenschaftlich-Technische Berichte FZR-341*, page 41, 2002.
- [Schw05] R. Schwengner, R. Beyer, F. Donau, E. Grosse, A. Hartmann, A. R. Junghans, S. Mallion, G. Rusev, K. D. Schilling, W. Schulze, and A. Wagner. The photon-scattering facility at the superconducting electron accelerator ELBE. *Nuclear Instruments and Methods in Physics Research Section A*. 555, page 211, 2005.
- [Schw03] R. Schwengner, L. Käubler, M. Langer, G. Rusev, W. Schulze, and A. Wagner. Detector Setup for Nuclear-Resonance-Fluorescence Experiments at ELBE. *Wissenschaftlich-Technische Berichte FZR-372*, page 27, 2003.
- [Selt86] S. M. Seltzer and M. J. Berger. Bremsstrahlung Energy Spectra from Electrons with Kinetic Energy 1 KeV - 10 GeV Incident on Screened Nuclei and Orbital Electrons of Neutral Atoms with  $Z = 1 - 100$ . *Atomic Data and Nuclear Data Tables*. 35, page 345, 1986.
- [Skor75] S. J. Skorka. *Electromagnetic interaction in nuclear spectroscopy*. North-Holland Publications, Amsterdam, 1975.
- [Somo98] E. Somorjai, Z. Fulop, A. Z. Kiss, C. E. Rolfs, H. P. Trautvetter, U. Greife, M. Junker, S. Goriely, M. Arnould, M. Rayet, T. Rauscher, and H. Oberhummer. Experimental cross section of Sm-144( $\alpha, \gamma$ )Gd-148 and implications for the p-process. *Astronomy and Astrophysics*. 333, page 1112, 1998.
- [Sonn03] K. Sonnabend, P. Mohr, K. Vogt, A. Zilges, A. Mengoni, T. Rauscher, H. Beer, F. Kappeler, and R. Gallino. The s-process branching at W-185. *Astrophysical Journal*. 583, page 506, 2003.

- [Sonn04] K. Sonnabend, K. Vogt, D. Galaviz, S. Muller, and A. Zilges. Systematic study of (gamma,n) reaction rates for  $Z \leq 78$  isotopes. *Physical Review C*. 70, 035802, 2004.
- [Soro73] Y. I. Sorokin, Khrushch.Va, and B. A. Yurev. Cross Sections of Photoneutron Reactions for Au-197 and Bi-209. *Izvestiya Akademii Nauk Sssr Seriya Fizicheskaya*. 37, page 1890, 1973.
- [Sues56] H. E. Suess and H. C. Urey. Abundances of the elements. *Reviews of Modern Physics*. 28, page 53, 1956.
- [Thie83] F. K. Thielemann and M. Arnould. *Proceedings of International Conference on Nuclear Data for Science and Technology*, edited by K.Böckhoff, page 762, 1983.
- [Utsu03] H. Utsunomiya, H. Akimune, S. Goko, M. Ohta, H. Ueda, T. Yamagata, K. Yamasaki, H. Ohgaki, H. Toyokawa, Y. W. Lui, T. Hayakawa, T. Shizuma, E. Khan, and S. Goriely. Cross section measurements of the Ta-181(gamma,n)Ta-180 reaction near neutron threshold and the p-process nucleosynthesis. *Physical Review C*. 67, 015807, 2003.
- [Utsu06] H. Utsunomiya, P. Mohr, A. Zilges, and M. Rayet. Direct determination of photodisintegration cross sections and the p-process. *Nuclear Physics A*. 777, page 459, 2006.
- [Vans81] R. Vanska and R. Rieppo. The experimental isomeric cross-section ratio in the nuclear activation technique. *Nuclear Instruments and Methods*. 179, page 525, 1981.
- [Veys70] A. Veysiere, H. Beil, R. Bergere, P. Carlos, and A. Lepretre. Photoneutron cross sections of Pb-208 and Au-197. *Nuclear Physics A*. 159, page 561, 1970.
- [Vidm05] T. Vidmar. EFFTRAN - A Monte Carlo efficiency transfer code for gamma-ray spectrometry. *Nuclear Instruments and Methods A*. 550, page 603, 2005.
- [Vogt02] K. Vogt, P. Mohr, M. Babilon, W. Bayer, D. Galaviz, T. Hartmann, C. Hutter, T. Rauscher, K. Sonnabend, S. Volz, and A. Zilges. Measurement of the (gamma, n) cross section of the nucleus Au-197 close above the reaction threshold. *Nuclear Physics A*. 707, page 241, 2002.
- [Vogt01] K. Vogt, P. Mohr, M. Babilon, J. Enders, T. Hartmann, C. Hutter, T. Rauscher, S. Volz, and A. Zilges. Measurement of the (gamma,n) reaction rates of the nuclides Pt-190, Pt-192, and Pt-198 in the astrophysical gamma process. *Physical Review C*. 63, 055802, 2001.
- [Wagn05] A. Wagner, R. Beyer, M. Erhard, F. Donau, E. Grosse, A. Hartmann, A. R. Junghans, L. Kaubler, K. Kosev, S. Mallion, C. Nair, N. Nankov, G. Rusev, K. D. Schilling, W. Schulze, and R. Schwengner. The new bremsstrahlung facility at the superconducting electron accelerator ELBE. *Journal of Physics G*. 31, S1969, 2005.
- [Wagn08] A. Wagner, R. Beyer, M. Erhard, E. Grosse, A. R. Junghans, J. Klug, K. Kosev, C. Nair, N. Nankov, G. Rusev, K. D. Schilling, and R. Schwengner. Photon strength distributions in stable even-even molybdenum isotopes. *Journal of Physics G*. 35, 014035, 2008.

- [Wagn01] A. Wagner, F. Dönau, E. Grosse, L. Käubler, K.D. Schilling, R. Schwengner, and W. Schulze. A Beam Dump for Energetic Photons. *Wissenschaftlich-Technische Berichte FZR-319*, page 40, 2001.
- [Wall81] R. K. Wallace and S. E. Woosley. Explosive hydrogen burning. *Astrophysical Journal Supplement Series*. 45, page 389, 1981.
- [Wall97] G. Wallerstein, I. Iben, P. Parker, A. M. Boesgaard, G. M. Hale, A. E. Champagne, C. A. Barnes, F. Kappeler, V. V. Smith, R. D. Hoffman, F. X. Timmes, C. Sneden, R. N. Boyd, B. S. Meyer, and D. L. Lambert. Synthesis of the elements in stars: Forty years of progress. *Reviews of Modern Physics*. 69, page 995, 1997.
- [Woos90] S. E. Woosley, D. H. Hartmann, R. D. Hoffman, and W. C. Haxton. The neutrino-process. *Astrophysical Journal*. 356, page 272, 1990.
- [Zani03] L. Zanini, F. Corvi, H. Postma, F. Becvar, M. Krticka, J. Honzatko, and I. Tomandl. Cascade gamma decay study of Ag-108 following thermal and resonance neutron capture in Ag-107. *Physical Review C*. 68, 014320, 2003.

# Acknowledgement

No endeavor can be successfully completed in isolation and likewise this thesis too is a result of concerted efforts and support from many people. At the outset, I would like to thank my supervisor, Prof. Dr. Eckart Grosse, for the very many things starting with the confidence in picking me up for PhD in FZD. I thank him for all the inspiring discussions, timely advices, encouragement and support throughout all these years.

It is a pleasure to thank Dr. Arnd Junghans and Dr. Andreas Wagner, for being wonderful thesis advisors. All throughout my PhD tenure they have been critical, encouraging, perceptive and insightful. My association with Arnd started right from the moment I landed in Dresden and I shall always treasure my time with him. Thanks a ton for everything Arnd. I thank Andreas for being the right mix of a person who would push when it matters the most; otherwise let me do things at my pace. Making it this far is unimaginable without him.

I am indebted to Dr. Ronald Schwengner for all those scientific and non-scientific discussions which lifted my spirits. His friendly attitude gave me the courage to knock his office door with a repeated phrase "Ronald, I have a simple question..!".

I am so happy to thank Martin for being a well-wisher and friend of all seasons, he has been there always in need - I have already started missing our discussions which often lead to bitter fights and/or sweet endings embedded with M.E's trade mark philosophical reasonings.

I would like to thank Dr. Peter Michel and the ELBE crew for providing stable beam during our photoactivation experiments. Special thanks are due to Dr. Daniel Bemmerer, for initiating a collaboration with the Felsenkeller laboratory in Dresden, which has helped a lot. I am grateful to Dr. Matthias Koehler and Dr. Detlev Degering at the Felsenkeller lab for their time and help with my sample measurements. Many thanks to Dr. Klaus-Dieter Schilling, for his help during the experiments and for making me aware of the ELBE safety regulations. It is a pleasure to work with somebody like Andreas Hartman and I'd like to thank him for all the technical inputs.

I am thankful to our system administrators Jens, Daniela and Christel for all their support and excellent maintenance of the computers and terminals in ISP. Christel has been amazing, her care and affection made me feel at home!

I'd like to thank my friends-cum-colleagues: Roland (both Sr. and Jr.), Gencho, Joakim, Krasimir, Michele and Anja for being so nice and for making our group such a wonderful place to work in. In addition, it is a pleasure to thank Anne, for her limitless helping nature and Dorit for helping me out with all the paper works. I can't miss to thank Kathleen, who was at our Institute when I joined; and who made my initial German days hassle free.

This PhD would have never been possible without the support of my family, particularly my friend-turned-partner Sineej. I thank him for being a wonderful friend, excellent cook and pillar of support during the tiring times. I would also like to thank my parents, brother and friends back home.

Above and all I thank god almighty for all blessings.





# Erklärung

Hiermit versichere ich, daß ich die vorliegende Arbeit ohne unzulässige Hilfe Dritter und ohne Benutzung anderer als der angegebenen Hilfsmittel angefertigt habe. Die als fremde Quellen direkt oder indirekt übernommenen Gedanken sind als solche kenntlich gemacht. Die Arbeit wurde bisher weder im Inland noch im Ausland in gleicher oder ähnlicher Form einer anderen Prüfungsbehörde vorgelegt.

Chithra Nair

*Dresden*

*June 2009*